DETECTION OF MRI BIOMARKERS OF GOLDEN RETRIEVER DUCHENNE MUSCULAR DYSTROPHY

A Dissertation

by

AYDIN ERESEN

Submitted to the Office of Graduate and Professional Studies of
Texas A&M University
in partial fulfillment of the requirements for the degree of

DOCTOR OF PHILOSOPHY

Chair of Committee,	Jim X. Ji
Co-Chair of Committee,	Xiaoning Qian
Committee Members,	Aydin Karsilayan
	Joe N. Kornegay
Head of Department,	Miroslav Begovic

August 2018

Major Subject: Electrical Engineering

ABSTRACT

Golden retriever muscular dystrophy (GRMD) is a spontaneous X-linked canine model of Duchenne muscular dystrophy (DMD) with the affected animals developing a progressively fatal disease, similar to the human condition. As a genetically homologous animal model, GRMD has increasingly been used in natural history studies and studies assessing treatment outcome. There is a great demand for accurate outcome measures across all disease stages to improve the understanding of natural history and to facilitate clinical trials. Histology images are widely used for accurate outcome measures across all disease stages. With a highly invasive method as ground-truth, a variety of non-invasive methods are frequently assessed to extract information corresponding to biological characteristics. Due to high soft-tissue contrast images, MRI is commonly preferred imaging modality to assess GRMD. Spatial correspondence between histology and MRI is a critical step in the quantitative evaluation of skeletal muscle in GRMD. Registration becomes technically challenging due to non-orthogonal histology section orientation, section distortion, and the different image contrast and resolution. This research dissertation proposed a framework for accurate histology to MRI registration and textural analysis methods to describe non-invasive MRI biomarkers utilizing multi-sequence MRI images. The experiments showed that textural features of qualitative and quantitative MRI images can be reliably used for disease assessments and treatment monitoring.

DEDICATION

To my beautiful wife, Esra, and lovely daughters, Mina and Neva.

ACKNOWLEDGEMENTS

I would like to thank my committee chair, Dr. Ji, and my committee members, Dr. Qian, Dr. Karsilayan and Dr. Kornegay, for their guidance and support throughout the course of this research. I would also thank to Dr. Alic at Texas A&M University at Qatar for invaluable help during my research. I also thank Dr. Bosshard and Dr. Wright at Texas A&M University for assistance in acquiring 4.7T MR images and Wade Friedeck at Texas A&M University for assistance in acquiring 3T MR images.

I owe debt of gratitude to observers Akanksh Basavaraju, Pranav Dhulipala and Samira V. Eslahi at Texas A&M University for initializing the registration experiment and selecting landmark locations on the MRI images for evaluation.

Finally, thanks to my wife and daughters for her patience and love.

CONTRIBUTORS AND FUNDING SOURCES

Contributors

The muscle samples used in this study were provided by Dr. Joe N. Kornegay at Texas A&M University. The sectioning of muscle samples and acquiring histology images were completed by Dr. Sharla M. Birch from Texas A&M University. The manually selected region of interest mentioned in Chapter 2 was provided by Xiangbai Chen, MD at Baylor Scott & White Clinic. The statistical analysis depicted in Chapter 2 was completed in part by Dr. Lan Zhou from Texas A&M University. The segmented histology images used in Chapter 4 were generated by Stephen McConnel at Los Alamos National Laboratory as part of his Master's thesis. The random forest classification optimization depicted in Chapter 4 was performed with the assistance of Dr. Noor Hafsa from Texas A&M University at Qatar.

All other work conducted for this research and dissertation was completed independently.

Funding Sources

Graduate study was partially supported by the National Science Foundation under award number 1606136, by National Natural Science Foundation of China under award number 81729003, by the Natural Science Foundation of Shenzhen under award number GHHZ20150316143320494, and by Qatar National Research Fund under award numbers NPRP6-241-2-102, NPRP8-1606-3-322, and NPRP8-293-2-124. Any opinions, findings, and conclusions or recommendations expressed in this paper are those of the authors and do not necessarily reflect the views of the funding agencies.

NOMENCLATURE

US	United States
UK	United Kingdom
CK	Creatine Kinase
MD	Muscular Dystrophy
MDX	X-chromosome-linked muscular dystrophy
BMD	Becker Muscular Dystrophy
DMD	Duchenne Muscular Dystrophy
CMD	Congenital Muscular Dystrophy
GRMD	Golden Retriever Muscular Dystrophy
CT	Computed Tomography
PET	Proton Emission Tomography
US	Ultrasound Imaging
MRI	Magnetic Resonance Imaging
T_1w	T_1-weighted
T_2w	T_2-weighted
FA	Fractional Anisotropy
MD	Mean Diffusivity
ADC	Apparent Diffusion Coefficient
TrD	Trace Diffusivity
MI	Mutual Information
NGF	Normalized Gradient Field

MIC	Combined Mutual Information and Correlation of structures in images
IACUC	Institutional Animal Care and Use Committee
FOV	Field of View
T_R	Repetition Time
T_E	Echo Time
FA	Flip Angle
RGB	Red, Green, Blue
HSV	Hue, Saturation, Value
PS	Pattern Search
BIC	Bootstrap Information Criterion
REML	Restricted Maximum Likelihood
qMRI	Quantitative Magnetic Resonance Imaging
RMS	Root Mean Squares
ROI	Region of Interest
SVM	Support Vector Machines
D_2p	Two-point Dixon
T_1m	T_1-map
T_2m	T_2-map
DWf	Dixon Water Fraction
DFf	Dixon Fat Fraction
FOS	First Order Statistics
GLCM	Gray Level Co-occurrence Matrix
GRLM	Gray Level Run-length Matrix

LBP	Local Binary Patterns
WT	Wavelet Transform
CSA	Cross Section Area
V_{tot}	Total Volume
MVI	Muscle Volume Index
MPI	Muscle Percentage Index
RF	Random Forest
SN	Sensitivity
SP	Specificity
Acc	Accuracy
MPI_{gt}	Muscle Percentage Index of Ground-truth

TABLE OF CONTENTS

Page

LIST OF FIGURES

FIGURE Page

LIST OF TABLES

CHAPTER I

INTRODUCTION

The muscles are structural body elements responsible for the movement. The muscles are divided into three major groups according to their location and functions; cardiac muscles (the heart), smooth muscles (located along with the blood vessels and hollow internal organs) and skeletal muscles (located mostly along the bones) [1]. Skeletal muscles are the largest muscle group with 30-40 percent of the body mass [2]. Additionally, the skeletal muscles are the only muscle group voluntarily controlled by the somatic nervous system, in contrast, involuntary muscles that contract without conscious control [1].

Atrophy and weakness of the skeletal muscles are the most common indications of muscular diseases, i.e. muscular dystrophy and inflammatory myopathy [3, 4]. Muscular atrophy is a process of degeneration of the muscle cells and decrease of the muscle mass. The muscle atrophy is mostly caused by reduced physical activity due to situations causing restricted movement, cancers, myopathies, and several other diseases. The decrease in muscle mass volume triggers the muscle weakness. Furthermore, reduced levels of potassium and other electrolytes may also cause the muscle weaknesses.

Muscular myopathy is a general term for a group of conditions affecting skeletal muscles [5], and are divided into two general groups; genetic and non-genetic muscular disorders [6]. Non-genetic disorders involve autoimmune changes or the changes caused by specific medicines and hormonal disorders. The genetic myopathies congenital, metabolic or periodic myopathies [7], are caused by gene mutations severely affecting the muscular system of the individuals. Muscular dystrophies are the best researched inherited diseases. The congenital myopathies are autosomal dominant diseases that the mutated genes are transferred in different ways: i.e. X-linked, autosomal dominant or recessive [8]. The metabolic myopathies are occurred due to lack of a required substance to maintain muscle functions.

Table 1.1. The occurrence of nine X-linked recessive muscular dystrophy disorders

Muscular Dystrophies	Occurrence	References
Duchenne and Becker MD	1 in 3500-5000 worldwide. 400-600 male patients are born in the US each year	[9-11]
Myotonic MD	1 in 8000 in worldwide	[12]
Limb-girdle MD	1 in 14500 to 123000 worldwide	[13]
Facioscapulohumeral MD	1 in 20000 worldwide	[14]
Emery-dreifuss MD	1 in 100000 worldwide	[15, 16]
Oculopharyngeal MD	1 in 100000 in Europe. 1 in 1000 in Quebec, Canada among the French-Canadian population. 1 in 700 Jewish population of Bukaran in Israel	[17, 18] [18, 19].
Congenital MD		
Fukuyama CMD	2-4 in 100000 in Japan	[20].
LMNA CMD	Only 50 patients are recorded in medical history	[21]
Distal MD	1 in 440000 in Japan	[22, 23]

Muscular Dystrophies

History of the muscular dystrophy starts with an essay reporting progressive muscle weakness in male patients (published by Sir Charles Bell in 1830), and a publication of Semmola in 1834 describing clinical features, and a report by Conte and Gioia in 1836 on a recessive muscle weakness, replacement of muscle tissue with adipose and other connective tissues and damages [24]. The following articles published in the 1850s mentioned the early death of boys with progressive muscle weaknesses. The name of the disease was given after the French neurologist

Duchenne de Boulogne who studied the recessive muscle weakness of thirteen boys with the most common muscular dystrophy currently known as Duchenne muscular dystrophy [25].

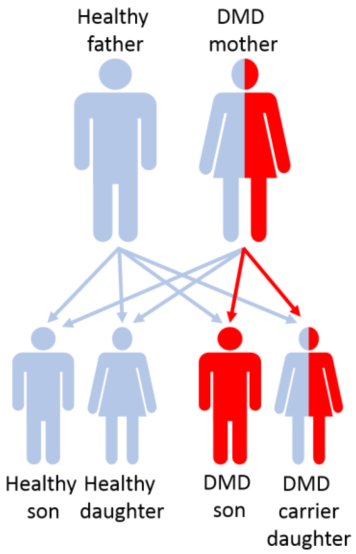

Figure 1.1. Illustration of X-linked disorder transfer to next generation

Muscular dystrophy is the group of genetic disorders caused due to alteration of specific gene sequences [25-28]. The muscular dystrophy diseases can be passed to the next generation with the transfer of altered genes. Besides, a gene mutation can occur spontaneously by environmental effects and cause to the formation of the disease in the families without known dystrophy history. Recently, there are more than thirty types of dystrophies described in the literature and they're grouped in nine major groups; Duchenne, Becker, Emery-dreifuss, Limb-girdle, Facioscapulohumeral, Myotonic, Oculopharyngeal and Distal muscular dystrophy [26, 29, 30], for prevalence, see Table 1.1 [9-23].

The major types of muscular dystrophies are specified according to their inheritance type: recessive, dominant and sex-linked. Figure 1.1 illustrates the transfer of mutated gene to the next generation. In the recessively inherited disorders (e.g. limb-girdle dystrophies), the same gene on both parents is mutated. According to the number of transferred mutated genes, the child becomes either a patient or a carrier. In dominantly inherited disorders (e.g. facioscapulohumeral and oculopharyngeal dystrophy), only one gene is involved in developing the condition. Sex-linked disorders are occurred due to a gene mutation on the X chromosome. Due to a low probability of gene mutation on both X chromosomes, in general, the males are the patient of this types of disorder, and females are the carriers for this group of diseases. Duchenne and Becker muscular dystrophies are X-linked muscle disorders. Among all types of muscular dystrophy diseases, Duchenne type muscular dystrophy is the most common and severe type of muscular dystrophy [26, 31], and therefore it's selected as the topics of this study.

Duchenne Muscular Dystrophy

Duchenne Muscular Dystrophy (DMD) is the most common dystrophy type connected to the X-linked inheritance and it affects exclusively male infants due to dystrophin type protein deficiency [32-34]. Dystrophin protein is responsible to keep muscle fibers intact and acquainted with a chemical signal transfer in cells [35]. Therefore, with insufficient dystrophin produced, muscle fibers lose their structural shape and functionality over time [35]. A representation for dystrophin glycoprotein complex components and membranes in skeletal muscle is shown in Figure 1.2. Dystrophin protein mostly expressed in skeletal and cardiac muscles [36]. The structural integrity of a damaged muscle depends on a fine balance between destruction and regeneration of the muscle tissue. In normal muscle repair, fibers are removed by inflammatory cells and they're repaired or replaced with satellite cells that form muscle cells later. In DMD case, the amount of satellite cells reduces or they lost their ability forming muscle cells and the muscular tissue is replaced by fat or fibrosis tissues.

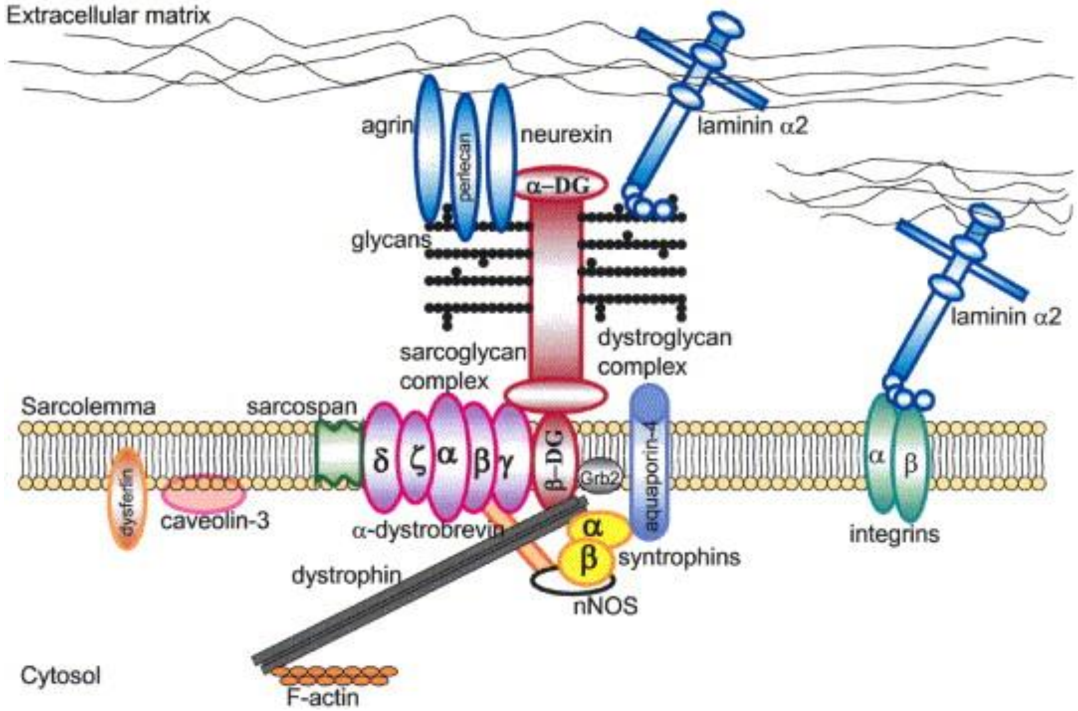

Figure 1.2. The components of dystrophin glycoprotein complex with other membranes in skeletal muscle. Reprinted with permission of Neuromuscular Disorders [37].

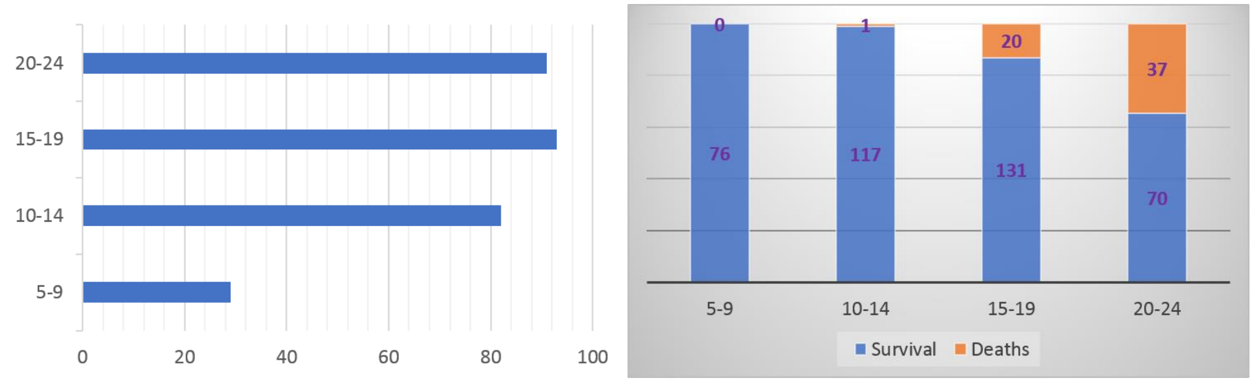

Figure 1.3. The severity of DMD disease progression. (a) show the percentage of patients using wheelchair varying ages and (b) demonstrates the number of deaths at varying age groups in DMD disease (adapted from [38]).

DMD disorder shows faster progression and increased severity than other muscular dystophies [39]. Although DMD and BMD is caused by a mutation on dystrophin gene, the severity of these dystrophies significantly differs. DMD is caused by out-frame mutations which causes absence of less than 5% of regular level of dystrophin protein is absent in DMD patients [40]. On the other hand, BMD which is caused by in-frame mutations on dystrophin gene, is less severe due to partial-wild-type dystrophin function (10% to 40% dystrophin of the normal amount) [41].

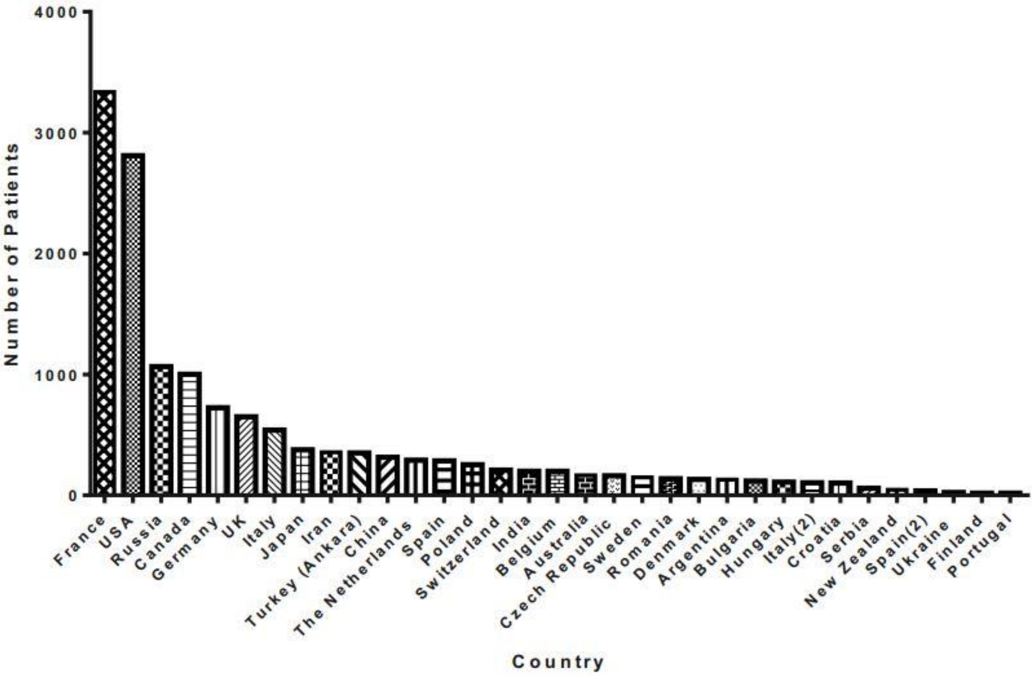

Figure 1.4. The number of DMD patients identified by national DMD network agencies of the countries registered to Treat-NMD network. The data is presented in sorted form (highest to lowest).
Reprinted with permission from Human Mutation [42].

Although DMD disease is an inherited disease, It may be seen in families without any DMD disease in family history due to somatic mutations [43]. It causes progressive muscle weaknesses and loss of muscle functions starting at lower limbs muscles and then spreads to the other muscle groups including heart and respiration muscles [32-34]. Due to continuous muscle atrophy and weaknesses, the patients are restricted to wheelchairs at earlier teenage years (Figure 1.3 (a)) and ends with death during young adulthood varying ages among the patients (Figure 1.3 (b)) [38, 44].

Figure 1.4 illustrates the incidence of DMD worldwide. To provide better access the findings related to disease and treatments methods and to accelerate the preclinical and clinical developments in the neuromuscular field, a global network connecting the local DMD registries from thirty-one countries was established in the UK [42].

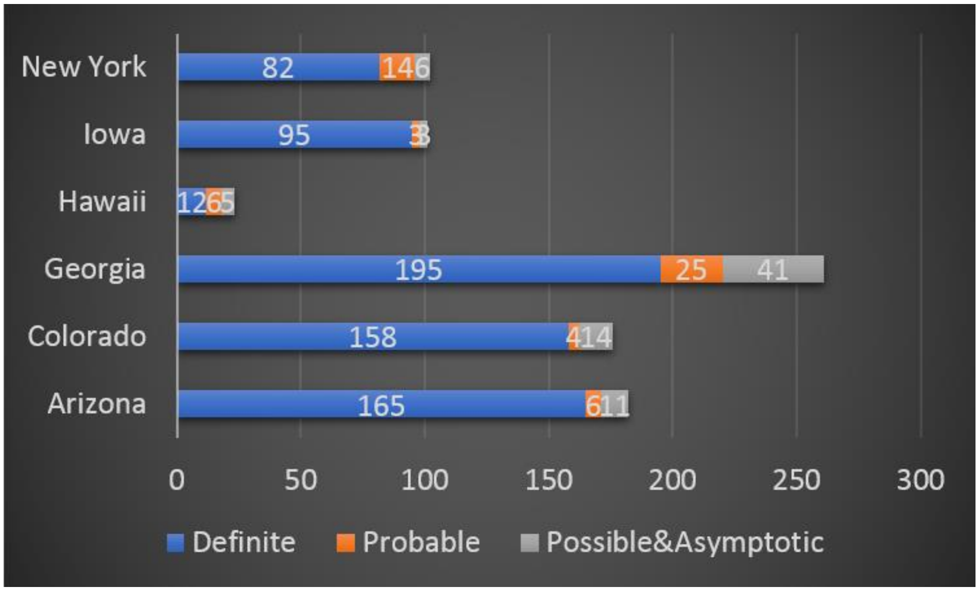

Figure 1.5. Number of males with DMD or BMD in 6 US states identified by MD STARnet from 1991 to 2010 (adapted from Romitte et al. [45]).

Figure 1.5 illustrates the incidence of DMD and BMD in six states of United States, as identified by MD STARnet Muscular Dystrophy Surveillance, Tracking, and Research Network [45].

The number of DMD and BMD cases between 5 and 9 years was given in Figure 1.6 (a). The total number of 528 DMD and 171 BMD patients were grouped based on their birth years. In Figure 1.6 (b), the number of DMD and BMD patients were presented in groups according to their ages. While the number of DMD patients within first two age groups (toddler to teenage years) was increased, a significant decrease was observed during last two stages of age terms. The number of BMD patients were increased for first three stages and decreased in the last term of the ages. Figure 1.6 (a) and (b) showed that the DMD occurs more frequently than BMD disease.

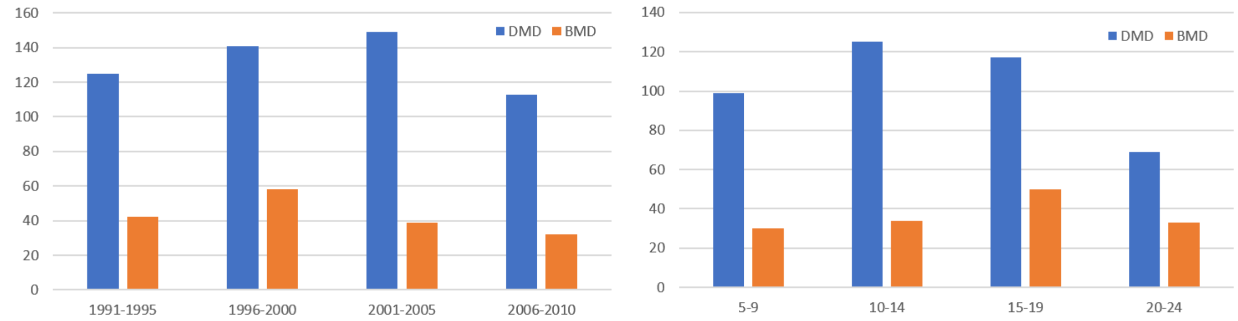

Figure 1.6. The number of DMD and BMD patients identified by MD STARnet. (a) Patients aged between 5 and 9 grouped according to the year of birth. (b) The patients with age of 5 to 24 (adapted from Romitte et al. [45]).

Currently, there is no approved treatment that can prevent or reverse the effects of DMD disorder. However, there are several drugs, gene, and cell therapies utilized to reduce effects of the disease and improve quality and span of life for the DMD patients [46, 47]. In [48], Kim et al. illustrated the clinical responses for two different treatment options for short-term and long-term usage. Although short-term drug usage doesn’t significantly affect the lifespan, long-term use of both drugs delayed the loss of ambulation within the patients.

Animal Models of DMD

Generally, the complexity of diseases prevents researchers to find alternative methods in replacement of living animals [25]. Therefore, the animal models are still required to improve understanding the biology of the diseases and facilitate the clinical trials. The literature describes almost sixty animal models described for DMD disorder. [49]. Among the animal models described in the literature, a mouse model (MDX, [50]) and canine model (GRMD, [51]) were the most studied animal models of Duchenne muscular dystrophy. The MDX model, discovered in the early 1980s, is the most commonly used animal model for clinical research studies. However, the severity of the condition in MDX mice is milder than DMD patients. GRMD, discovered in the late 1980s, was the first and most widely used canine model in clinical research studies. The clinical and histological studies showed remarkable similarities between GRMD and DMD diseases [49, 52]. Besides, animals with GRMD disorder are severely affected similar to human DMD patients and their lifespan was affected about the same rate with DMD patients [49]. Therefore, GRMD model is commonly used in clinical trials.

Diagnosis

DMD is diagnosed by physical tests to analyze weakness of the muscles, blood test to measure creatine kinase (CK) level, muscle biopsy, or by genetic tests to examine mutations of dystrophin gene [53]. There is a great demand for accurate outcome measures across all disease stages to improve the understanding of natural history and to facilitate clinical trials. Histology images are widely used for accurate outcome measures across all disease stages. With a highly invasive method as ground-truth, a variety of non-invasive methods are frequently assessed to extract information corresponding to biological characteristics.

There are several non-invasive imaging modalities which have potential to be used to diagnose DMD disorder; CT, PET, US, and MRI [54-57]. In CT imaging modality, multiple X-ray measurements are collected to generate a cross-sectional image of the organs. The intensity of the image is formed based on the attenuation of the X-ray signals captured by the receivers. The high sensitivity of CT resolution to density variation between the tissues makes it suitable for tissue analyses. In DMD disorder, CT is used to detect structural changes in muscle tissue such as fat deposition [54]. However, X-ray exposure and insensitivity for separation of adipose and connective tissue of the muscles limit the usage of CT in DMD studies, especially for younger patients [58].

In PET imaging, gamma rays scattered from injected radioactive tracer collided with electrons are captured by the scanner. Based on the substance of the radioactive material, various metabolic activities can be captured with uptake level of radioactive tracer. In DMD disorder, muscle tissue is replaced with connective tissue and fat. Due to an increase of metabolically inactive fibrosis tissue, radio-labeled substance uptake level decrease can be useful for analysis of skeletal muscle tissues for DMD [55]. However, increased uptake level with fat deposition limits the usage of PET imaging for DMD disease [59].

In US imaging, the backscattered echoes are used to generate an image of the internal organs utilizing the reflected signals based on the density of the organs. US imaging is advantageous in medical diagnosis due to absence of ionizing radiation, low cost and portability. In DMD, US was used to examine muscle involvement to determine suitable muscle tissues for biopsy as analyzing the backscattered signals [56, 60]. However, usage of US method is limited in the analysis of superficial muscle groups.

In MRI scanner, the protons in the human body were aligned with the direction of the strong magnetic field. When an RF pulse was applied, the alignment of the protons was changed. After RF pulse was turned off, the protons return to the equilibrium state with different rates among the tissues. The varying recovery times enable to characterize the tissues with various disease models. The high soft tissue contrast and absence of ionizing radiation makes MRI imaging one of the most promising alternative non-invasive methods for analysis of skeletal muscles [61]. In addition, deeper organs can be imaged easily and accurately using MRI. Therefore, MRI imaging technique is widely used to diagnose DMD disease using various MRI sequences [53, 57, 62-74]. In GRMD disease, fat and fibrosis deposition show radical changes similar to DMD which makes GRMD hard to diagnose [75]. The studies completed on GRMD subjects can be separated into two groups: i.e. qualitative and quantitative [61, 75-89]. The qualitative analysis methods include subjective grading of structural MRI images using an MRI grading scale [58, 88-90]. T_1w images and post-contrast images are widely evaluated based on visual inspection of structural alterations i.e. fat infiltration. On the other hand, quantitative image analysis techniques evaluate the quantitative measurements of MRI images (T_1w or T_2w) or maps (T_1 and T_2 values, water and fat fractions, and tissue diffusivity) and track changes among different stages of the disease [76, 78, 85-87, 91]. A variety of studies were focused on detection of imaging biomarkers based on interpretation of qualitative and quantitative MRI data [61, 64, 76, 87, 92-94]. In early stages of GRMD disease, T_1 relaxation time is increased due to increased muscle free water molecules compared to healthy subjects caused by consecutive muscle degeneration-regeneration processes [61, 83]. T_1 relaxation time decreases in the following stages due to the replacement of muscle with fat and connective tissues. T_2 relaxation time decreases with the disease progression [58]. T_2 values in the tissues of fat and connective tissue also necrotic cells are all longer than muscle tissues. Therefore, fat or fibrosis cannot be easily separated from necrosis [83]. Although fat deposition progressively occurs during disease stages, GRMD subjects do not show the similar level of fat deposition as seen in DMD patients [95]. The studies using DTI MRI showed decreased FA, ADC and increased MD for selected muscle types in DMD patients [70]. Besides, a correlation between fat infiltration and ADC, FA values was observed in DMD patients [68].

In DMD disease, muscle groups are affected by varying severity and speed [90, 96]. Therefore, studies have investigated the effects of the DMD disease on different skeletal muscles to determine the most vulnerable muscle groups that provide larger difference during the disease progression [61, 89, 90, 96, 97].

Quantitative MRI-based Imaging Biomarkers

Multiple research groups use texture analysis of MRI images to determine effects of GRMD disease on skeletal muscles [61, 73, 78, 81, 82]. The general hypothesis of the studies is that the structural changes in muscle tissue will be reflected in MRI images. Therefore, disease effects may be captured with extracted features of grayscale MRI data. The first order statistics [98], co-occurrence matrix [99], run-length matrix [100] and Zernike/Legendre moments of the MRI data was extracted from T_1w or T_2w images [61, 73, 81, 82]. The presented results show that MRI has the potential for diagnosis of GRMD disease using textural analyses [73, 79, 81, 82].

The signal intensity of MRI images is determined by the biological changes seen on histology images. The understanding the effects of histological changes on MRI images will improve the connection between histology and MRI. Therefore, the direct relationship between histological details and MRI characteristics should be interpreted for sensitive and robust non-invasive MRI biomarkers for GRMD disease.

Outline of the thesis

The aim of this thesis was to develop and evaluate quantitative, texture-based imaging biomarkers extracted from ex vivo qMRI, reflecting the changes in aging GRMD pectineus muscles. The procedure defined in this thesis was addressed following questions:

- What kind of methods are needed to align a histology slice with an ex vivo MRI volume?
- Which MRI imaging sequences provides a better understanding of the disease progression in pectineus muscles?
- Which textural analysis methods of MRI sequences result in better performance for assessment of clinical outcomes for GRMD disease?
- Which locally extracted features from quantitative MRI images utilizes the MPI as a biomarker of GRMD disease among age groups?

Chapter 2 presents a method for accurate registration of a 2D high-resolution histology image and 3D MRI volume of healthy and GRMD muscles. The aim of this study is to provide a framework for an accurate histology image localization in 3D MRI volume. The methodology of this study combines standardized MRI and histology data acquisition and processing methods, interactive orientation initialization, an improved similarity metric for multimodality images and increasing complexity of transformation. In this study, the proposed registration process was completed in three consecutive steps increasing the degrees of freedom incrementally. Accurate registration of histology slice and MRI volume enables to investigate the localized correlation between MRI modalities and biological tissue classes [101-103].

Chapter 3 represents a study examining textural features of two qualitative (T_1w and T_2w) and four quantitative MRI images (T_1m, T_2m, Dixon water fraction, Dixon fat fraction) for assessing the disease severity while reducing MRI imaging time and cost. Total of forty-one textural features using five different methods is extracted from six MRI images acquired with a 3T clinical scanner. Using an SVM based classification approach, the performance of the classifier was evaluated with MRI modality feature pairs to detect potential MRI biomarkers.

In Chapter 4, an automatically generated muscle percentage index as an imaging biomarker of muscle degeneration in GRMD was proposed. The MPI was generated by a machine learning classification process created by random forest approach using quantitative MRI images (T_1m, T_2m, two Dixon maps, and four DTI maps) of nine GRMD samples. While using three type of texture descriptor features (local binary pattern, gray-level co-occurrence matrix, gray-level run-length matrix) and a gradient image (histogram of oriented gradients) of raw qMRI images as input for the classification models, segmented histology image labels were used as output classes (muscle, non-muscle). All eight qMRI maps were co-registered and resampled to the same spatial resolution, and co-registered with histology validated class labels (muscle and non-muscle). The classification performance across different stages in the natural history of GRMD was evaluated using optimized models in a leave-one-out cross-validation approach. MPI was generated from a final classification result, for each sample separately, by a morphological filter as pruning method was evaluated as a noninvasive biomarker for different aged dogs.

Chapter 5 summarizes the main results for clinical, experimental studies and contributions of the thesis, and discusses the obtained performances of completed studies. Furthermore, it also provides the recommendations for future research.

References

[1] W. C. Mackenzie, *The action of muscles, including muscle rest and muscle re-education*. New York: Paul B. Hoeber, 1921.

[2] E. N. Marieb and K. Hoehn, *Human Anatomy & Physiology*, 10 ed. Boston: Pearson, 2016.

[3] G. Karpati, *Disorders of Voluntary Muscle*, 8 ed. Cambridge: Cambridge University Press, 2010.

[4] Encyclopædia Britannica. (2014, 14 May). *Muscle disease*. Available: https://www.britannica.com/science/muscle-disease#ref58881

[5] National Institute of Neurological Disorders and Stroke. (2017, 17 May). *Myopathy Information Page*. Available: https://www.ninds.nih.gov/Disorders/All-Disorders/Myopathy-Information-Page

[6] National Neuroscience Institute. (2017, 14 May). *Muscle Diseases*. Available: https://www.nni.com.sg/PatientsandVisitors/Conditions-Treatments/Pages/Muscle-Diseases.aspx

[7] Remedy's Health Communities. (2015, 15 May). *Myopathies*. Available: http://www.health communities.com/myopathies/types.shtml

[8] C. A. Sewry and C. Wallgren-Pettersson, "Myopathology in congenital myopathies," *Neuropathology And Applied Neurobiology*, vol. 43, pp. 5-23, 2017.

[9] A. E. H. Emery, "The muscular dystrophies," *The Lancet*, vol. 359, pp. 687-695, 2002.

[10] J. K. Mah, L. Korngut, J. Dykeman, L. Day, T. Pringsheim, and N. Jette, "A systematic review and meta-analysis on the epidemiology of Duchenne and Becker muscular dystrophy," *Neuromuscular Disorders*, vol. 24, pp. 482-491, 2014.

[11] S. Verma, Y. Anziska, and J. Cracco, "Review of Duchenne Muscular Dystrophy (DMD) for the Pediatricians in the Community," *Clinical Pediatrics*, vol. 49, pp. 1011-1017, 2010.

[12] U.S. National Library of Medicine. (2018, 18 May). *Myotonic dystrophy*. Available: https://ghr.nlm.nih.gov/condition/myotonic-dystrophy

[13] S. R. Hammans, "Myotonic Dystrophy, 3rd edition," *Brain,* vol. 125, pp. 1225-1226, 2002.

[14] S. Sacconi, L. Salviati, and C. Desnuelle, "Facioscapulohumeral muscular dystrophy," *Biochimica et Biophysica Acta (BBA) - Molecular Basis of Disease,* vol. 1852, pp. 607-614, 2015.

[15] G. Bonne and S. Quijano-Roy, "Emery-Dreifuss muscular dystrophy, laminopathies, and other nuclear envelopathies," *Handbook of Clinical Neurology,* vol. 113, pp. 1367-76, 2013.

[16] U.S. National Library of Medicine. (2018). *Emery-Dreifuss muscular dystrophy*. Available: https://ghr.nlm.nih.gov/condition/emery-dreifuss-muscular-dystrophy

[17] S. C. Blumen, J.-P. Bouchard, B. Brais, R. L. Carasso, D. Paleacu, V. E. Drory, *et al.*, "Cognitive impairment and reduced life span of oculopharyngeal muscular dystrophy homozygotes," *Neurology,* vol. 73, pp. 596-601, 2009.

[18] U.S. National Library of Medicine. (2018, 18 May). *Oculopharyngeal muscular dystrophy*. Available: https://ghr.nlm.nih.gov/condition/oculopharyngeal-muscular-dystrophy

[19] A. V. Marusin, H. A. Kurtanov, N. R. Maksimova, M. G. Swarovsakaja, and V. A. Stepanov, "Haplotype analysis of oculopharyngeal muscular dystrophy (OPMD) locus in Yakutia," *Russian Journal of Genetics,* vol. 52, pp. 331-338, 2016.

[20] T. Tatsushi, K. Kazuhiro, T. Satoshi, S. Junko, K. Hiroki, K. Hiroki, *et al.*, "Fukuyama-type congenital muscular dystrophy (FCMD) and α-dystroglycanopathy," *Congenital Anomalies,* vol. 43, pp. 97-104, 2003.

[21] A. Barateau, N. Vadrot, P. Vicart, A. Ferreiro, M. Mayer, D. Héron, *et al.*, "A Novel Lamin A Mutant Responsible for Congenital Muscular Dystrophy Causes Distinct Abnormalities of the Cell Nucleus," *PLOS ONE,* vol. 12, pp. 1-18, 2017.

[22] T. Takahashi, M. Aoki, M. Tateyama, E. Kondo, T. Mizuno, Y. Onodera, *et al.*, "Dysferlin mutations in Japanese Miyoshi myopathy," *Relationship to phenotype,* vol. 60, pp. 1799-1804, 2003.

[23] U.S. National Library of Medicine. (2018, 18 May). *Miyoshi myopathy*. Available: https://ghr.nlm.nih.gov/condition/miyoshi-myopathy

[24] R. A. Huml, "Muscular Dystrophy: Historical Background and Types," in *Muscular Dystrophy: A Concise Guide*, R. A. Huml, Ed., ed Cham: Springer International Publishing, 2015, pp. 5-7.

[25] "Duchenne muscular dystrophy," in *Medline Plus Encylopedia*, ed.

[26] M. Cardamone, B. T. Darras, and M. M. Ryan, "Inherited Myopathies and Muscular Dystrophies," *Semin Neurol,* vol. 28, pp. 250-259, 2008.

[27] J. N. Walton, "On the inheritance of muscular dystrophy," *Annals of Human Genetics,* vol. 20, 1955.

[28] G. Bulfield, W. G. Siller, P. A. L. Wight, and K. J. Moore, "X chromosome-linked muscular dystrophy (mdx) in the mouse," *Proceedings of the National Academy of Sciences,* vol. 81, pp. 1189-1192, 1984.

[29] E. Mercuri, "Muscle MRI in inherited neuromuscular disorders: Past, present, and future," *Journal of Magnetic Resonance Imaging,* vol. 25, pp. 433-440, 2007.

[30] L. ten Dam, "Muscle imaging in inherited and acquired muscle diseases," *European Journal of Neurology,* vol. 23, pp. 688-703, 2016.

[31] C. M. McDonald, R. T. Abresch, G. T. Carter, W. M. Fowler, E. R. Johnson, and D. D. Kilmer, "Profiles of neuromuscular diseases. Duchenne muscular dystrophy," *American Journal of Physical Medicine & Rehabilitation,* vol. 74, 1995.

[32] R. H. T. Edwards, D. J. Newham, D. A. Jones, and S. J. Chapman, "Role of mechanical damage in pathogenesis of proximal myopathy in man," *The Lancet,* vol. 1, pp. 548-552, 1984.

[33] J. Y. Cheung, J. V. Bonventre, C. D. Malis, and A. Leaf, "Calcium and ischemic injury," *The New England Journal of Medicine,* vol. 314, pp. 1670-1676, 1986.

[34] E. P. Hoffman, R. H. Brown, Jr, and L. M. Kunkel, "Dystrophin: the protein product of the Duchenne muscular dystrophy locus," *Cell,* vol. 51, pp. 919-928, 1987.

[35] D. J. Blake, A. Weir, S. E. Newey, and K. E. Davies, "Function and Genetics of Dystrophin and Dystrophin-Related Proteins in Muscle," *Physiological Reviews,* vol. 82, pp. 291-329, 2002.

[36] M.-L. Bang, T. Centner, F. Fornoff, A. J. Geach, M. Gotthardt, M. McNabb, *et al.*, "The Complete Gene Sequence of Titin, Expression of an Unusual ≈700-kDa Titin Isoform, and Its Interaction With Obscurin Identify a Novel Z-Line to I-Band Linking System," *Circulation Research,* vol. 89, pp. 1065-1072, 2001.

[37] R. D. Cohn, "Dystroglycan: important player in skeletal muscle and beyond," *Neuromuscular Disorders,* vol. 15, pp. 207-217, 2005.

[38] "Prevalence of Duchenne/Becker Muscular Dystrophy Among Males Aged 5--24 Years --- Four States, 2007," Centers of Disease Control and Prevention, Ed., ed. USA, 2009.

[39] Q. Bing, K. Hu, Q. Tian, Z. Zhao, H. Shen, N. Li, *et al.*, "Semi-quantitative assessment of lower limb MRI in dystrophinopathy," *International Journal of Clinical and Experimental Medicine,* vol. 9, pp. 13723-13732, 2016.

[40] A. Nicolas, C. Lucchetti-Miganeh, R. B. Yaou, J.-C. Kaplan, J. Chelly, F. Leturcq, *et al.*, "Assessment of the structural and functional impact of in-frame mutations of the DMD gene, using the tools included in the eDystrophin online database," *Orphanet Journal of Rare Diseases,* vol. 7, p. 45, July 09 2012.

[41] H. Bellayou, K. Hamzi, M. A. Rafai, M. Karkouri, I. Slassi, H. Azeddoug, *et al.*, "Duchenne and Becker Muscular Dystrophy: Contribution of a Molecular and

Immunohistochemical Analysis in Diagnosis in Morocco," *Journal of Biomedicine and Biotechnology,* vol. 2009, p. 5, 2009.

[42] C. L. Bladen, K. Rafferty, V. Straub, S. Monges, A. Moresco, H. Dawkins*, et al.*, "The TREAT-NMD Duchenne muscular dystrophy registries: conception, design, and utilization by industry and academia," *Human Mutation,* vol. 34, pp. 1449-1457, 2013.

[43] National Human Genome Research Institute. (May 15, 2018). *Duchenne Muscular Dystrophy*. Available: https://rarediseases.info.nih.gov/diseases/6291/duchenne-muscular-dystrophy

[44] A. E. Parker, S. A. Robb, J. Chambers, A. C. Davidson, K. Evans, J. O'Dowd*, et al.*, "Analysis of an adult Duchenne muscular dystrophy population," *QJM: An International Journal of Medicine,* vol. 98, pp. 729-736, 2005.

[45] P. A. Romitti, Y. Zhu, S. Puzhankara, K. A. James, S. K. Nabukera, G. K. D. Zamba*, et al.*, "Prevalence of Duchenne and Becker Muscular Dystrophies in the United States," *Pediatrics,* vol. 135, pp. 513-521, 2015.

[46] U.S. Food and Drug Administration. (2017, 4 May). *FDA approves drug to treat Duchenne muscular dystrophy*. Available: https://www.fda.gov/NewsEvents/Newsroom/PressAnnouncements/ucm540945.htm

[47] National Institute of Neurological Siorders and Stroke (NINDS). (2017, May 15). *Muscular Dystrophy Information Page*. Available: https://www.ninds.nih.gov/Disorders/All-Disorders/Muscular-Dystrophy-Information-Page

[48] S. Kim, K. A. Campbell, D. J. Fox, D. J. Matthews, and R. Valdez, "Corticosteroid Treatments in Males With Duchenne Muscular Dystrophy: Treatment Duration and Time to Loss of Ambulation," *Journal of Child Neurology*, vol. 30, pp. 1275-1280, 2014.

[49] J. W. McGreevy, C. H. Hakim, M. A. McIntosh, and D. Duan, "Animal models of Duchenne muscular dystrophy: from basic mechanisms to gene therapy," *Disease Models & Mechanisms,* vol. 8, pp. 195-213, 2015.

[50] J. Manning and D. O'Malley, "What has the mdx mouse model of duchenne muscular dystrophy contributed to our understanding of this disease?," *Journal of Muscle Research and Cell Motility,* vol. 36, pp. 155-167, 2015.

[51] J. N. Kornegay, J. R. Bogan, D. J. Bogan, M. K. Childers, and R. W. Grange, "Golden retriever muscular dystrophy (GRMD): developing and maintaining a colony and physiological functional measurements," *Methods in Molecular Biology,* vol. 709, pp. 105-123, 2011.

[52] J. N. Kornegay, S. M. Tuler, D. M. Miller, and D. C. Levesque, "Muscular dystrophy in a litter of golden retriever dogs," *Muscle Nerve,* vol. 11, pp. 1056-1064, 1988.

[53] D. J. Birnkrant, K. Bushby, C. M. Bann, S. D. Apkon, A. Blackwell, D. Brumbaugh, *et al.*, "Diagnosis and management of Duchenne muscular dystrophy, part 1: diagnosis, and neuromuscular, rehabilitation, endocrine, and gastrointestinal and nutritional management," *The Lancet Neurology,* vol. 17, pp. 251-267, 2018.

[54] M. Jiddane, J. L. Gastaut, J. F. Pellissier, J. Pouget, G. Serratrice, and G. Salamon, "CT of primary muscle diseases," *American Journal of Neuroradiology,* vol. 4, pp. 773-776, 1983.

[55] L. J. Soo, P. Zoltán, J. Csaba, B. M. E., M. Otto, C. D. C., *et al.*, "Altered regional brain glucose metabolism in Duchenne muscular dystrophy: A pet study," *Muscle & Nerve,* vol. 26, pp. 506-512, 2002.

[56] E. L. Finanger, B. Russman, S. C. Forbes, W. D. Rooney, G. A. Walter, and K. Vandenborne, "Use of Skeletal Muscle MRI in Diagnosis and Monitoring Disease Progression in Duchenne Muscular Dystrophy," *Physical Medicine & Rehabilitation Clinics of North America,* vol. 23, pp. 1-10, 2012.

[57] H. K. Kim, A. C. Merrow, S. Shiraj, B. L. Wong, P. S. Horn, and T. Laor, "Analysis of fatty infiltration and inflammation of the pelvic and thigh muscles in boys with Duchenne muscular dystrophy (DMD): grading of disease involvement on MR imaging and correlation with clinical assessments," *Pediatric Radiology,* vol. 43, pp. 1327-1335, 2013.

[58] H. K. Kim, T. Laor, P. S. Horn, J. M. Racadio, B. Wong, and B. J. Dardzinski, "T2 Mapping in Duchenne Muscular Dystrophy: Distribution of Disease Activity and Correlation with Clinical Assessments," *Radiology,* vol. 255, pp. 899-908, 2010.

[59] K. Gutpell and L. Hoffman, "Non-invasive assessment of skeletal muscle pathology and treatment for Duchenne muscular dystrophy.OA Musculoskeletal Medicine," *OA Musculoskeletal Medicine,* vol. 1, pp. 1-5, 2013.

[60] I. Shklyar, T. R. Geisbush, A. S. Mijialovic, A. Pasternak, B. T. Darras, J. S. Wu*, et al.*, "Quantitative Muscle Ultrasound in Duchenne Muscular Dystrophy: A Comparison of Techniques," *Muscle & nerve,* vol. 51, pp. 207-213, 2015.

[61] Z. Fan, J. Wang, M. Ahn, Y. Shiloh-Malawsky, N. Chahin, S. Elmore*, et al.*, "Characteristics of magnetic resonance imaging biomarkers in a natural history study of golden retriever muscular dystrophy," *Neuromuscular Disorders,* vol. 24, pp. 178-191, 2014.

[62] B. H. Wokke, J. C. Van Den Bergen, M. T. Hooijmans, J. J. Verschuuren, E. H. Niks, and H. E. Kan, "T2 relaxation times are increased in Skeletal muscle of DMD but not BMD patients," *Muscle & Nerve,* vol. 53, pp. 38-43, 2016.

[63] R. J. Willcocks, I. A. Arpan, S. C. Forbes, D. J. Lott, C. R. Senesac, E. Senesac*, et al.*, "Longitudinal measurements of MRI-T2 in boys with Duchenne muscular dystrophy: Effects of age and disease progression," *Neuromuscular Disorders,* vol. 24, pp. 393-401, 2014.

[64] B. H. Wokke, J. C. van den Bergen, M. J. Versluis, E. H. Niks, J. Milles, A. G. Webb*, et al.*, "Quantitative MRI and strength measurements in the assessment of muscle quality in Duchenne muscular dystrophy," *Neuromuscular Disorders,* vol. 24, pp. 409-416, 2014.

[65] U. Bonati, P. Hafner, S. Schädelin, M. Schmid, A. Naduvilekoot Devasia, J. Schroeder*, et al.*, "Quantitative muscle MRI: A powerful surrogate outcome measure in Duchenne muscular dystrophy," *Neuromuscular Disorders,* vol. 25, pp. 679-685, 2015.

[66] M. T. Hooijmans, B. M. Damon, M. Froeling, M. J. Versluis, J. Burakiewicz, J. J. G. M. Verschuuren*, et al.*, "Evaluation of skeletal muscle DTI in patients with duchenne muscular dystrophy," *NMR in Biomedicine,* vol. 28, pp. 1589-1597, 2015.

[67] L. Lilian, H. François, G. Arnaud, P. Yann, M. Armelle, H. Jean-Yves*, et al.*, "Non-invasive assessment of muscle stiffness in patients with duchenne muscular dystrophy," *Muscle & Nerve,* vol. 51, pp. 284-286, 2015.

[68] S. Ponrartana, L. Ramos-Platt, T. A. L. Wren, H. H. Hu, T. G. Perkins, J. M. Chia, *et al.*, "Effectiveness of Diffusion Tensor Imaging in Assessing Disease Severity in Duchenne Muscular Dystrophy: Preliminary Study," *Pediatric Radiology,* vol. 45, pp. 582-589, 2014.

[69] C. Wary, N. Azzabou, C. Giraudeau, J. L. Louër, M. Montus, T. Voit, *et al.*, "Quantitative NMRI and NMRS Identify Augmented Disease Progression After Loss of Ambulation in Forearms of Boys with Duchenne Muscular Dystrophy," *NMR in Biomedicine,* vol. 28, pp. 1150-1162, 2015.

[70] G. D. Li, Y. Y. Liang, P. Xu, J. Ling, and Y. M. Chen, "Diffusion-Tensor Imaging of Thigh Muscles in Duchenne Muscular Dystrophy: Correlation of Apparent Diffusion Coefficient and Fractional Anisotropy Values With Fatty Infiltration," *American Journal of Roentgenology,* vol. 206, pp. 867-870, 2016.

[71] A. Mankodi, C. A. Bishop, S. Auh, R. D. Newbould, K. H. Fischbeck, and R. L. Janiczek, "Quantifying disease activity in fatty-infiltrated skeletal muscle by IDEAL-CPMG in Duchenne muscular dystrophy," *Neuromuscular Disorders,* vol. 26, pp. 650-658, 2016.

[72] R. J. Willcocks, W. D. Rooney, W. T. Triplett, S. C. Forbes, D. J. Lott, C. R. Senesac, *et al.*, "Multicenter prospective longitudinal study of magnetic resonance biomarkers in a large duchenne muscular dystrophy cohort," *Annals of Neurology,* vol. 79, pp. 535-547, 2016.

[73] M.-H. Zhang, J.-S. Ma, Y. Shen, and Y. Chen, "Optimal classification for the diagnosis of duchenne muscular dystrophy images using support vector machines," *International Journal of Computer Assisted Radiology and Surgery,* vol. 11, pp. 1755-1763, 2016.

[74] G. Claudia, A. Alessandro, N. Francesca, P. S. C., S. Corrado, N. Sara, *et al.*, "Longitudinal MRI quantification of muscle degeneration in Duchenne muscular dystrophy," *Annals of Clinical and Translational Neurology,* vol. 3, pp. 607-622, 2016.

[75] J. N. Kornegay, "The golden retriever model of Duchenne muscular dystrophy," *Skeletal Muscle,* vol. 7, pp. 1-21, 2017.

[76] J. L. Thibaud, A. Monnet, D. Bertoldi, I. Barthelemy, S. Blot, and P. G. Carlier, "Characterization of dystrophic muscle in golden retriever muscular dystrophy dogs by nuclear magnetic resonance imaging," *Neuromuscular Disorders*, vol. 17, pp. 575-584, 2007.

[77] M. Kobayashi, A. Nakamura, D. Hasegawa, M. Fujita, H. Orima, and S. Takeda, "Evaluation of Dystrophic Dog Pathology by Fat-Suppressed T2-Weighted Imaging," *Muscle & Nerve,* vol. 40, pp. 815-826, 2009.

[78] J. L. Thibaud, N. Azzabou, I. Barthelemy, S. Fleury, L. Cabrol, S. Blot*, et al.*, "Comprehensive longitudinal characterization of canine muscular dystrophy by serial NMR imaging of GRMD dogs," *Neuromuscular Disorder,* vol. 22, pp. S85-S99, 2012.

[79] J. Wang, Z. Fan, K. Vandenborne, G. Walter, Y. Shiloh-Malawsky, H. An*, et al.*, "A computerized MRI biomarker quantification scheme for a canine model of Duchenne muscular dystrophy," *International Journal of Computer Assisted Radiology and Surgery,* vol. 8, pp. 763-774, 2013.

[80] I. Barthélémy, F. Pinto-Mariz, E. Yada, L. Desquilbet, W. Savino, and S. D. Silva-Barbosa, "Predictive markers of clinical outcome in the GRMD dog model of Duchenne muscular dystrophy," *Disease Models & Mechanisms,* vol. 7, 2014.

[81] D. Duda, M. Kretowski, N. Azzabou, and J. D. de Certaines, "MRI Texture Analysis for Differentiation Between Healthy and Golden Retriever Muscular Dystrophy Dogs at Different Phases of Disease Evolution," in *Computer Information Systems and Industrial Management*, 2015, pp. 255-266.

[82] G. Yang, V. Lalande, L. Chen, N. Azzabou, T. Larcher, J. D. de Certaines*, et al.*, "MRI Texture Analysis of GRMD Dogs Using Orthogonal Moments: A Preliminary Study," *IRBM,* vol. 36, pp. 213-219, 2015.

[83] J. D. De Certaines, T. Larcher, D. Duda, N. Azzabou, P.-A. Eliat, L. M. Escudero*, et al.*, "Application of texture analysis to muscle MRI: 1-What kind of information should be expected from texture analysis?," *EPJ Nonlinear Biomedical Physics,* vol. 3, pp. 1-14, March 19 2015.

[84] R. A. Lerski, J. D. de Certaines, D. Duda, W. Klonowski, G. Yang, J. L. Coatrieux*, et al.*, "Application of texture analysis to muscle MRI: 2 – technical recommendations," *EPJ Nonlinear Biomedical Physics,* vol. 3, pp. 1-20, 2015.

[85] J. N. Kornegay, J. R. Bogan, D. J. Bogan, M. K. Childers, J. Li, P. Nghiem, *et al.*, "Canine Models of Duchenne Muscular Dystrophy and Their Use in Therapeutic Strategies," *Mammalian Genome,* vol. 23, pp. 85-108, 2012.

[86] R. Gilles, J.-L. Thibaud, M. Toussaint, S. Blot, and P. G. Carlier, "Early detection of contractile dysfunction in GRMD dogs by post-processing of standard cine FLASH-MRI," *Journal of Cardiovascular Magnetic Resonance,* vol. 13, pp. 1-2, 2011.

[87] W. T. Triplett, C. Baligand, S. C. Forbes, R. J. Willcocks, D. J. Lott, S. DeVos, *et al.*, "Chemical shift-based MRI to measure fat fractions in dystrophic skeletal muscle," *Magnetic Resonance in Medicine,* vol. 72, pp. 8-19, 2014.

[88] M. Kiichiro, N. Imaharu, F. Nobuo, I. Hiroo, T. Yukio, and A. Yoshiro, "Protron spin-lattice relaxation time of duchenne dystrophy skeletal muscle by magnetic resonance imaging," *Muscle & Nerve,* vol. 11, pp. 97-102, 1988.

[89] F. A. Marden, A. M. Connolly, M. J. Siegel, and D. A. Rubin, "Compositional analysis of muscle in boys with Duchenne muscular dystrophy using MR imaging," *Skeletal Radiology,* vol. 34, pp. 140-148, 2005.

[90] G. C. Liu, Y. J. Jong, C. H. Chiang, and T. S. Jaw, "Duchenne muscular dystrophy: MR grading system with functional correlation," *Radiology,* vol. 186, pp. 475-480, 1993.

[91] C. Brinkmeyer-Langford and J. N. Kornegay, "Comparative Genomics of X-linked Muscular Dystrophies: The Golden Retriever Model," *Current Genomics* vol. 14, pp. 330-342, 2012.

[92] S. C. Forbes, G. A. Walter, W. D. Rooney, D.-J. Wang, S. DeVos, J. Pollaro, *et al.*, "Skeletal Muscles of Ambulant Children with Duchenne Muscular Dystrophy: Validation of Multicenter Study of Evaluation with MR Imaging and MR Spectroscopy," *Radiology,* vol. 269, pp. 198-207, 2013.

[93] D. J. Lott, S. C. Forbes, S. Mathur, S. A. Germain, C. R. Senesac, H. Lee Sweeney, *et al.*, "Assessment of intramuscular lipid and metabolites of the lower leg using magnetic resonance spectroscopy in boys with Duchenne muscular dystrophy," *Neuromuscular Disorders,* vol. 24, pp. 574-582, 2014.

[94] C. A. Collins and J. E. Morgan, "Duchenne's muscular dystrophy: animal models used to investigate pathogenesis and develop therapeutic strategies," *International Journal of Experimental Pathology,* vol. 84, pp. 165-172, 2003.

[95] J. N. Kornegay, C. F. Spurney, P. P. Nghiem, C. L. Brinkmeyer-Langford, E. P. Hoffman, and K. Nagaraju, "Pharmacologic management of Duchenne muscular dystrophy: target identification and preclinical trials," *ILAR Journal*, vol. 55, pp. 119-149, 2014.

[96] P. Garrood, K. G. Hollingsworth, M. Eagle, B. S. Aribisala, D. Birchall, K. Bushby, *et al.*, "MR imaging in Duchenne muscular dystrophy: quantification of T1-weighted signal, contrast uptake, and the effects of exercise," *Journal of Magnetic Resonance Imaging,* vol. 30, pp. 1130-1138, 2009.

[97] M. Rusu, H. Wang, T. Golden, A. Gow, and A. Madabhushi, "Multiscale multimodal fusion of histological and MRI volumes for characterization of lung inflammation," in *Medical Imaging 2013: Biomedical Applications in Molecular, Structural, and Functional Imaging,* Lake Buena Vista (Orlando Area), Florida, USA, 2013.

[98] N. Aggarwal and R. K. Agrawal, "First and Second Order Statistics Features for Classification of Magnetic Resonance Brain Images," *Journal of Signal and Information Processing,* vol. 3, pp. 146-153, 2012.

[99] R. M. Haralick, K. Shanmugam, and I. H. Dinstein, "Textural features for image classification," *IEEE Transactions on Systems, Man, and Cybernetics,* vol. SMC-3, pp. 610-621, 1973.

[100] M. M. Galloway, "Texture analysis using gray level run lengths," *Computer Graphics and Image Processing,* vol. 4, pp. 172-179, 1975.

[101] A. Eresen, S. McConnell, S. M. Birch, J. F. Griffin, J. N. Kornegay, and J. X. Ji, "Localized MRI and histological image correlation in a canine model of duchenne muscular dystrophy," *Conf Proc IEEE Eng Med Biol Soc*, vol. 2016, pp. 4083-4086, Aug 2016.

[102] A. Eresen, S. McConnell, S. Birch, W. Friedeck, J. Griffin, J. Kornegay, *et al.*, "Correlating MRI and Histological Parameters in GRMD Muscles: A Comparison Between 3T and 4.7T Acquisitions," presented at the ISMRM, Honolulu, HI, USA, 2017.

[103] A. Eresen, S. McConnell, S. M. Birch, J. F. Griffin IV, J. N. Kornegay, and J. X. Ji, "Tissue classification in a canine model of Duchenne Muscular Dystrophy using quantitative MRI parameters," in *39th Annual International Conference of the IEEE Engineering in Medicine and Biology Society (EMBC),* Seogwipo, South Korea, 2017.

CHAPTER II

NEW SIMILARITY METRIC FOR REGISTRATION OF MRI TO HISTOLOGY: GOLDEN RETRIEVER MUSCULAR DYSTROPHY IMAGING

Duchenne muscular dystrophy is a fatal X-linked muscle disorder affecting ~1 in 4000-6000 newborn males [1]. Affected boys have mutations in the DMD gene, which results in absence of cytoskeletal protein dystrophin and progressive degeneration of skeletal and cardiac muscles [2]. Golden retriever muscular dystrophy is a spontaneous X-linked canine model of DMD, with affected dogs developing a progressive, fatal disease similar to the human condition [3, 4]. As a genetically homologous animal model, GRMD has increasingly been used in therapeutic preclinical trials [3, 4].

Current outcome measures in DMD are suboptimal. Muscle biopsy, used to provide the ground-truth information, is invasive and limited in its coverage by specimen size. Functional and muscle strength assessments are susceptible to rater variability [5, 6]. MRI is commonly used as a non-invasive alternative to providing meaningful information on disease progression and treatment response [6-20]. Although earlier studies identified various MRI biomarkers based on whole muscle volumes, they lacked an adequate validation procedure [6-10, 15-19]. Thorough understanding of the MRI biomarkers of DMD involves an accurate spatial correlation of MRI and histology, offering means to verify MRI findings. On the other hand, to create histological images, a muscle sample must be processed through multiple steps: biopsy, fixation by formalin followed by dehydration, paraffin embedding, sectioning, and rehydration during staining. An important side effect of this process is the significant tissue deformation, which inevitably changes tissue appearance. This severely complicates the registration of MRI to histological images. The registration is additionally complicated by inherent differences in image intensity and resolution between histological color images and grayscale MRI images.

The field of multi-modality registration has evolved considerably in recent years. Still, the literature specifically dealing with registration of histology to MRI is limited. The first attempts to register histology and MRI were part of an effort to establish brain atlases, starting with affine registration [21] and advancing to piece-wise affine models [22]. Although affine registration achieved good initial results in these applications, it was inadequate to deal with non-linear distortions that occur during tissue excision and histological processing. Elastic registration to link MRI with histology using surface matching has also been considered but has been limited to the global matching of MRI volumes [23, 24].

Other studies of point-based registration using manually placed landmarks [25] are time-consuming and prone to inter-observer variability due to human interaction. These methods have been divided into three general categories: 3D-to-3D, 2D-to-2D and 2D-to-3D registration [26-28]. The first category, 3D-to-3D, registers consecutive histology images to reconstructed color 3D histology data sets and registers these to either ex vivo MRI or in vivo MRI [29-32] with a maximum registration accuracy of 0.7-3 mm. These studies have been used to register pancreatic tumors [29], prostate [30, 31] and lungs [32]. The second category of methods, 2D-to-2D, employs a histology to MRI slice registration in a 2D manner [33, 34]. Histologic images were registered to in vivo MRI images of the human prostate with an accuracy of 0.91%-0.93% assessed by dice similarity. The last category of registration methods, 2D-to-3D, is based on aligning a single 2D histology image with a 3D volume [23, 35-38]. The 2D histology images of brain [35, 36], prostate [37], and bone grafts [38] were registered to ex vivo [35-38] or in vivo [23, 37] volumes. These publications use a different level of registration complexity ranging from rigid [36], through point matching [23], to full elastic registration [35, 37]. All these publications require manual initialization, with manual [23, 37] or automatic [23, 35] annotation of whole organ [23, 37] or internal landmarks [23]. However, all the publications lack a comprehensive and detailed validation of registration accuracy. They evaluate the quality of the registrations by a similarity measure to assess global alignment [36, 37], by evaluation of the size of a specific region [23], by comparison to manual position [38], or by use of anatomical landmarks [35].

Intensity-based similarity metrics and optimization algorithms are used to evaluate registration performance. In cases of multi-modal registrations, differences in image acquisition mechanisms produce analogous changes in image content [36]. Therefore, the similarity metric is critical for a successful multi-modal registration. Among various similarity metrics used for image registration [27, 28, 36, 39], mutual information is most frequently used in multi-modal image registrations [27, 28], especially for medical images [26]. However, the structural information is not sufficiently reflected in the MI, potentially leading to inaccurate registrations. An attempt to use an internal structure in a multi-modal images registration process proposed utilization of the normalized gradient field as a metric [40]. When tested under perfectly controlled environment, NGF produced good registration results for the affine linear transformation. Unfortunately, its performance tends to decrease in applications with large elastic deformations. In addition, registration accuracy is massively affected by the initial position of the 2D histology image due to an optimization problem during the registration process. Careful specimen preparation and cutting plane positioning can help alleviate this problem [41].

To overcome these limitations and to provide accurate registration between 2D histology images and 3D MRI volume, we propose a registration framework based upon interactive initialization in 3D MRI volume [42] and a gradient-based addition to the MI metric. The experimental setup ensures detection of the angle and position of a 2D histology image. Employing such extensive measures is essential to find the 3D orientation of skeletal muscle specimens.

The aim of this work was to develop a slice-to-volume registration framework that can reliably and efficiently align a single histology image with a 3D MRI volume acquired from ex vivo normal and pathological skeletal muscle samples. Specifically, an interactive procedure using a 3D mouse was implemented to determine the initial position of the 2D histology images in the 3D space of the cross-sectional MRI slices. In addition, a new similarity metric was proposed combining mutual information and local gradient information.

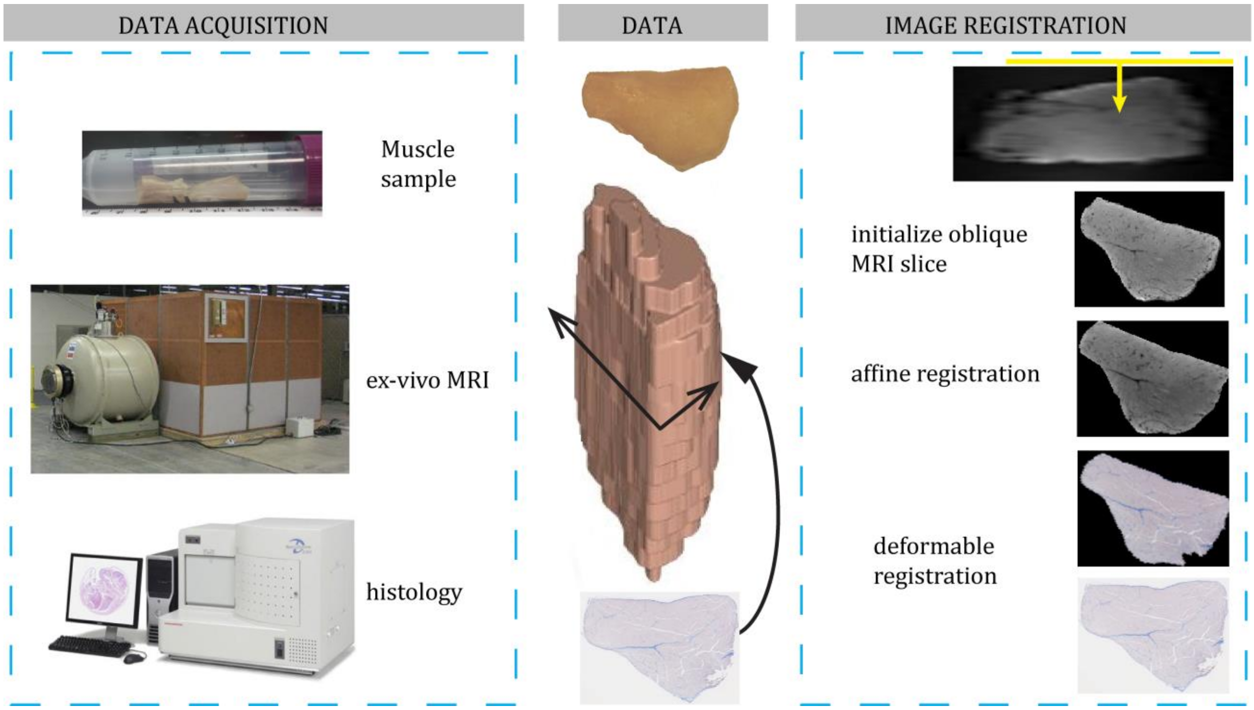

Figure 2.1. Overview of the data processing and image registration steps. The initial location of the histology image is determined via user guidance. Then, affine and elastic transformation models are used for registration

Materials and Methods

Figure 2.1 is a schematic overview of the proposed registration methodology, consisting of initialization, followed by affine and elastic registration of the MRI and histology data. The proposed methodology starts with pre-processing histology and MRI data. Subsequently, an interactive alignment and affine transformation are used to produce the most likely orientation of the MRI slice to match the histological image. Finally, a non-rigid B-spline transformation is used to refine the registration between 3D MRI volume and histology image.

All datasets were processed by the same procedure detailed in the foregoing section using an in-house developed software based upon Matlab® (Version 9.1.0, MathWorks Inc., Natick, Massachusetts, USA). Different registration steps were performed using either Matlab® or Elastix (Version 4.8) [43].

Animals

Studies were completed on dogs from a colony maintained at Texas A&M University and were approved by the Institutional Animal Care and Use Committee protocol (2015-01110) under established standards [44, 45]. Pectineus muscles were taken at necropsy from 9 GRMD [4] and one healthy dog. The canines ranged between 3 and 48 months in age, i.e., three 3 months old, two 12 months old, one each 15, 18, 42, and 48 months old, and one healthy adult dog. The pectineus muscle samples (average size 12 mm × 20 mm × 45 mm) were extracted and fixed at their resting length. They are stored in formalin-filled containers prior to MRI acquisitions. On MRI imaging day, they are removed from the containers and prepared for MRI imaging.

Image Acquisition

MRI

A 40 cm bore 4.7T Varian Bruker scanner equipped with enhanced gradient system and an in-house developed birdcage coil was used for image acquisitions over a 30 mm × 30 mm field of view and a matrix size of 256 × 256 [46]. The T_1-weighted images were acquired with $T_R = 268$ ms, $T_E = 6.1$ ms, FA = 72°, and 4 averages using a conventional gradient echo sequence. The T_2-weighted images were acquired with $T_R = 3$ s, $T_E = 40$ ms and 1 average using conventional spin echo MRI sequence. Twenty transverse slices were acquired at a resolution of 117.19 µm × 117.19 µm × 1 mm.

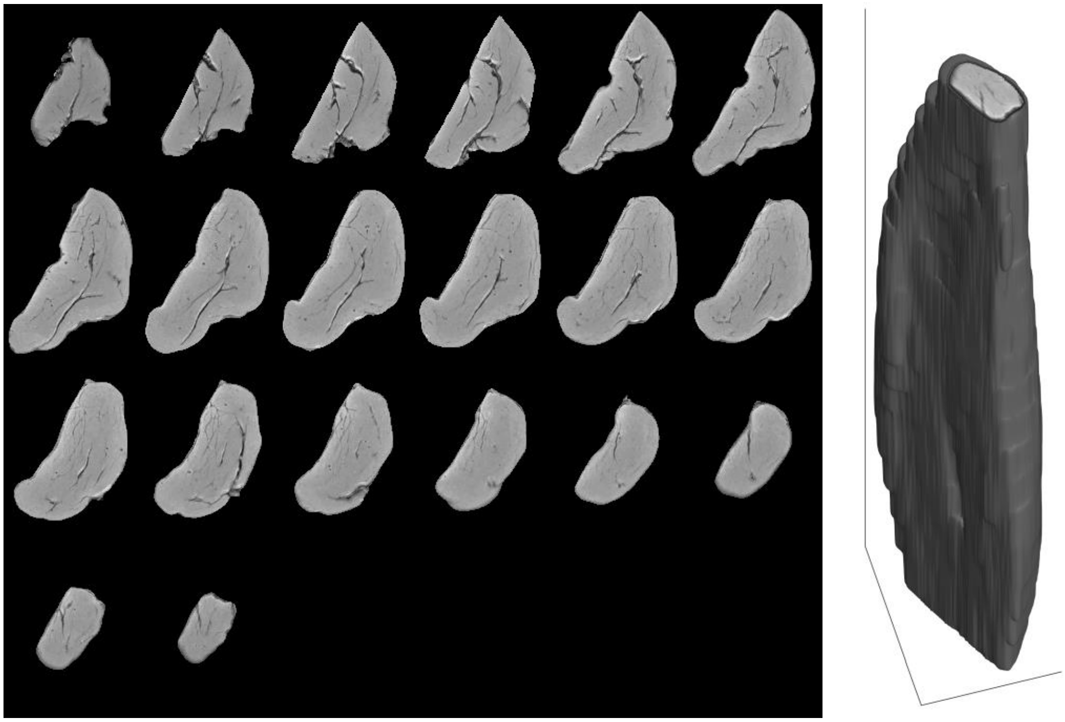

Figure 2.2. A representative set of T_1-weighted images of a GRMD dog muscle and the 3D rendering of same muscle volume

Histology

Before imaging, each sample was removed from formalin, rinsed with saline, dried, and placed into a 50-ml centrifuge tube. To reduce potential motion artifacts caused by vibrations occurring during high-resolution MRI scans, tubes were filled with agarose gel (0.8 gr of Agarose [Apex, USA] with 100-ml of plain water). When MRI images acquired, samples are removed from the containers and cleaned to prepare for sectioning. A muscle block is generated from each muscle in the middle. Two consecutive (5 μm) slices were cut from midsection using a microtome. The sections were stained with Masson's trichrome dye, which stains skeletal muscle tissue red/pink, fibrotic tissue (including collagen) blue, and fat or areas of tissue separation voids clear (appears white in images) [47]. The slides were digitally scanned (Hamamatsu NanoZoomer 2.0-HT pathology scanner) at 40x optical zoom and stored in a (tailed) proprietary image file format with a maximum pixel resolution of 0.23 μm.

Image Pre-processing

MRI

After MRI images acquired, they are inspected to identify potential artifacts. The mask images were required to remove background effects and define an interested region in MRI slices. The MRI masks for each slice were generated from T_1w images by using local adaptive thresholding method [48] and then refined by a morphological binary operation (opening) followed by active contour algorithm with 15 iterations [25, 26]. A representative set of twenty T_1w MRI slices (left) and the 3D rendering of the MRI volume (right) are presented in Figure 2.3.

Histology

Differences in resolution between histology images and MRI increases the computational complexity and may hamper convergence of the registration procedure [49]. To match the MRI resolution more accurately, histology images were exported from the proprietary image format at 10x optical zoom resolution (pixel size 0.93 µm) using NDPITools [50].

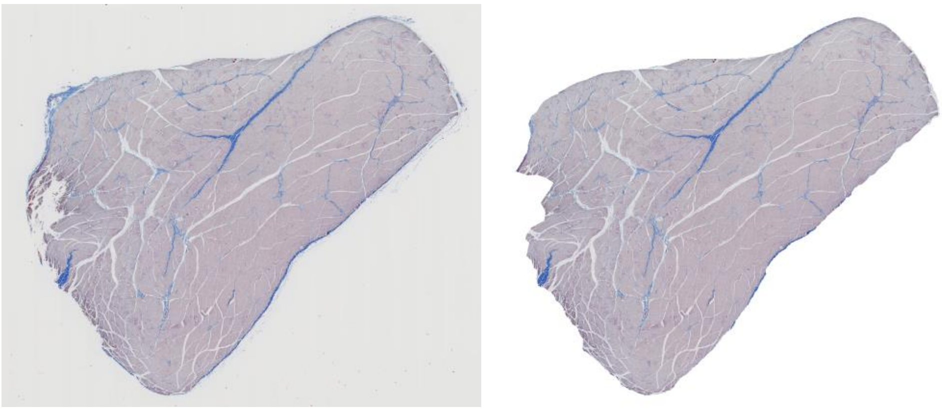

Figure 2.3. Original histology slice (left) and masked version (right)

Due to histologic processing, histology sections may have a range of artifacts, including stain clumping, tissue separation along facial planes, and/or tissue folding [51]. To minimize the influence of artifacts on registration quality, a histology mask for each sample was generated automatically in down-sampled images (pixel size 0.93 µm) by employing Otsu's global threshold [52]. This segmentation was pruned by morphological operations (erosion and dilation) and refined by an active contour method with 150 iterations for each individual sample [53]. A representative raw and masked histology images are presented in Figure 2.3.

Trichrome stained histology images contain three color channels (RGB) to represent skeletal muscle (red/pink), fibrotic tissue and collagen (blue) and fat/non-staining background (usually appearing clear/white in images) [47]. To optimally exploit the information in histology images, considering the fibrosis and muscle tissue, the information content of separate image channels and transformed image models were evaluated. In the registration procedure, we used the hue-component in the registration process as it provides the best separation between signal intensities of tissues of interest and presumably the best image contrast. After the final registration step, each transformation was applied on all components to reconstruct a co-registered RGB color image.

Image Registration

By processing of histology sections, muscle sample undergoes the deformation with respect to its original shape imaged by MRI. To compensate for the deformation between 3D-MRI and histology image, we developed a registration framework consisting of three distinct steps:

1) Interactive alignment
2) Slice-to-volume affine registration
3) Slice-to-slice non-rigid registration

For the two latter registration steps, multi-parametric MRI (consisting of T_1w and T_2w MR and corresponding mask) was used as a fixed image, while the hue-component of the histology image (and corresponding mask) was used as a moving image. A similarity metric for medical registration problems, mutual information (MI), is a global measure and does not consider the local image gradients. Local image structures such as edges can be effectively captured using a Laplacian filter. To overcome the limitations of MI, we employed a new similarity metric combining mutual information and correlation of local structure in the images, referred to as MIC.

$$S\left(I_1, I_2\right) = M_1\left(I_1, I_2\right) + M_2\left(L_1, L_2\right) \tag{2.1}$$

where I_1 is the multi-parametric MRI slice, I_2 is the hue-component of the histology image, L_1 is the corresponding multi-parametric MRI slice (I_1) after Laplacian filtering (kernel size of 3), and L_2 is hue-component of the histology image (I_2) after Laplacian filtering (kernel size of 3). M_1

is the mutual information [54] between I_1 and I_2, and M_2 is the Pearson's correlation [55] between L_1 and L_2.

Mutual information between the MRI and histology images was computed separately for both sequences in multi-parametric MRI, i.e., T_1w versus histology, and T_2w versus histology. Correspondingly, Pearson correlation was calculated independently for both T_1w and T_2w sequences. The calculated four metrics were weighted equally to compute the similarity measure between MRI and histology.

Step 1: Interactive Alignment

The objective of this step was to define an oblique MRI slice with the highest correlation to the histology image as validated by an observer. Achieving the global alignment in this step helps to avoid local registration minima and facilitate fast and efficient convergence of the subsequent registration steps. In our previous work, an interactive alignment procedure was developed using a smartphone as a control device [42]. In this study, we substituted the smartphone with a 3D mouse (SpaceNavigator, 3DConnexion, USA) as it enables oblique slice selection in an efficient yet user-friendly approach. This allowed for simultaneous control of six degrees of freedom, i.e., rotation, translation, plus the zoom and pan actions. The user is provided with visual feedback in the form of two fused color overlays, both consisting of the current raw MRI slice overlaid by the raw histologic image.

Interactive alignment procedure generates the oblique MRI slice interpolated using a cubic kernel (FOV: 300 pixels × 300 pixels) and a pixel size of 117.19 µm × 117.19 µm × 0.10 mm. Additionally, this step registers the histology image with four degrees of freedom. We initiated the registration by using four different oblique slices in MRI defined by four observers independently.

The registration process was completed separately for each parameter set determined by different users.

Step 2: Slice-to-Volume Affine Registration

For this iterative step, we used Matlab®. The oblique MRI plane, defined during interactive alignment, was used to initialize the optimization algorithm to search through the MRI volume iteratively by applying translation and rotation. During this process, rotation angles were limited to 30º and translation parameters to 10 mm. Simultaneously, the histology image was scaled in both directions. To avoid local registration minima and to decrease computation time, an optimization scheme was used based upon pattern search algorithm [56]. The PS algorithm generates a grid around the initialized point with the boundary constraints for each parameter to be optimized and then using an adaptive method to change the direction of scaling with step size. The PS algorithm stops when one of the following conditions is met: the mesh size is less than 10^{-3}; the number of iterations is greater than 800; the number of function evaluations is more than 14k, or the change of the proposed similarity metric is less than 10^{-4}.

Step 3: Slice-to-Slice Non-Rigid Registration

Non-rigid registration in this step was completed by utilizing Elastix [43]. A B-spline deformable registration with a three-level image-pyramid was used to minimize deformations. An adaptive stochastic gradient descent algorithm was selected for optimization of the deformable transformation parameters with the proposed similarity metric for non-rigid registration. The control points for B-spline transformation were placed every 10 pixels in each direction and were re-positioned (during the registration process) according to the registration accuracy. The stopping criterion was selected as a similarity metric with a value less than 10^{-6}. The proposed similarity metric was utilized during the non-rigid registration step.

Evaluation of Registration Accuracy

To validate the proposed metric, compared to classical mutual information, we have evaluated the registration accuracy for both metrics separately. Furthermore, the benefit of multi-modal registration approach was also evaluated by performing three registration experiments (for each metric) using different MRI data: T_1w, T_2w, and the combination of T_1w and T_2w. For all separate registrations, four observers used visual inspection with a moving quadrant view for qualitative evaluation of the resulting alignment. In addition, the registration was quantitatively evaluated using the distance from anatomical landmarks (e.g., characteristic features in the skeletal muscle sample) for all individual registration experiments separately. For the quantitative evaluation of each sample, five clearly identifiable anatomical landmark points were defined before registration by an experienced observer on the histology image. Subsequently, after final registration, five observers independently annotated the corresponding anatomical landmark points in MRI for each registration experiment and for all 10 samples. To evaluate registration accuracy, the root mean squared distance between the corresponding landmark points in MRI and the histology was calculated after all three registration steps separately. For each registration and each observer, we averaged all landmark points and evaluated for four different registrations. The selected landmark locations on the MRI image were transformed back to previous steps to calculate the RMS distance of earlier steps. Additionally, the inter-observer variability was estimated by computing the RMS distance between the corresponding landmark points (in each sample independently) for all five observers after the final registration step.

Evaluation of Reference Plane

The reference plane greatly facilitates the registration procedure. Differences in reference plane position between the two images, after the second step in the registration procedure, measured the initial reference plane error. To quantify the error in reference plane positioning, the out-of-plane angulation was estimated as the rotation component of the rigid registration for the second step. The effects of the out-of-plane angular change on final registration step was investigated using statistical analyses defined in the next section.

Surface Change

Global surface change of the histology image was established by computing the determinant of the corresponding transformation for the second step and the third step:

$$\Delta A = 2\frac{|A_r - A_o|}{|A_r + A_o|} \tag{2.2}$$

where A_o, and A_r represent the cross-sectional area before and after registration, respectively.

Statistical Analysis

Random effects models were fitted with the RMS as the dependent variable and the Bootstrap Information Criterion (BIC) was used for model selection. The model parameters were estimated through restricted maximum likelihood estimation. Likelihood ratio tests were used to compare the differences between the effects of the three steps. Residuals were checked for the goodness of fit of the models. Statistical analysis was performed using R version 3.3.3 (2017 The R Foundation for Statistical Computing). Furthermore, the Cohen’s d effect size was calculated between the first two steps of the registration procedure. To summarize the data, mean and standard deviation were calculated for each step and user.

Table 2.1. Average root mean squared distances (pixels) for the different registration steps for all registration experiments averaged over all 10 samples and for all four initializations. Detailed results of RMS measures after step 2 and after step 3 are presented in Table A1 (Appendix A). (MI: Mutual information, MIC: Proposed similarity metric)

Similarity Metric	MRI image	Step 1	Step 2	Step 3
MI	T_1w	4.36±1.87	4.40±0.60	4.80±0.75
	T_2w		4.65±0.47	4.87±0.52
	T_1w & T_2w		4.55±0.39	4.83±0.46
MIC	T_1w	4.36±1.87	4.29±0.37	3.78±0.62
	T_2w		4.11±0.60	3.52±1.18
	T_1w & T_2w		3.11±0.37	1.27±0.75

Results

Evaluation of Registration Accuracy

The proposed registration framework was used to register pectineus muscle samples from 10 dogs (nine GRMD and one normal) for both metrics (using MI and MIC) separately. The quantitative evaluation (registration error) is presented in Table 2.1 as RMS distance averaged over the ten samples after all registration steps for all registrations, and with different MRI images (T_1w, T_2w, and the combination of T_1w and T_2w). For proposed registration framework (including MI and dual MRI), RMS distance (presenting maximum accuracy among four initializations) was provided in the Table A1 (Appendix A) for all samples separately. For three samples, one landmark point (selected in the histology image before the registration) was not visible in MRI after the final registration step. For these three samples, we averaged the RMS for remaining four landmark points.

In case of MI metric, the registration accuracy remained unchanged regardless of the increase in the degree of freedom or data input. However, in case of MIC metric, the registration accuracy clearly increased with additional MRI sequences. The average RMS decreased from 4.36 pixels (511.49 µm) after the first step to 1.27 pixels (148.83 µm) after the third step. Besides increasing accuracy by decreasing registration error, we also observed a significant decrease in variance after the third step for all samples. On average, the final accuracy of 148.83 µm corresponds to a surface populated by 3-15 healthy muscle cells [57]. The supplementary table shows the detailed results for all ten samples and all four observers separately for an experiment using MIC metric and a combination of T1w and T2w MRI. The best out of four registrations for each sample yielded the RMS error of 128.48 ± 25.39 µm (averaged for all 10 skeletal muscle samples). There was no significant difference in registration accuracy between the healthy sample (RMS distance of 125.67 µm) and diseased samples with an average RMS distance of 128.79 µm.

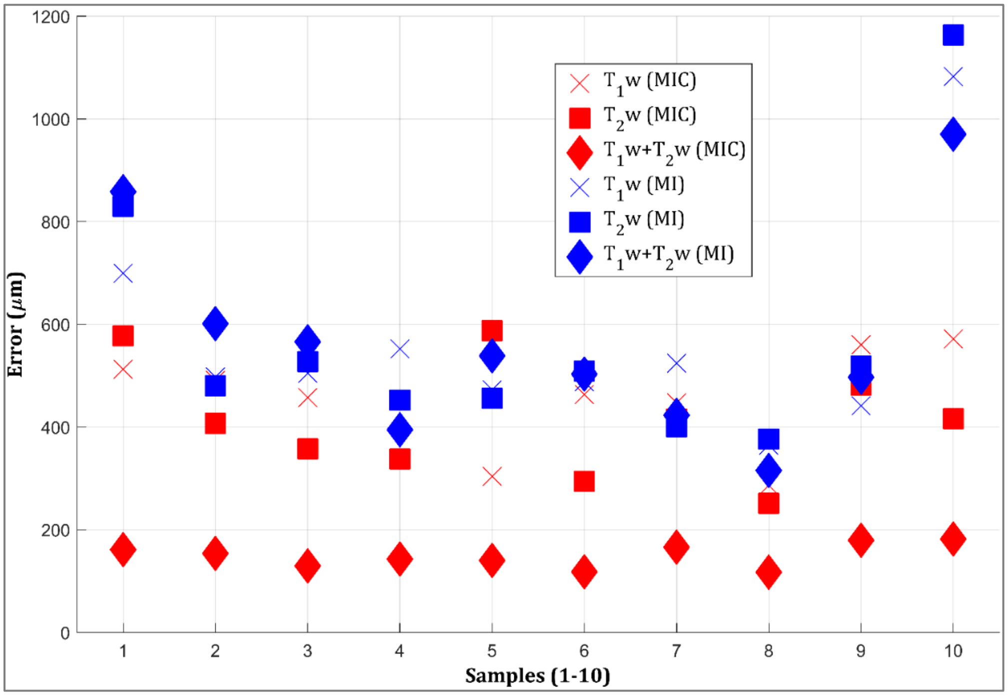

Figure 2.4. The RMS error for all individual samples averaged over five landmark points except samples 1, 3, 10 (4 landmark points) for all four registrations, five observers, and all six different registration experiments.

Figure 2.4 illustrates the RMS error for all ten samples individually as assessed by five observers independently. A significant decrease in RMS distance was observed between every step of the registration process.

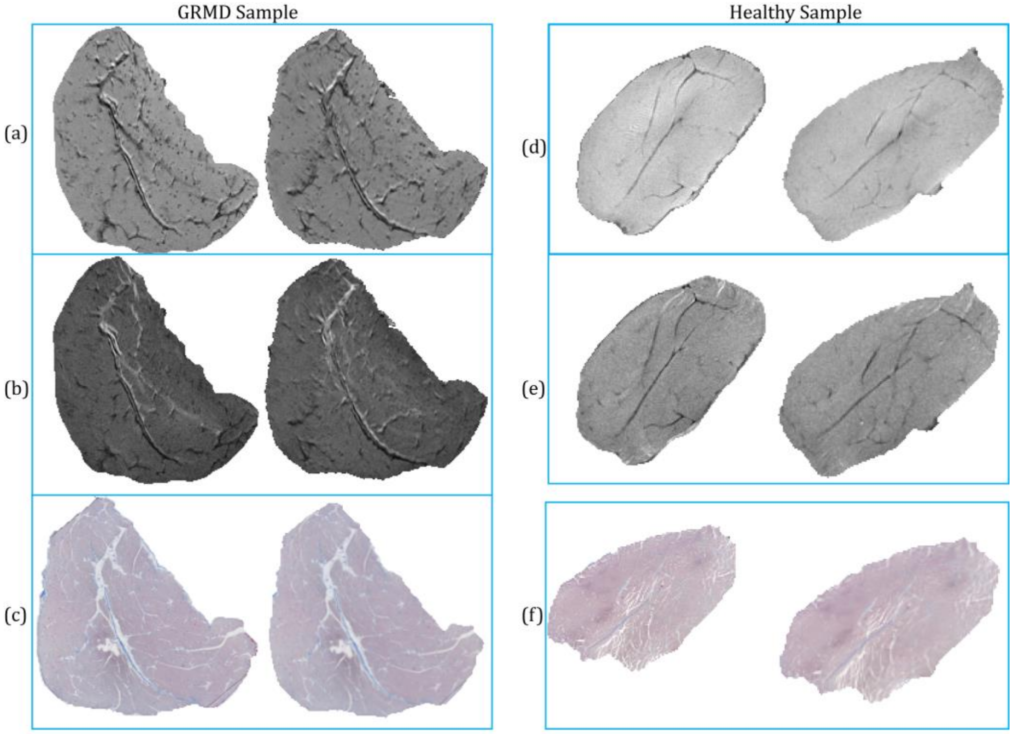

Figure 2.5. Final registration results for GRMD (left panel) and normal dog (right panel) samples. In each group, the left image presents the initial image and the registered image is shown on the right. T_1-weighted, T_2-weighted and histology images of the GRMD (a, b, and c) and normal dog (d, e, and f), respectively, are shown.

For proposed registration framework (including MI and dual MRI), we assessed the uncertainty of manual annotations by the inter-observer variability as RMS error for all corresponding landmark points (in MRI) and for each landmark point in histology. The inter-observer variability after the final registration step was assessed at 1.5 ± 0.83 pixels. Resulting original and post-registration images were illustrated for two samples: GRMD (Figure 2.5-left) and normal (Figure 2.5-right) with Figure 2.6 detailing the registration results. The checkerboard views illustrate a good alignment for the registered histology image with 3D-T_1w MRI (Figure 2.6-left), and 3D-T_2w MRI (Figure 2.6-right).

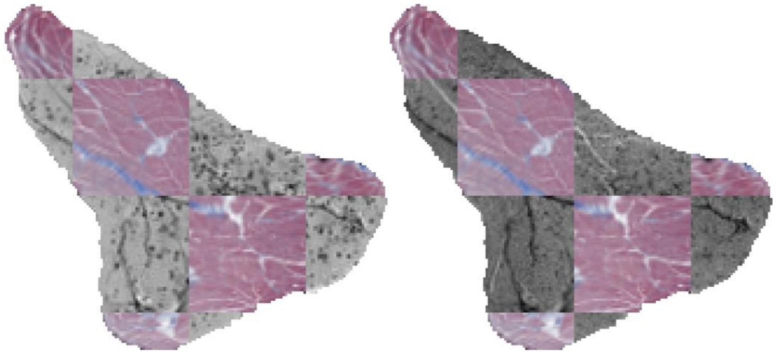

Figure 2.6. Checkerboard images of the sample show the matching curved line structure of histology and T_1w MRI images (left) and of histology and T_2w MRI (right). The figure illustrates the results of the proposed registration framework (including MIC and dual MRI).

The statistical analysis of the registration accuracy showed no significant effect of the initial orientation of the oblique MRI slice to the final registration. The users (initializing the registrations by choosing an oblique MRI slice) were statistically modeled with both as a fixed effect (p=0.08) and as a random effect (p=0.27). Furthermore, Cohen's d-effect size of 1.153 was assessed between the first two steps of the registration procedure.

Table 2.2. The angulation difference after first and second steps of the registration process averaged for all four registrations and all ten samples

	Step 1 $\lvert\theta^{\circ}\rvert$	Step 2 $\lvert\theta^{\circ}\rvert$
Average	4.36	5.64
Minimum	0.00	0.00
Maximum	15.00	21.02

Table 2.3 Summarized surface change in histology images averaged for all four registrations

	after 1st step		after 2nd step		after 3rd step	
	ΔA (%)	abs(ΔA)	ΔA (%)	abs(ΔA)	ΔA (%)	abs(ΔA)
sample 1	7.4	7.4	-1.57	1.57	-6.28	6.28
sample 2	-9.9	9.9	-1.48	1.48	-6.74	6.74
sample 3	-16.8	16.8	-1.97	1.97	-5.53	5.53
sample 4	0.0	0.0	-0.86	1.24	-3.66	3.66
sample 5	-20.8	20.8	-2.96	2.96	-1.23	2.53
sample 6	-4.6	4.6	-0.22	0.22	-1.48	2.77
sample 7	0.0	0.0	-1.13	2.04	-1.51	2.80
sample 8	-10.2	10.2	0.05	0.66	-2.48	3.77
sample 9	-8.1	8.1	-0.21	0.81	-3.33	3.33
sample 10	24.1	24.1	-0.24	0.24	-2.77	2.77
average	-3.9	10.2	-1.1	1.3	-3.5	4.0
min	-20.8	0.0	-3.0	0.2	-6.7	2.5
max	24.1	24.1	0.0	3.0	-1.2	6.7

Evaluation of Reference Plane

The angular change in the reference plane (θ^o) was assessed after the first step and second step in the registration process. Table 2.2 shows the average absolute reference plane compared to original MRI orientation. To determine the relationship between angulation difference and registration accuracy after each step, random effects models were fitted with registration accuracy as the dependent variable. The results showed that the angulation difference was not significant on the registration accuracy calculated after first and second steps of the framework (p=1.0). Furthermore, there was no significant difference between the steps (p=0.2018).

Histological Surface Change

On average, the cross-sectional area of the histology images decreased after final registration by 3.5% (this change ranged between 1.2% and 6.7%). The same decreasing trend was observed for all samples. Table 2.3 showed the change in cross-sectional area for the ten samples as average for all four independent registration experiments.

Discussions and Conclusions

Noninvasive tools for skeletal muscle evaluation are critically needed to assess MRI in therapeutic protocols for muscular dystrophy and other myopathies. Therefore, it is essential that the selected biomarkers are robust in detecting (small and subtle) differences between degrees of muscle involvement.

In this study, we present a multi-modality registration scheme with a new similarity metric to co-register histology with MRI. The proposed method features a 3D mouse-controlled slice localization to select a slice orientation as a starting point for registration. Another unique feature of the method is the similarity metric that combines mutual information and local gradients. Specifically, multi-modal MRI and Laplacian histology hue-images were used for the registration to incorporate local texture information. Both T_1w and T_2w MRI images were included in the similarity metric calculation. The proposed metric, between MRI and histology images, was calculated for T_1w and T_2w MRI separately and was equally weighted during affine and deformable registrations. We performed four separate registrations for each sample, each one with an oblique plane initiated by a different observer independently. The registration quality, evaluated by remaining RMS error, demonstrated the superiority of MIC to MI that is considered a state-of-the-art distance measure for multi-modal image registration. During evaluation of the registration accuracy, visible structures were validated qualitatively and quantitatively by assessing the inner anatomical landmarks based on RMS distances. The results were evaluated by five observers to reduce bias in the manual selection of landmarks after the registrations. The average registration accuracy was evaluated to 148.83 µm (1.27 pixels) after the final registration step with an inter-observer variability of 1.5 ± 0.83 pixels. This demonstrated the average accuracy was slightly under the inter-observer variability. However, when compared to the best out of four registrations for each sample (128.48 ± 25.39 µm), the registration accuracy was well under the inter-observer variability.

This study represents a successful and efficient initial step to establish a registration method to align a single histology image with 3D MRI volume data, enabling extraction of histology validated imaging biomarkers of GRMD skeletal muscle. The quantitative registration results show that the proposed method can be used to register different modality images successfully with low misalignment errors. Eventually, data obtained with this process should provide a better understanding of the effects of GRMD on skeletal muscle in preclinical treatment trials. This will allow accurate monitoring of disease progression and assessment of treatment effects without highly invasive biopsy procedures.

References

[1] J. R. Mendell, C. Shilling, N. D. Leslie, K. M. Flanigan, R. al-Dahhak, J. Gastier-Foster, *et al.*, "Evidence-based path to newborn screening for Duchenne muscular dystrophy," *Annals of Neurology,* vol. 71, pp. 304-313, 2012.

[2] S. Guiraud, A. Aartsma-Rus, N. M. Vieira, K. E. Davies, G.-J. B. van Ommen, and L. M. Kunkel, "The pathogenesis and therapy of muscular dystrophies," *Annual Review of Genomics and Human Genetics,* vol. 16, pp. 281-308, 2015.

[3] C. Brinkmeyer-Langford and J. N. Kornegay, "Comparative Genomics of X-linked Muscular Dystrophies: The Golden Retriever Model," *Current Genomics,* vol. 14, pp. 330-342, 2012.

[4] J. N. Kornegay, "The golden retriever model of Duchenne muscular dystrophy," *Skeletal Muscle,* vol. 7, pp. 1-21, 2017.

[5] A. Lerario, S. Bonfiglio, M. Sormani, A. Tettamanti, S. Marktel, S. Napolitano, *et al.*, "Quantitative muscle strength assessment in duchenne muscular dystrophy: longitudinal study and correlation with functional measures," *BMC Neurology,* vol. 12, pp. 1-8, 2012.

[6] J. L. Thibaud, N. Azzabou, I. Barthelemy, S. Fleury, L. Cabrol, S. Blot, *et al.*, "Comprehensive longitudinal characterization of canine muscular dystrophy by serial NMR imaging of GRMD dogs," *Neuromuscular Disorder,* vol. 22, pp. S85-99, 2012.

[7] J. N. Kornegay, J. R. Bogan, D. J. Bogan, M. K. Childers, J. Li, P. Nghiem, *et al.*, "Canine Models of Duchenne Muscular Dystrophy and Their Use in Therapeutic Strategies," *Mammalian Genome,* vol. 23, pp. 85-108, 2012.

[8] K. G. Hollingsworth, P. Garrood, M. Eagle, K. Bushby, and V. Straub, "Magnetic resonance imaging in duchenne muscular dystrophy: Longitudinal assessment of natural history over 18 months," *Muscle & Nerve,* vol. 48, pp. 586-588, 2013.

[9] S. Ponrartana, L. Ramos-Platt, T. A. L. Wren, H. H. Hu, T. G. Perkins, J. M. Chia, *et al.*, "Effectiveness of Diffusion Tensor Imaging in Assessing Disease Severity in Duchenne Muscular Dystrophy: Preliminary Study," *Pediatric Radiology,* vol. 45, pp. 582-589, 2015.

[10] C. Wary, N. Azzabou, C. Giraudeau, J. L. Louër, M. Montus, T. Voit, *et al.*, "Quantitative NMRI and NMRS Identify Augmented Disease Progression After Loss of Ambulation in Forearms of Boys with Duchenne Muscular Dystrophy," *NMR in Biomedicine,* vol. 28, pp. 1150-1162, 2015.

[11] M. Kobayashi, A. Nakamura, D. Hasegawa, M. Fujita, H. Orima, and S. Takeda, "Evaluation of Dystrophic Dog Pathology by Fat-Suppressed T2-Weighted Imaging," *Muscle & Nerve,* vol. 40, pp. 815-826, 2009.

[12] J. N. Kornegay, D. D. Cundiff, D. J. Bogan, J. R. Bogan, and C. S. Okamura, "The Cranial Sartorius Muscle Undergoes True Hypertrophy in Dogs with Golden Retriever Muscular Dystrophy," *Neuromuscular Disorders,* vol. 13, pp. 493-500, 2003.

[13] G. Yang, V. Lalande, L. Chen, N. Azzabou, T. Larcher, J. D. de Certaines, *et al.*, "MRI Texture Analysis of GRMD Dogs Using Orthogonal Moments: A Preliminary Study," *IRBM,* vol. 36, pp. 213-219, 2015.

[14] E. L. Finanger, B. Russman, S. C. Forbes, W. D. Rooney, G. A. Walter, and K. Vandenborne, "Use of Skeletal Muscle MRI in Diagnosis and Monitoring Disease Progression in Duchenne Muscular Dystrophy," *Physical Medicine & Rehabilitation Clinics of North America,* vol. 23, pp. 1-10, 2012.

[15] J. L. Thibaud, A. Monnet, D. Bertoldi, I. Barthelemy, S. Blot, and P. G. Carlier, "Characterization of dystrophic muscle in golden retriever muscular dystrophy dogs by nuclear magnetic resonance imaging," *Neuromuscul Disord,* vol. 17, pp. 575-584, 2007.

[16] H. Akima, D. Lott, C. Senesac, J. Deol, S. Germain, I. Arpan, *et al.*, "Relationships of thigh muscle contractile and non-contractile tissue with function, strength, and age in boys with Duchenne muscular dystrophy," *Neuromuscular Disorders,* vol. 22, pp. 16-25, 2012.

[17] P. Garrood, K. G. Hollingsworth, M. Eagle, B. S. Aribisala, D. Birchall, K. Bushby, *et al.*, "MR imaging in Duchenne muscular dystrophy: quantification of T1-weighted signal, contrast uptake, and the effects of exercise," *Journal of Magnetic Resonance Imaging,* vol. 30, pp. 1130-1138, Nov 2009.

[18] B. H. Wokke, J. C. van den Bergen, M. J. Versluis, E. H. Niks, J. Milles, A. G. Webb, *et al.*, "Quantitative MRI and strength measurements in the assessment of muscle quality in Duchenne muscular dystrophy," *Neuromuscular Disorders,* vol. 24, pp. 409-416, 2014.

[19] Z. Fan, J. Wang, M. Ahn, Y. Shiloh-Malawsky, N. Chahin, S. Elmore, *et al.*, "Characteristics of magnetic resonance imaging biomarkers in a natural history study of golden retriever muscular dystrophy," *Neuromuscul Disord,* vol. 24, pp. 178-191, 2014.

[20] R. Vohra, A. Accorsi, A. Kumar, G. Walter, and M. Girgenrath, "Magnetic Resonance Imaging Is Sensitive to Pathological Amelioration in a Model for Laminin-Deficient Congenital Muscular Dystrophy (MDC1A)," *PLOS ONE,* vol. 10, pp. 1-12, 2015.

[21] S. Ourselin, E. Bardinet, D. Dormont, G. Malandain, A. Roche, N. Ayache, *et al.*, "Fusion of Histological Sections and MR Images: Towards the Construction of an Atlas of the Human Basal Ganglia," in *Medical Image Computing and Computer-Assisted Intervention – MICCAI 2001: 4th International Conference Utrecht, The Netherlands, October 14–17, 2001 Proceedings*, W. J. Niessen and M. A. Viergever, Eds., ed Berlin, Heidelberg: Springer Berlin Heidelberg, 2001, pp. 743-751.

[22] A. Pitiot, E. Bardinet, P. M. Thompson, and G. Malandain, "Piecewise affine registration of biological images for volume reconstruction," *Medical Image Analysis,* vol. 10, pp. 465-483, 2006.

[23] M. A. Jacobs, J. P. Windham, H. Soltanian-Zadeh, D. J. Peck, and R. A. Knight, "Registration and warping of magnetic resonance images to histological sections," *Medical Physics,* vol. 26, pp. 1568-1578, 1999.

[24] T. Schormann and K. Zilles, "Three-dimensional linear and nonlinear transformations: an integration of light microscopical and MRI data," *Human brain mapping,* vol. 6, pp. 339-347, 1998.

[25] G. Li, S. Nikolova, and R. Bartha, "Registration of in vivo magnetic resonance T1-weighted brain images to triphenyltetrazolium chloride stained sections in small animals," *Journal of Neuroscience Methods,* vol. 156, pp. 368-375, 2006.

[26] J. V. Hajnal, D. L. G. Hill, and D. J. Hawkes, *Medical Image Registration*. USA: CRC Press, 2001.

[27] V. R. S. Mani and S. Arivazhagan, "Survey of Medical Image Registration," *Journal of Biomedical Engineering and Technology,* vol. 1, pp. 8-25, 2013.

[28] F. P. M. Oliveira and J. M. R. S. Tavares, "Medical Image Registration: a Review," *Computer Methods in Biomechanics and Biomedical Engineering,* vol. 17, pp. 73-93, 2012.

[29] L. Alic, J. C. Haeck, K. Bol, S. Klein, S. T. van Tiel, P. A. Wielepolski, *et al.*, "Facilitating Tumor Functional Assessment by Spatially Relating 3D Tumor Histology and In Vivo MRI: Image Registration Approach," *PLOS One,* vol. 6, pp. 1-10, 2011.

[30] H. Park, M. R. Piert, A. Khan, R. Shah, H. Hussain, J. Siddiqui, *et al.*, "Registration Methodology for Histological Sections and In Vivo Imaging of Human Prostate," *Academic Radiology,* vol. 15, pp. 1027-1039, 2008.

[31] G. Xiao, B. N. Bloch, J. Chappelow, E. M. Genega, N. M. Rofsky, R. E. Lenkinski, *et al.*, "Determining histology-MRI slice correspondences for defining MRI-based disease

signatures of prostate cancer," *Computerized Medical Imaging and Graphics,* vol. 35, pp. 568-578, 2011.

[32] M. Rusu, T. Golden, H. Wang, A. Gow, and A. Madabhushi, "Framework for 3D histologic reconstruction and fusion with in vivo MRI: Preliminary results of characterizing pulmonary inflammation in a mouse model," *Medical Physics,* vol. 42, pp. 4822-4832, 2015.

[33] Y. Mazaheri, L. Bokacheva, D.-J. Kroon, O. Akin, H. Hricak, D. Chamudot, *et al.*, "Semi-automatic Deformable Registration of Prostate Mr Images to Pathological Slices," *Journal of Magnetic Resonance Imaging,* vol. 32, pp. 1149-1157, 2010.

[34] H. M. Reynolds, S. Williams, A. Zhang, R. Chakravorty, D. Rawlinson, C. S. Ong, *et al.*, "Development of a registration framework to validate MRI with histology for prostate focal therapy," *Medical Physics,* vol. 42, pp. 7078-7089, 2015.

[35] T. S. Kim, M. Singh, W. Sungkara, C. Zarow, and H. Chui, "Automatic Registration of Postmortem Brain Slices to MRI Reference Volume," *IEEE Transactions on Nuclear Science,* vol. 47, pp. 1607-1613, 2000.

[36] S. Osechinskiy and F. Kruggel, "Slice-to-Volume Nonrigid Registration of Histological Sections to MR Images of the Human Brain," *Anatomy Research International,* vol. 2011, pp. 1-17, 2011.

[37] J. Chappelow, B. N. Bloch, N. Rofsky, E. Genega, R. Lenkinski, W. DeWolf, *et al.*, "Elastic Registration of Multimodal Prostate MRI and Histology via Multiattribute Combined Mutual Information," *Medical Physics,* vol. 38, pp. 2005-2018, 2011.

[38] N. Chicherova, K. Fundana, B. Müller, and P. C. Cattin, "Histology to μCT data matching using landmarks and a density biased RANSAC," presented at the International Conference on Medical Image Computing and Computer-Assisted Intervention, Boston, 2014.

[39] P. Markelj, D. Tomazevic, B. Likar, and F. Pernus, "A review of 3D/2D registration methods for image-guided interventions," *Medical Image Analysis,* vol. 16, pp. 642-661, 2012.

[40] E. Haber and J. Modersitzki, "Intensity Gradient Based Registration and Fusion of Multi-modal Images," Berlin, Heidelberg, 2006, pp. 726-733.

[41] L. H. Chen, H. Ho, R. Lazaro, C. H. Thng, J. Yuen, W. S. Ng, *et al.*, "Optimum slicing of radical prostatectomy specimens for correlation between histopathology and medical images," *International Journal of Computer Assisted Radiology and Surgery,* vol. 5, pp. 471-487, 2010.

[42] A. Eresen, P. Li, and J. X. Ji, "Correlating 2D histological slice with 3D MRI image volume using smart phone as an interactive tool for muscle study," in *2014 36th Annual International Conference of the IEEE Engineering in Medicine and Biology Society*, 2014, pp. 6418-6421.

[43] S. Klein, M. Staring, K. Murphy, M. A. Viergever, and J. P. Pluim, "elastix: a toolbox for intensity-based medical image registration," *IEEE Transactions of Medical Imaging,* vol. 29, pp. 196-205, 2010.

[44] Committee for the Update of the Guide for the Care and Use of Laboratory Animals, "Guide for the care and use of laboratory animals," ed. Washington, D.C.: National Academy Press, 2011.

[45] National Institutes of Health. (2015, 1 Sept). *Office of Laboratory Animal Welfare - Public Health Service Policy on Humane Care and Use of Laboratory Animals*.

[46] M. P. McDougall and S. M. Wright, "Volume Array Coil with Enforced Uniform Element Currents for Improved Excitation Homogeneity," ed: Google Patents, 2013.

[47] J. A. Kiernan, *Histological and Histochemical Methods*: Cold Spring Harbor Laboratory Press, 2008.

[48] C. K. Chow and T. Kaneko, "Automatic boundary detection of the left ventricle from cineangiograms," *Computers and Biomedical Research,* vol. 5, pp. 388-410, 1972 1972.

[49] C. Zhao, A. Carass, A. Jog, and J. L. Prince, "Effects of Spatial Resolution on Image Registration," in *Proc SPIE Int Soc Opt Eng,* 2016.

[50] C. Deroulers, D. Ameisen, M. Badoual, C. Gerin, A. Granier, and M. Lartaud, "Analyzing huge pathology images with open source software," *Diagnostic Pathology*, vol. 8, 2013.

[51] P. R. Bindhu, R. Krishnapillai, P. Thomas, and P. Jayanthi, "Facts in artifacts," *Journal of Oral and Maxillofacial Pathology*, vol. 17, pp. 397-401, 2013.

[52] N. Otsu, "A Threshold Selection Method from Gray-Level Histograms," *IEEE Transactions on Systems, Man, and Cybernetics*, vol. SMC-09, pp. 62-66, 1979.

[53] Michael Kass, A. Witkin, and D. Terzopoulos, "Snakes: Active contour models," *International Journal of Computer Vision*, vol. 1, pp. 321-331, 1988.

[54] T. M. Cover and J. A. Thomas, *Elements of Information Theory (Wiley Series in Telecommunications and Signal Processing)*: Wiley-Interscience, 2006.

[55] K. Pearson, "Note on Regression and Inheritance in the Case of Two Parents," *Proceedings of the Royal Society of London*, vol. 58, pp. 240-242, 1895.

CHAPTER III

TEXTURE AS IMAGING BIOMARKER FOR DISEASE SEVERITY IN GRMD

Duchenne muscular dystrophy is an X-linked genetic disorder caused by dystrophin protein deficiency [1]. The incidence of DMD is ~4000-6000 newborn males worldwide making it the most common form of muscular dystrophy [2]. Dystrophic muscles undergo repeated cycles of degeneration and are ultimately replaced by fat and connective tissue. Golden retriever muscular dystrophy is a genetically homologous DMD model that has similar phenotypic features [3]. Studies in GRMD dogs have helped to define efficacy and side effects of potential treatment options [4-8]. Various biomarkers have been developed to assess disease progression in both DMD and GRMD. Functional tests such as quantitative force measurements and the 6-minute-walk test give evidence of improvement but are prone to observer variability [9, 10]. Muscle biopsy traditionally provide ground truth information related to histopathological features but is invasive, generally limited to a single time point and specific region of the muscle [11]. This has led to efforts to identify quantitative, ideally noninvasive methods that could be tracked longitudinally in clinical trials.

Numerous studies have utilized magnetic resonance imaging (MRI) to monitor disease progression and treatment outcomes in pre-clinical [12-17] and clinical [18-21] studies. Quantitative MRI protocols such as T_1-map, T_2-map, water/fat images obtained from the Dixon sequence, and several diffusion tensor imaging parameters have also been used to assess muscle quality [22-27]. Studies have shown significant differences in muscle volume and cross-sectional area between healthy and diseased subjects in animal models [28-31], and in human subjects [32-36]. Imaging biomarkers in these and other studies have behaved differently across muscle types and stages of the disease [20, 28, 37]. During DMD disease progression, higher T_1 relaxation time was observed early in the disease course due to increased muscle free water associated with necrosis, but then decreased because of fibrosis and fat infiltration. In addition, several tissue types (i.e. necrotic, fatty and fibrotic) have longer T_2 relaxation time, making a differentiation between necrosis from fibrosis difficult. Clinical studies showed an increase in muscle fat fraction in DMD patients compared to healthy controls [25, 38, 39]. A positive correlation between age and fat fraction was also observed in DMD patients [25]. However, fat-infiltration was not observed at similar levels in GRMD subjects. On the other hand, significant differences of fractional anisotropy, apparent diffusion coefficient and mean diffusivity values were observed in clinical studies [40, 41]. As FA value was negatively correlated with muscle strength and fat-infiltration, a positive correlation with age was obtained. ADC values were positively correlated with muscle strength and fat infiltration but negatively correlated with age. Additionally, a significant increase in MD values occurred among DMD patients [40].

Muscle in DMD undergoes cycles of degeneration and regeneration, with associated inflammation, fat deposition, and fibrosis over time [42-44]. The wide range of lesions causes muscle heterogeneity in the MRI images [45, 46] potentially detectable by changes in muscle texture. Initial studies of heterogeneity focused on either T_1-weighted or T_2-weighted MRI images to differentiate between diseased and healthy subjects in clinical studies [47]. As an example, Zhang et. al. [47] use wavelet-based features and soft-margin support vector machines approach to assess the heterogeneity of T_1w and T_2w MRI images. They differentiate between healthy subjects and DMD patients with a classification accuracy of 92.9%. A number of studies have assessed texture features in GRMD dogs. In prior collaborations involving our group, Fan et. al. [15] and Wang et. al. [31] assessed first order statistics and texture in T_2w MRI to characterize

GRMD and healthy dogs at 3, 6 and 9 months of age. A different group assessed texture features (Zernike and Legendre moments) on selected regions of interest in T_2w MRI to differentiate between GRMD and healthy subjects at seven ages [48]. Maximum (100%) accuracy was reached using SVM approach at 5, 6, and 8 months among the seven age categories. Duda et. al. [49] assessed a total of 39 different texture features (first order statistics, normalized autocorrelation coefficient, gradient matrix, co-occurrence matrix, run-length matrix, gray level difference matrix, fractal dimension, entropy of laws' masks) in either raw MRI images (T_1w and T_2w) or gradient images to differentiate between GRMD and healthy subjects with a maximum accuracy of 95.8%.

In this study, we collected MRI images of *ex vivo* pectineus muscle samples with a clinical 3T Siemens Verio whole-body MRI scanner. Five groups of features of two qualitative and four quantitative MRI images were extracted. We used a classification approach to investigate the contribution of different qMRI sequences and also tested texture analysis as an imaging biomarker to differentiate between two age categories of GRMD muscles.

Materials and Methods

In this study, we hypothesized that heterogeneity in qMRI images can be used to grade the severity of DMD muscle lesions based on age, with the assumption that older dogs should have more severe lesions. To test our hypothesis, we developed a classification-based framework (Figure 3.1) that included three distinctive steps. First, MRI sequences were acquired, co-registered, and a set of qMRI images were generated. Second, a mask was generated to define a ROI, and heterogeneity features were extracted on the ROI. The final step involved building an SVM-based classifier.

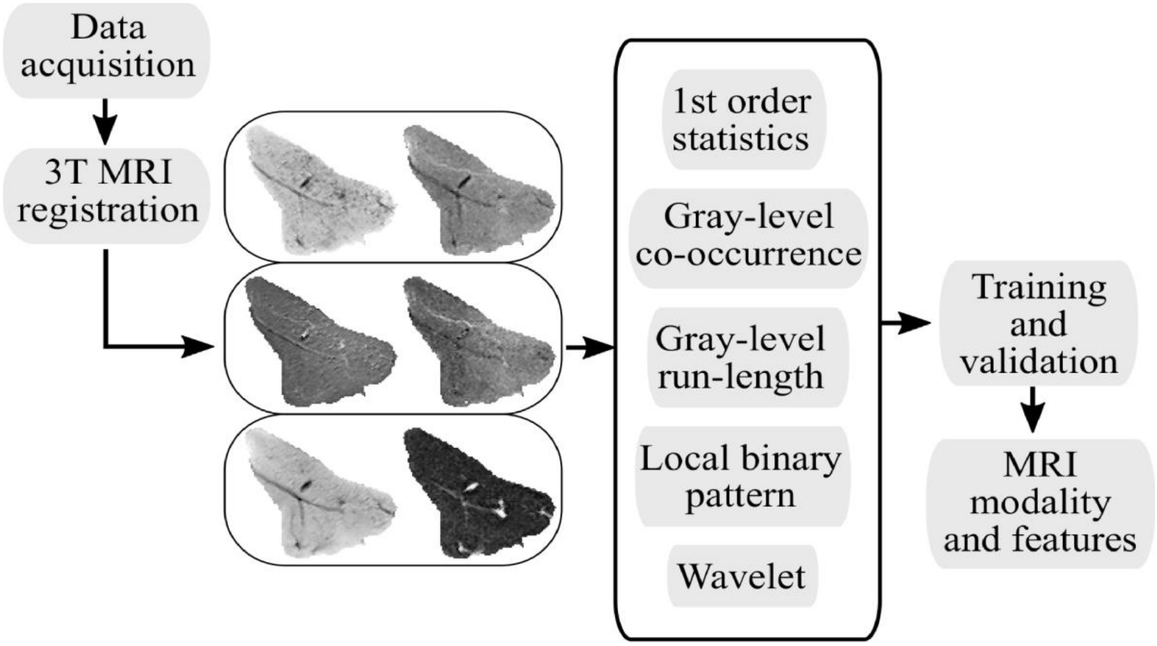

Figure 3.1. The framework represents the overall process of texture analysis to select MRI modality and textural features

Animals

The image data were collected from nine GRMD dogs from a colony at Texas A&M University under Institutional Animal Care and Use Committee (IACUC) protocol 2015-01110 under established standards [4, 50]. Pectineus muscle samples were removed from GRMD dogs during necropsy. The details were described in the second chapter of this dissertation [51].

MRI Image Acquisition

For MRI acquisitions, we used a clinical (3T Siemens Verio) whole-body MRI scanner and a small size loop coil (40 mm diameter). The MRI sequences acquired (36 slices with FOV of 50 mm × 50 mm), listed in Table 3.1, include T_1-weighted, T_2-weighted, two-point Dixon (D_2p), T_1-map, and T_2-map sequences.

Table 3.1. MRI acquisition parameters on clinical 3T MRI scanner

MRI Sequence	TR (ms)	TE (ms)	FA (°)	Averages	Resolution (µm)	Total time (min)
T_1w	16.7	5.51	4	9	195.31	25
T_2w	3500	60	-	1	195.31	4
T_1m	16.7	5.51	4, 21	9	195.31	51
T_2m	3500	15-90	-	1	195.31	15
Dixon	710	38	140	6	195.31	37

Image Processing and Registration

To reduce effects of bias-field artifacts, each 3D MRI image was corrected using the N4ITK algorithm [52]. The algorithm minimizes field inhomogeneity effects using a B-spline algorithm, with a multiresolution approach, to identify a smooth multiplicative field. Subsequently, all 3D MRI volumes were co-registered by applying an affine transformation using Elastix [53]. The middle MRI slices were used in further analysis. The T_1w image slice was used to generate a mask by morphological processing followed by thresholding. This initial mask was refined by a snake voxel-based approach to define the ROI for further processing [54]. T_1m images were calculated using the Despot1 method [55], T_2m images were estimated using a linear least squares regression algorithm, and D_2p water fraction (DWf) and fat fraction (DFf) images were estimated using one base and one frequency shifted image [56]. Figure 3.2 shows a representative set of two qualitative and four quantitative images from one muscle sample.

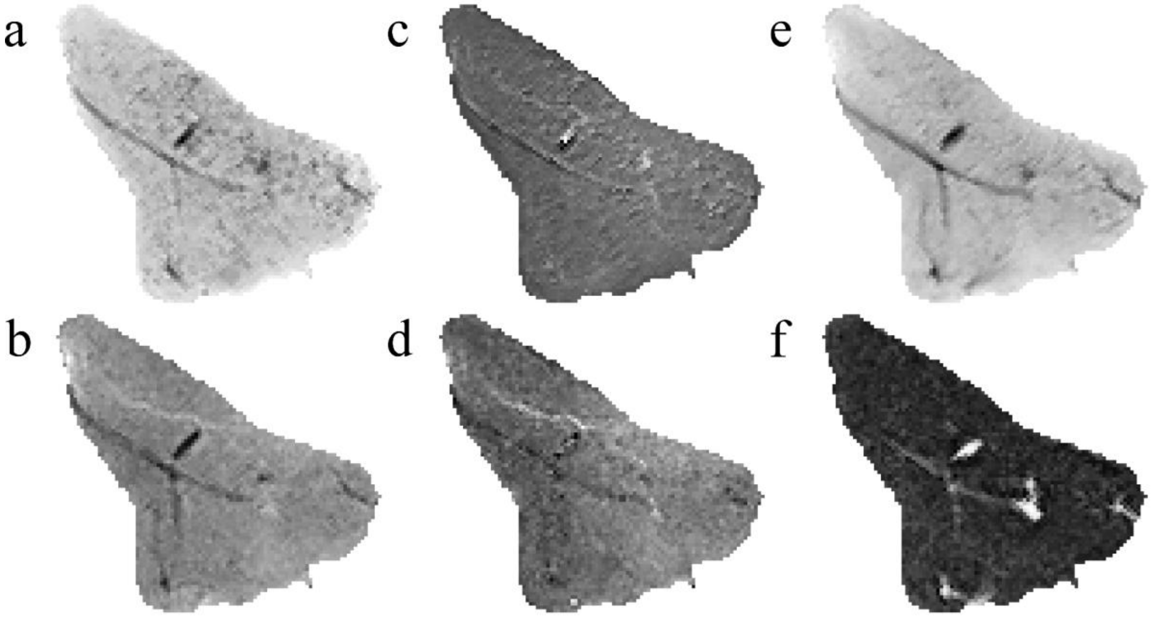

Figure 3.2. Qualitative and quantitative middle MRI slices of the sample from a 15 month-old GRMD dog acquired with the 3T clinical scanner: T_1w (a), T_2w (b), T_1m (c), T_2m (d), D_2p water fraction (e) and D_2p fat fraction (f) images.

Feature Extraction

In this study, we quantify the heterogeneity of the muscle tissue by extracting different texture descriptors from MRI images. For each MRI data (T_1w, T_2w, T_1m, T_2m, DWf, DFf), we computed 41 texture features listed in Table 3.2 and detailed in Table B1 (Appendix B). The calculated features are stored sequentially and used in the experiments by combining features up to 3 feature group.

Table 3.2. Features calculated from 3T MRI images

Feature combinations	Number of features (Pixelwise)
First order statistical features	6
Gray level co-occurrence matrix	6
Gray level run-length matrix features	7
Local binary pattern features	10
Wavelet transform based features	12

First Order Statistical Features

These methods characterize the muscle tissue by non-spatial descriptors, such as the gray-level frequency distributions. In this study, we used six FOS features: mean, standard deviation, third moment, entropy, skewness, and kurtosis for all samples. The features are calculated from normalized histograms of the grayscale MRI images.

Gray Level Co-occurrence Matrix

Co-occurrence matrix is one of the most popular texture analysis methods which describes the spatial relationship of pixels as the frequency of the occurring gray levels [57]. It's widely used for analysis of textures in images. GLCM measure can be calculated in different directions. For this study, we calculated GLCM in four main directions (0°, 45°, 135°, 180°), and average them to analyze the information for different directions together. We calculated six GLCM features: homogeneity, contrast, correlation, diagonal, entropy and energy using average GLCM data.

Gray Level Run-length Matrix

Run length encoding enables to define representative high-level statistical features as detecting the repetition of gray level intensities in the defined direction. GRLM calculates the length of intensity runs in four main directions (0°, 45°, 135°, 180°) [58]. In this study, we averaged the GRLM data calculated in four main directions and then calculated 11 GRLM features using the averaged GRLM matrix: short run emphasis, long run emphasis, gray-level nonuniformity, run length nonuniformity, run percentage, low gray-level run emphasis, high gray-level run emphasis, short-run low gray-level run emphasis, short-run high gray-level run emphasis, long run low gray-level run emphasis, and long run high gray-level run emphasis.

Local Binary Patterns

Local binary pattern method is one of the most popular texture operators due to its simplicity, efficiency, and robustness of monotonic illumination variations [59]. In LBP method, all pixels of the image are labeled as the sum of the weighted mask by comparing them with their neighbor pixels. Some LBP patterns i.e. edges, curves, flat areas, and spot occur more frequently than other patterns. Therefore, uniform patterns are commonly used to reduce the length of the descriptors defined by LBP method. In this study, we used the approach proposed by Ojala et. al. [60]. Utilizing LBP method, Ten LBP features (1-10) were calculated using eight neighborhood pixels for each MRI images.

Wavelet Transform

Wavelet transform represents signals by splitting into multiple frequency scales using different basis functions resulting in a signal with a half size of the original one described as high and low-frequency details. In this study, we used the Daubechies basis function with overlapping windows providing a reflection of all intensity variations between pixels. In two-dimensional wavelet, four quarter sized images were generated using a pair of linear filters. The mean, variance and power measures of the resulting four sub-images were computed to describe the textual description of the images.

Classification Framework

Data for classification were grouped according to subject ages: the samples between 3 and 12 months were considered the young group and remaining samples between 15 and 48 months were considered the adult group. A total of 41 features (Table 3.2) for each MRI dataset were used for the classification. Weighted MRI, T_1 and T_2 MRI maps and Dixon MRI maps were studied in three separate experiments to outline their potential for severity grading. Each experiment reports classification accuracy of textures as an imaging biomarker. In each experiment, we used a kernel-based SVM method [61] to assess the performance of increasing number of features. To assess the classification quality, a linear kernel in a leave-one-out cross-validation framework was used. The kernel parameters were optimized using a heuristic approach and the penalty factor was optimized empirically. The classification accuracy was averaged over nine experiments for each kernel parameter and penalty factor.

Even though accuracy is widely used to validate the classification performance, this metric is not always optimal [62]. Alternative metrics such as sensitivity and specificity have also been used to evaluate the classification model in diagnostic imaging [62, 63]. Therefore, accuracy, sensitivity, and specificity measures were all tracked during the training. In this research study, young subjects were selected as the negative class while adult samples were labeled as the positive class. The classification framework was used to identify disease effects related to age of the subjects. Sensitivity was used as a measure for correct detection rate of young subjects and specificity was the measure of correct detection of old subjects. To assess the performance of the classifier, we validated performance accuracy for all three metrics during the test phase. For each experiment separately, the number of features was increased incrementally from single MRI to a combination of MRI sequences in each sub-group. All experiments were completed using Matlab® (Version 9.1.0, MathWorks Inc., Natick, Massachusetts, USA).

Results

To assess the potential of weighted MRI images (quantified by texture features) as a biomarker of disease severity, we maximized accuracy, sensitivity, and specificity during the training processes. Table B1 (Appendix B) lists all textural features used in this study.

Experiment I: Weighted MRI as an Imaging Biomarker for Severity Grading

Table 3.3 lists the highest performance metrics for one, two, or three texture features separately. Table B2 (Appendix B) lists all textural features, with the highest validation accuracy shown in Table 3.3 for the incrementally added number of features.

With only one feature used, the average validation accuracy was 88.9% for a T_1w image and the combination of T_1w and T_2w images. Maximizing sensitivity during the training slightly decreased the validation accuracy, while maximizing accuracy or specificity provided the same validation results. The average validation accuracy of 88.9% was reached using a single feature from FOS (3^{th} moment) or WT (mean of approximation detail image, or variance of diagonal detail image) for a T_1w image and GRLM (low gray level run emphasis) or WT (mean of approximation detail image) for a combination of T_1w and T_2w images.

Table 3.3. The validation accuracy for clinical 3T MRI data for maximized accuracy, sensitivity and specificity illustrating increased accuracy by increasing number of features in all three MRI sets for weighted T_1 and T_2 images.

		Number of Features								
		1			2			3		
		Acc.	Se.	Sp.	Acc.	Se.	Sp.	Acc.	Se.	Sp.
MRI	T_1w	88.9	88.9	88.9	100	100	100	100	100	100
	T_2w	77.8	66.7	77.8	88.9	88.9	88.9	100	100	100
	Both	88.9	88.9	88.9	100	100	100	100	100	100

If two textural features were used, the average validation accuracy increased to 100% for T_1w image and the combination of T_1w and T_2w images. Maximizing any of the three metrics during training provided the same results. A validation accuracy of 100% was reached for several feature pairs for T_1w images (21 different feature combinations) and a combination of T_1w and

T_2w images (24 different feature combinations), see Table B2 (Appendix B). Figure 3.3 (left) presents the results of a classification model for incrementally adding a number of features and for all three weighted images separately. Figure 3.3 (right) presents a scatterplot for two features with maximum validation accuracy: i.e. WT (variance of detail image) and FOS (entropy) for T_1w image.

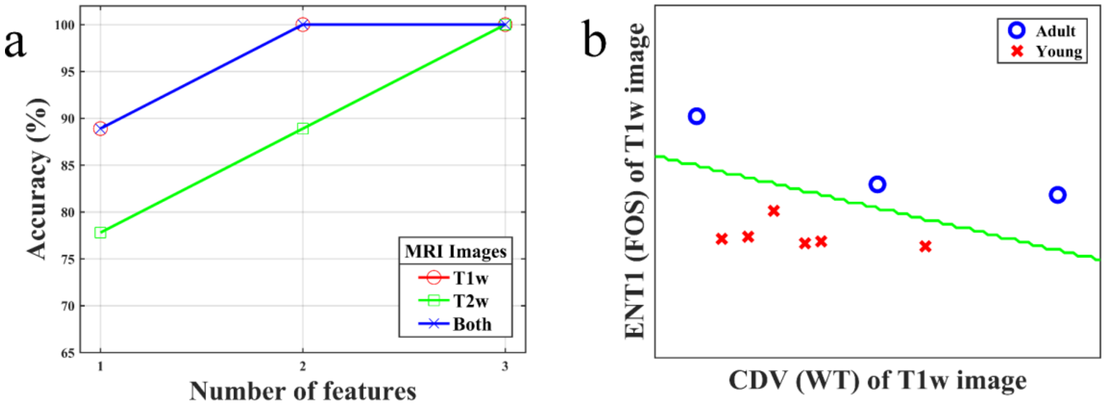

Figure 3.3. Classification results using features of only T_1w, only T_2w, or combined features of T_1w and T_2w illustrating increasing validation accuracy as a function of increasing number of features in all three MRI sets (a). The scatter plot of the most accurate texture features in T_1w images on clinical 3T data (b). The decision boundary of SVM is drawn in green.

For a triplet of features, the average validation accuracy was 100% for all three MRI options regardless of the metrics maximized during the training. Table B2 (Appendix B) summarizes all triplets with maximal validation accuracy for T_1w (470 different feature combinations), T_2w (7 different feature combinations), and a combination of T1w and T2w (348 different feature combinations).

Experiment II: T_1 and T_2 MRI Map as an Imaging Biomarker for Severity Grading

Table 3.4 lists the highest performance metrics for one, two, or three texture features separately. Table B3 (Appendix B) lists all textural features, with the highest validation accuracy shown in Table 3.4 for the incrementally added number of features.

With only one feature, the highest validation accuracy (100%) was obtained with the combination of T_1m and T_2m images using WT (power of diagonal detail image) regardless of the metrics used during training. For separate parametric maps, the validation accuracy was 88.9% for T_2m (5 different feature combinations) and 66.7% for T_1m, (20 different feature combinations).

Table 3.4. The validation accuracy for clinical 3T MRI data for maximized accuracy, sensitivity and specificity illustrating increased accuracy by increasing number of features in all three MRI sets for parametric T_1m and T_2m images.

		Number of Features								
		1			2			3		
		Acc.	Se.	Sp.	Acc.	Se.	Sp.	Acc.	Se.	Sp.
MRI	T_1m	66.7	66.7	66.7	88.9	88.9	88.9	100	100	100
	T_2m	88.9	88.9	77.8	100	100	100	100	100	100
	Both	100	100	100	100	100	100	100	100	100

With two textural features used, the validation accuracy increased to 100% for T_2m and combination of T_1m and T_2m images. The highest validation accuracy for T_2m images was obtained by a combination of LBP features (2&10 or 4&6). There are several combinations of texture features providing maximum accuracy for a combination of T_1w and T_2w images, i.e. GRLM and WT, LBP and two different features form WT. Figure 3.4 (left) shows the results of the classification model of incrementally adding the number of features and for all three map images separately. Figure 3.4 (right) shows a scatterplot for texture in T_1m and T_2m quantified by WT (power of diagonal detail image).

For a triplet of texture features, regardless of the performance metrics used during classification, resulted in 100% validation accuracy for all three MRI image inputs. Table B3 (Appendix B) summarizes all triplets with maximal validation accuracy for T_1m (4 different feature combinations), T_2m (21 different feature combinations), and a combination of T_1m and T_2m (43 different feature combinations).

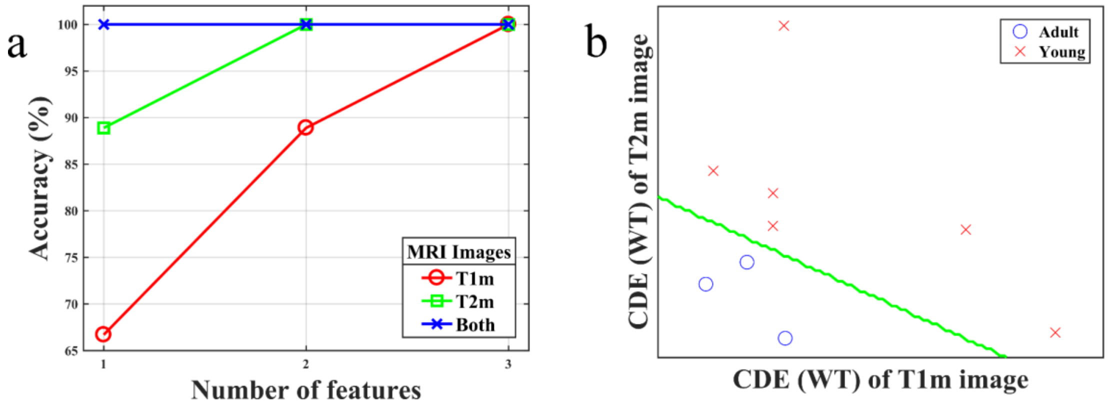

Figure 3.4. Classification results using features of only T_1m, only T_2m, or combined features of T_1m and T_2m illustrating increasing validation accuracy as a function of increasing number of features in all three MRI sets (a). The scatter plot of the most accurate texture features in T_1m and T_2m images on clinical 3T data (b). The decision boundary of SVM is drawn in green.

Experiment III: Dixon MRI Maps as an Imaging Biomarker for Severity Grading

Table 3.5 lists the highest performance metrics for one, two, or three texture features separately. Table B4 (Appendix B) lists all textural features, with the highest validation accuracy shown in Table 3.5 for the incrementally added number of features.

Using one texture feature, WT (mean of horizontal detail image), extracted from DWf maps provided a validation accuracy of 77.8%. There were 23 texture features, extracted from DFf maps, with validation accuracy of 66.7% and slightly increased to 77.8% with LBP (5) feature as specificity measure used during the training process. Using a combination of Dixon maps increased the accuracy to 100% when assessed by GRLM (short run emphasis).

Table 3.5. The validation accuracy for clinical 3T MRI data for maximized accuracy, sensitivity and specificity illustrating increased accuracy by increasing number of features in all three MRI sets for Dixon (water and fat) images.

		Number of Features								
		1			2			3		
		Acc.	Se.	Sp.	Acc.	Se.	Sp.	Acc.	Se.	Sp.
MRI	DWf	77.8	77.8	77.8	88.9	88.9	88.9	100	100	100
	DFf	66.7	66.7	77.8	100	100	100	100	100	100
	Both	100	100	100	100	100	100	100	100	100

Two texture features combined improved the validation accuracy to 88.9% for DWf map (5 different feature combinations). The validation accuracy for texture features extracted from DFf was 100% for 11 different feature combinations, and for a combination of both Dixon maps (23 different feature combinations). Figure 3.5 (left) shows the results of the classification model of incrementally adding a number of features and for all three Dixon images separately. Figure 3.5 (right) presents a scatterplot for two features of a DFf image with maximum validation accuracy: i.e. WT (variance and power of vertical detail images).

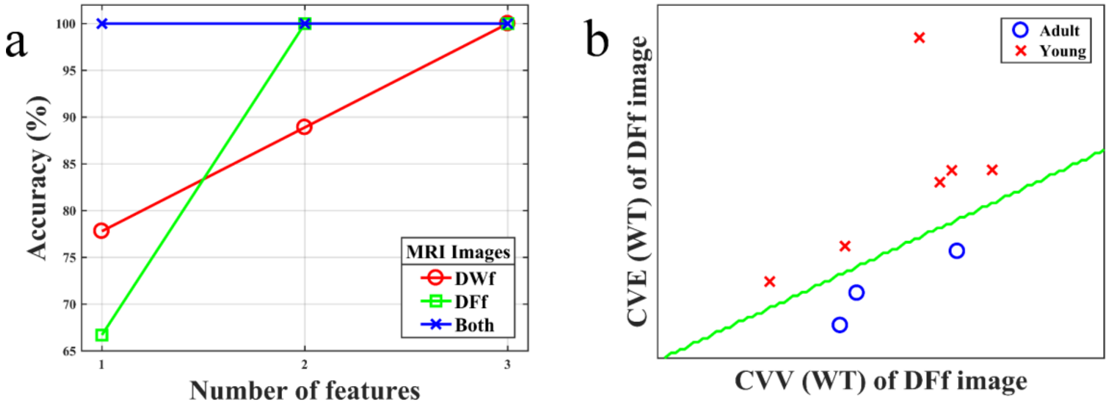

Figure 3.5. Classification results using features of only DWf, only DFf, or combined features of DWf and DFf illustrating increasing validation accuracy as a function of increasing number of features in all three MRI sets (a). The scatter plot of the most accurate texture features in DFf images on clinical 3T data (b). The decision boundary of SVM drawn in green.

For a triplet of features with D_2p images, 100% validation accuracy was obtained regardless of performance metrics or map. Among the feature groups, GRLM features had the most common features with maximized accuracy.

Discussions and Conclusions

Evaluation of subtle changes in skeletal muscle using non-invasive imaging techniques such as MRI has great potential for assessment of clinical outcomes and disease progression in GRMD. In this study, we assessed a texture analysis approach to identify imaging biomarkers that tracked with disease severity and optimum MRI modalities to reduce imaging time and computation cost. A single MRI image or combination of several MRI images quantified using five group of features (first order statistics, gray level co-occurrence matrix, gray level run-length matrix features, local binary pattern features, and wavelet transform based features) was used to assess complex MRI characteristics. We used a soft margin based SVM approach to classify the MRI data in a leave-one-out approach.

The MRI images were analyzed in three experimental setups: weighted image (T_1w and T_2w), parametric maps (T_1m and T_2m), and Dixon maps (water and fat). Our results showed that T_1w images provided better discrimination than T_2w images and that calculating two texture features on T_1w MRI images provided excellent results (100% accuracy). In contrast, if only one texture feature from either T_1w or T_2w was analyzed, the highest accuracy was 88.9% and 77.8%, respectively. Combining T_1w and T_2w image features did not significantly influence the results. For MRI parametric maps, use of two texture features (LBP) to quantify heterogeneity in T_2m produced 100% accuracy. In contrast to weighted MRI images, merging parametric maps (T_1m and T_2m) improved the classification accuracy (100%). Combining Dixon parametric maps (water and fat fraction) provided 100% accuracy when quantified using texture descriptor extracted from the gray-level run-length matrix. Similarly, a combination of the gray-level run-length matrix, local binary patterns, and wavelet-based descriptors or gray-level run-length matrix features in combination with first order statistics, local binary patterns or wavelet-based descriptors, or gray-level co-occurrence matrix in combination with wavelet-based descriptors was 100% accurate for fat-fraction map. In all cases, using three texture features was 100% accurate in grading GRMD severity.

For sake of the analysis, we divided the muscles into two groups based on age. The assumption was that older dogs would have more severe lesions. Given that disease progression varies among GRMD dogs, there was potential for overlap between the two age groups. However, the two groups generally had distinctive MRI features that allowed us to test our approach. The study was also limited by the relatively low number of samples, which is common with large animal preclinical studies. As a result, there was considerable variation among the ages of the two disease groups, which undoubtedly reduced the robustness and sensitivity of the approach.

In summary, this study assessed a number of texture descriptors as potential non-invasive MRI biomarkers for grading disease severity reflected in aging effects in GRMD dogs. The classification results showed high validation accuracy regardless of the type of metrics used in training. Furthermore, combining features of multiple MRI images improved classification accuracy. We were unable to reach 100% accuracy when only one MRI sequence was used in combination with a single texture feature. However, use of one texture feature in combination with two MRI parametric maps was 100% accurate for longitudinal and transverse parametric maps and for Dixon fat and water fractions. Analysis of two texture features in combination with one MRI sequence was 100% accurate with single T_1-weighted images, T_2 parametric map and Dixon fat fraction. Considering the scan-time and complexity of calculating texture features, T_2m images provided better accuracy with lower acquisition time than other MRI sequences. The accuracy of T_1w and T_1m images was same when nine averages were used due to the reduced signal to noise ratio. On the other hand, Dixon fat fraction and combination of Dixon images provided similar validation accuracies when six averages were used to improve the signal to noise ratio. However, the increase in acquisition time could potentially lead to movement artifacts during clinical acquisition. Accordingly, analysis of T_2m images has greater potential as a non-invasive biomarker for assessment of severity of GRMD disease.

References

[1] J. Y. Cheung, J. V. Bonventre, C. D. Malis, and A. Leaf, "Calcium and ischemic injury," *The New England Journal of Medicine,* vol. 314, pp. 1670-1676, 1986.

[2] J. R. Mendell, C. Shilling, N. D. Leslie, K. M. Flanigan, R. al-Dahhak, J. Gastier-Foster, *et al.*, "Evidence-based path to newborn screening for Duchenne muscular dystrophy," *Annals of Neurology,* vol. 71, pp. 304-313, 2012.

[3] C. Brinkmeyer-Langford and J. N. Kornegay, "Comparative genomics of X-linked muscular dystrophies: the golden retriever model," *Curr Genomics,* vol. 14, 2013.

[4] "Duchenne muscular dystrophy," in *Medline Plus Encylopedia,* ed.

[5] J. M. Liu, C. S. Okamura, D. J. Bogan, J. R. Bogan, M. K. Childers, and J. N. Kornegay, "Effects of prednisone in canine muscular dystrophy," *Muscle Nerve,* vol. 30, pp. 767-773, 2004.

[6] J. N. Kornegay, C. F. Spurney, P. P. Nghiem, C. L. Brinkmeyer-Langford, E. P. Hoffman, and K. Nagaraju, "Pharmacologic management of Duchenne muscular dystrophy: target identification and preclinical trials," *ILAR Journal*, vol. 55, pp. 119-149, 2014.

[7] A. Vulin, I. Barthélémy, A. Goyenvalle, J.-L. Thibaud, C. Beley, G. Griffith, *et al.*, "Muscle function recovery in golden retriever muscular dystrophy after AAV1-U7 exon skipping," *Mol Ther,* vol. 20, pp. 2120-2133, 2012.

[8] I. Barthelemy, A. Uriarte, C. Drougard, Y. Unterfinger, J.-L. Thibaud, and S. Blot, "Effects of an immunosuppressive treatment in the GRMD dog model of Duchenne muscular dystrophy," *PLoS One,* vol. 7, pp. 1-12, 2012.

[9] A. Lerario, S. Bonfiglio, M. Sormani, A. Tettamanti, S. Marktel, S. Napolitano, *et al.*, "Quantitative muscle strength assessment in duchenne muscular dystrophy: longitudinal study and correlation with functional measures," *BMC Neurol,* vol. 12, p. 91,2012.

[10] J. L. Thibaud, A. Monnet, D. Bertoldi, I. Barthe´le´my, S. Blot, and P. G. Carlier, "Characterization of Dystrophic Muscle in Golden Retriever Muscular Dystrophy Dogs by Nuclear Magnetic Resonance Imaging," *Neuromuscular Disorders,* vol. 17, p. 10, 2007.

[11] G. Yang, V. Lalande, L. Chen, N. Azzabou, T. Larcher, J. D. de Certaines, *et al.*, "MRI texture analysis of GRMD dogs using orthogonal moments: A preliminary study," *Irbm,* vol. 36, pp. 213-219, 2015.

[12] A. B. Martins-Bach, J. Malheiros, B. Matot, P. C. M. Martins, C. F. Almeida, W. Caldeira, *et al.*, "Quantitative T2 Combined with Texture Analysis of Nuclear Magnetic Resonance Images Identify Different Degrees of Muscle Involvement in Three Mouse Models of

Muscle Dystrophy: mdx, Largemyd and mdx/Largemyd," *PLOS ONE,* vol. 10, pp. 1-16, 2015.

[13] R. S. Vohra, S. Mathur, N. D. Bryant, S. C. Forbes, K. Vandenborne, and G. A. Walter, "Age-related T2 changes in hindlimb muscles of mdx mice," *Muscle & Nerve,* vol. 53, pp. 84-90, 2016.

[14] E. C. Qin, L. Jugé, S. A. Lambert, V. Paradis, R. Sinkus, and L. E. Bilston, "In Vivo Anisotropic Mechanical Properties of Dystrophic Skeletal Muscles Measured by Anisotropic MR Elastographic Imaging: The mdx Mouse Model of Muscular Dystrophy," *Radiology,* vol. 273, pp. 726-735, 2014.

[15] Z. Fan, J. Wang, M. Ahn, Y. Shiloh-Malawsky, N. Chahin, S. Elmore*, et al.*, "Characteristics of magnetic resonance imaging biomarkers in a natural history study of golden retriever muscular dystrophy," *Neuromuscular Disorders,* vol. 24, pp. 178-191, 2014.

[16] J. Park, J. Wicki, S. E. Knoblaugh, J. S. Chamberlain, and D. Lee, "Multi-Parametric MRI at 14T for Muscular Dystrophy Mice Treated with AAV Vector-Mediated Gene Therapy," *PLOS ONE,* vol. 10, pp. 1-24, 2015.

[17] T. Yokota, Q.-l. Lu, T. Partridge, M. Kobayashi, A. Nakamura, S. Takeda*, et al.*, "Efficacy of systemic morpholino exon-skipping in duchenne dystrophy dogs," *Annals of Neurology,* vol. 65, pp. 667-676, 2009.

[18] B. H. Wokke, J. C. Van Den Bergen, M. T. Hooijmans, J. J. Verschuuren, E. H. Niks, and H. E. Kan, "T2 relaxation times are increased in Skeletal muscle of DMD but not BMD patients," *Muscle & Nerve,* vol. 53, pp. 38-43, 2016.

[19] M. T. Hooijmans, N. Doorenweerd, C. Baligand, J. J. G. M. Verschuuren, I. Ronen, E. H. Niks*, et al.*, "Spatially localized phosphorous metabolism of skeletal muscle in Duchenne muscular dystrophy patients: 24–month follow-up," *PLOS ONE*, vol. 12, pp. 1-15, 2017.

[20] R. J. Willcocks, I. A. Arpan, S. C. Forbes, D. J. Lott, C. R. Senesac, E. Senesac*, et al.*, "Longitudinal measurements of MRI-T2 in boys with Duchenne muscular dystrophy: Effects of age and disease progression," *Neuromuscular Disorders,* vol. 24, pp. 393-401, 2014.

[21] I. Arpan, R. J. Willcocks, S. C. Forbes, R. S. Finkel, D. J. Lott, W. D. Rooney, *et al.*, "Examination of effects of corticosteroids on skeletal muscles of boys with DMD using MRI and MRS," *Neurology,* vol. 83, pp. 974-980, 2014.

[22] T. A. L. Wren, S. Bluml, L. Tseng-Ong, and V. Gilsanz, "Three-Point Technique of Fat Quantification of Muscle Tissue as a Marker of Disease Progression in Duchenne Muscular Dystrophy: Preliminary Study," *American Journal of Roentgenology,* vol. 190, pp. W8-W12, 2008.

[23] H. K. Kim, T. Laor, P. S. Horn, J. M. Racadio, B. Wong, and B. J. Dardzinski, "T2 Mapping in Duchenne Muscular Dystrophy: Distribution of Disease Activity and Correlation with Clinical Assessments," *Radiology,* vol. 255, pp. 899-908, 2010.

[24] I. Arpan, S. C. Forbes, D. J. Lott, C. R. Senesac, M. J. Daniels, W. T. Triplett, *et al.*, "T2 mapping provides multiple approaches for the characterization of muscle involvement in neuromuscular diseases: a cross-sectional study of lower leg muscles in 5–15-year-old boys with Duchenne muscular dystrophy," *NMR in Biomedicine,* vol. 26, pp. 320-328, 2013.

[25] A. Fischmann, P. Hafner, M. Gloor, M. Schmid, A. Klein, U. Pohlman, *et al.*, "Quantitative MRI and loss of free ambulation in Duchenne muscular dystrophy," *Journal of Neurology,* vol. 260, pp. 969-974, 2013.

[26] S. C. Forbes, G. A. Walter, W. D. Rooney, D.-J. Wang, S. DeVos, J. Pollaro, *et al.*, "Skeletal Muscles of Ambulant Children with Duchenne Muscular Dystrophy: Validation of Multicenter Study of Evaluation with MR Imaging and MR Spectroscopy," *Radiology,* vol. 269, pp. 198-207, 2013.

[27] K. G. Hollingsworth, P. Garrood, M. Eagle, K. Bushby, and V. Straub, "Magnetic resonance imaging in duchenne muscular dystrophy: Longitudinal assessment of natural history over 18 months," *Muscle & Nerve,* vol. 48, pp. 586-588, 2013.

[28] R. Vohra, A. Accorsi, A. Kumar, G. Walter, and M. Girgenrath, "Magnetic Resonance Imaging Is Sensitive to Pathological Amelioration in a Model for Laminin-Deficient Congenital Muscular Dystrophy (MDC1A)," *PLOS ONE,* vol. 10, pp. 1-12, 2015.

[29] L. T. Bish, M. M. Sleeper, S. C. Forbes, K. J. Morine, C. Reynolds, and G. E. Singletary, "Long-term systemic myostatin inhibition via liver-targeted gene transfer in golden retriever muscular dystrophy," *Hum Gene Ther*, vol. 22, 2011.

[30] C. R. Heier, A. D. Guerron, A. Korotcov, S. Lin, H. Gordish-Dressman, S. Fricke, *et al.*, "Non-Invasive MRI and Spectroscopy of mdx Mice Reveal Temporal Changes in Dystrophic Muscle Imaging and in Energy Deficits," *PLOS ONE*, vol. 9, pp. 1-12, 2014.

[31] J. Wang, Z. Fan, K. Vandenborne, G. Walter, Y. Shiloh-Malawsky, H. An, *et al.*, "A computerized MRI biomarker quantification scheme for a canine model of Duchenne muscular dystrophy," *International Journal of Computer Assisted Radiology and Surgery*, vol. 8, pp. 763-774, 2013.

[32] R. S. Vohra, D. Lott, S. Mathur, C. Senesac, J. Deol, S. Germain, *et al.*, "Magnetic Resonance Assessment of Hypertrophic and Pseudo-Hypertrophic Changes in Lower Leg Muscles of Boys with Duchenne Muscular Dystrophy and Their Relationship to Functional Measurements," *PLOS ONE*, vol. 10, pp. 1-12, 2015.

[33] B. H. Wokke, J. C. van den Bergen, M. J. Versluis, E. H. Niks, J. Milles, A. G. Webb, *et al.*, "Quantitative MRI and strength measurements in the assessment of muscle quality in Duchenne muscular dystrophy," *Neuromuscular Disorders*, vol. 24, pp. 409-416, 2014.

[34] S. Mathur, D. J. Lott, C. Senesac, S. A. Germain, R. S. Vohra, H. L. Sweeney, *et al.*, "Age-Related Differences in Lower-Limb Muscle Cross-Sectional Area and Torque Production in Boys With Duchenne Muscular Dystrophy," *Archives of Physical Medicine and Rehabilitation*, vol. 91, pp. 1051-1058, 2010.

[35] P. Richards, W. R. Saywell, and P. Heywood, "Pseudohypertrophy of the temporalis muscle in Xp21 muscular dystrophy," *Developmental Medicine & Child Neurology*, vol. 42, pp. 786-787, 2000.

[36] H. Akima, D. Lott, C. Senesac, J. Deol, S. Germain, I. Arpan, *et al.*, "Relationships of thigh muscle contractile and non-contractile tissue with function, strength, and age in boys with Duchenne muscular dystrophy," *Neuromuscular Disorders*, vol. 22, pp. 16-25, 2012.

[37] T. C. Roberts, K. E. M. Blomberg, G. McClorey, S. E. L. Andaloussi, C. Godfrey, C. Betts, *et al.*, "Expression Analysis in Multiple Muscle Groups and Serum Reveals Complexity in

the MicroRNA Transcriptome of the mdx Mouse with Implications for Therapy," *Molecular Therapy. Nucleic Acids,* vol. 1, pp. 1-11, 2012.

[38] V. Ricotti, M. R. B. Evans, C. D. J. Sinclair, J. W. Butler, D. A. Ridout, J.-Y. Hogrel, *et al.*, "Upper Limb Evaluation in Duchenne Muscular Dystrophy: Fat-Water Quantification by MRI, Muscle Force and Function Define Endpoints for Clinical Trials," *PLOS ONE,* vol. 11, pp. 1-15, 2016.

[39] J. Burakiewicz, C. D. J. Sinclair, D. Fischer, G. A. Walter, H. E. Kan, and K. G. Hollingsworth, "Quantifying fat replacement of muscle by quantitative MRI in muscular dystrophy," *Journal of Neurology,* vol. 264, pp. 2053-2067, 2017.

[40] M. T. Hooijmans, B. M. Damon, M. Froeling, M. J. Versluis, J. Burakiewicz, J. J. G. M. Verschuuren, *et al.*, "Evaluation of skeletal muscle DTI in patients with duchenne muscular dystrophy," *NMR in Biomedicine,* vol. 28, pp. 1589-1597, 2015.

[41] S. Ponrartana, L. Ramos-Platt, T. A. L. Wren, H. H. Hu, T. G. Perkins, J. M. Chia, *et al.*, "Effectiveness of Diffusion Tensor Imaging in Assessing Disease Severity in Duchenne Muscular Dystrophy: Preliminary Study," *Pediatric Radiology,* vol. 45, pp. 582-589, 2014.

[42] J. L. Thibaud, A. Monnet, D. Bertoldi, I. Barthelemy, S. Blot, and P. G. Carlier, "Characterization of dystrophic muscle in golden retriever muscular dystrophy dogs by nuclear magnetic resonance imaging," *Neuromuscular Disorders,* vol. 17, pp. 575-584, 2007.

[43] R. J. Willcocks, W. D. Rooney, W. T. Triplett, S. C. Forbes, D. J. Lott, C. R. Senesac, *et al.*, "Multicenter prospective longitudinal study of magnetic resonance biomarkers in a large duchenne muscular dystrophy cohort," *Annals of Neurology,* vol. 79, pp. 535-547, 2016.

[44] J. N. Kornegay, "The golden retriever model of Duchenne muscular dystrophy," *Skeletal Muscle,* vol. 7, pp. 1-21, 2017.

[45] J. L. Thibaud, N. Azzabou, I. Barthelemy, S. Fleury, L. Cabrol, S. Blot, *et al.*, "Comprehensive Longitudinal Characterization of Canine Muscular Dystrophy by Serial NMR Imaging of GRMD Dogs," *Neuromuscular Disorders,* vol. 22, pp. S85-S99, 2012.

[46] M. Kinali, V. Arechavala-Gomeza, S. Cirak, A. Glover, M. Guglieri, L. Feng, *et al.*, "Muscle histology vs MRI in Duchenne muscular dystrophy," *Neurology,* vol. 76, pp. 346-353, 2011.

[47] M.-H. Zhang, J.-S. Ma, Y. Shen, and Y. Chen, "Optimal classification for the diagnosis of duchenne muscular dystrophy images using support vector machines," *International Journal of Computer Assisted Radiology and Surgery,* vol. 11, pp. 1755-1763, 2016.

[48] G. Yang, V. Lalande, L. Chen, N. Azzabou, T. Larcher, J. D. de Certaines, *et al.*, "MRI Texture Analysis of GRMD Dogs Using Orthogonal Moments: A Preliminary Study," *IRBM,* vol. 36, pp. 213-219, 2015.

[49] D. Duda, M. Kretowski, N. Azzabou, and J. D. de Certaines, "MRI Texture Analysis for Differentiation Between Healthy and Golden Retriever Muscular Dystrophy Dogs at Different Phases of Disease Evolution," in *Computer Information Systems and Industrial Management*, 2015, pp. 255-266.

[50] Committee for the Update of the Guide for the Care and Use of Laboratory Animals, "Guide for the care and use of laboratory animals," ed. Washington, D.C.: National Academy Press, 2011.

[51] A. Eresen, S. McConnell, S. M. Birch, J. F. Griffin IV, J. N. Kornegay, and J. X. Ji, "Tissue classification in a canine model of Duchenne Muscular Dystrophy using quantitative MRI parameters," in *39th Annual International Conference of the IEEE Engineering in Medicine and Biology Society (EMBC),* Seogwipo, South Korea, 2017.

[52] N. J. Tustison, B. B. Avants, P. A. Cook, Y. Zheng, A. Egan, P. A. Yushkevich, *et al.*, "N4ITK: Improved N3 Bias Correction," *IEEE Transactions on Medical Imaging,* vol. 29, pp. 1310-1320, 2010.

[53] S. Klein, M. Staring, K. Murphy, M. A. Viergever, and J. P. Pluim, "elastix: a toolbox for intensity-based medical image registration," *IEEE Trans Med Imaging,* vol. 29, pp. 196-205, 2010.

[54] Michael Kass, A. Witkin, and D. Terzopoulos, "Snakes: Active contour models," *International Journal of Computer Vision,* vol. 1, pp. 321-331, 1988.

[55] S. C. L. Deoni, B. K. Rutt, and T. M. Peters, "Rapid Combined T1and T2 Mapping Using Gradient Recalled Acquisition in the Steady State," *Magnetic Resonance in Medicine,* vol. 49, pp. 515-526, 2003.

[56] G. H. Glover and E. Schneider, "Three-Point Dixon Technique for True Water/Fat Decomposition with B_0 Inhomogeneity Correction," *Magnetic Resonance Imaging,* vol. 18, pp. 371-383, 1991.

[57] R. M. Haralick, K. Shanmugam, and I. H. Dinstein, "Textural features for image classification," *IEEE Transactions on Systems, Man, and Cybernetics,* vol. SMC-3, pp. 610-621, 1973.

[58] M. M. Galloway, "Texture analysis using gray level run lengths," *Computer Graphics and Image Processing,* vol. 4, pp. 172-179, 1975.

[59] T. Ojala, M. Pietikäinen, and D. Harwood, "A comparative study of texture measures with classification based on featured distributions," *Pattern Recognition,* vol. 29, pp. 51-59, 1996.

[60] T. Ojala, M. Pietikainen, and T. Maenpaa, "Multiresolution gray-scale and rotation invariant texture classification with local binary patterns," *IEEE Transactions on Pattern Analysis and Machine Intelligence,* vol. 24, pp. 971-987, 2002.

[61] C. J. C. Burges, "A Tutorial on Support Vector Machines for Pattern Recognition," *Data Mining and Knowledge Discovery,* vol. 2, pp. 121-167, 1998.

[62] W. Zhu, N. F. Zeng, and N. Wang, "Sensitivity, Specificity, Accuracy, Associated Confidence Interval and ROC Analysis with Practical SAS Implementations," in *NESUG Proceedings: Health Care and Life Sciences*, Baltimore, 2010.

[63] J. Maroco, D. Silva, A. Rodrigues, M. Guerreiro, I. Santana, and A. de Mendonça, "Data mining methods in the prediction of Dementia: A real-data comparison of the accuracy, sensitivity and specificity of linear discriminant analysis, logistic regression, neural networks, support vector machines, classification trees and random forests," *BMC Research Notes,* vol. 4, p. 299, 2011.

CHAPTER IV

MUSCLE PERCENTAGE INDEX AS AN IMAGING BIOMARKER FOR QUANTIFICATION OF MUSCLE DEGENERATION IN GRMD: MACHINE LEARNING APPROACH

There is a great demand for accurate outcome measures across all disease stages to improve the understanding of natural history and to facilitate the inclusion of a large range of participants in clinical trials. Current outcome measures are suboptimal: e.g., functional and muscle strength assessments are susceptible to rater variability [1, 2]. A vast variety of studies have utilized histological sections (paraffin and freshly-frozen) with different histochemical enzymes as an accurate ground-truth information (the gold standard) for assessment of the therapeutic response in DMD [3]. In DMD, inflammatory processes and subsequent fat replacement of muscle tissue is identified as a useful endpoint in clinical therapeutic trials, although progression in different muscle groups is reported to be uneven [4]. These processes in dystrophic muscles are quantifiable in histology images, though often assessed qualitatively [5]. The quantitative parameters for specific histological features (e.g. myofiber necrosis, fibrosis and fatty connective tissue, muscle) usually include the number of fibers or percentage of a feature of interest in the cross-section area [6]. The morphometric assessment of these parameters evolved from early manual methods [7], trough digitized planimetry [8, 9], to semi-automated [10] and completely automated methods [11]. However, these histopathological approaches have considerable drawbacks: i.e., highly invasive, a limited amount of coverage by specimen size, and unreliable representation of the overall disease state or therapeutic progress due to the variability of muscle involvement during the disease progression [12].

A variety of MRI protocols have evolved as a non-invasive alternative to provide useful information on natural disease progression and assessment of treatment response in pre-clinical [5, 13-17] and clinical [18-21] DMD studies. Quantitative mapping of MRI data has emerged as an attempt to quantify this process and use it as a non-invasive imaging biomarker. This includes the following parametric maps: T_1-relaxation time and T_2-relaxation time, water and fat maps using Dixon approach, and diffusion-weighted imaging [18, 22-27]. The data can be acquired using sequences with or without fat suppression. To assess disease progression and response to treatment, a vast majority of publications reports first order statistics based on (manually segmented) muscle volume in a number of parametric maps. Imaging biomarkers, i.e. total volume, cross-sectional area and muscle volume index, are observed as significantly different between healthy and diseased subjects in animal models [25, 28-30] and human studies [25, 31-35]. However, the same biomarkers are inconsistent between different muscle groups across the disease states [20, 25, 36]. Moreover, the current methods are often not automated and therefore are irreproducible and non-robust.

Even though it is long known that different processes (i.e., inflammation, degeneration, regeneration) are involved during the disease progression in DMD [1, 37, 38], this information has not been integrated to produce a single non-invasive imaging biomarker. Therefore, as a first attempt to identify an automated and a robust MRI biomarker, we develop and validate a classification-based segmentation framework reporting the muscle percentage index. This framework uses spatial information derived from multi-parametric qMRI. Data used in this study include eight qMRI maps: T_1-relaxation map, T_2-relaxation map, Dixon fat volume fraction, Dixon water volume fraction, and four DTI maps (apparent diffusion coefficient, fractional anisotropy, mean diffusivity and trace diffusivity). Specifically, using this qMRI data, we developed a Random

Forest-based binary classification (muscle versus non-muscle) framework based on histology-inspired classification labels. We aim to demonstrate that this segmentation framework exhibits consistent performance across different disease stages in the natural history of GRMD. The classification results were validated by MRI data from nine *ex-vivo* GRMD samples and corresponding histopathological images (co-registered to MRI data with an accuracy of 128.48 ± 25.39 µm). In our opinion, this automated imaging biomarker (based on qMRI) is suitable for an accurate assessment of disease progression, and potentially also for early assessment of changes due to treatment interventions.

Materials and Methods

Histology images provide cellular level anatomy using specific staining processes, thereby providing the ground-truth and reflecting the microscopic level of tissue structures. On the other hand, MRI captures anatomical and physiological changes of the tissue using the strong electromagnetic field. In this study, we hypothesize that multi-sequence MRI images reflect the histological findings. To validate this hypothesis, we used an approach illustrated in Figure 4.1: i.e., imaging multi-sequence MRI and taking histology images for nine *ex-vivo* samples of Golden Retriever Muscular Dystrophy animal model. This study was carried out under the approval of the Ethical Committee at the Texas A&M University (IACUC protocol 2015-01110) conform to the general requirements regarding animal studies [20, 39, 40]. Muscle samples were stained by using Mason’s trichrome stain (staining muscle as red, fibrosis as blue, and fat or areas of tissue separation voids as clear appearing white in images) [41, 42], and digitized using a Hamamatsu pathology scanner at 0.23 µm resolution. The detailed information of histology image acquisition was described in Chapter 2.

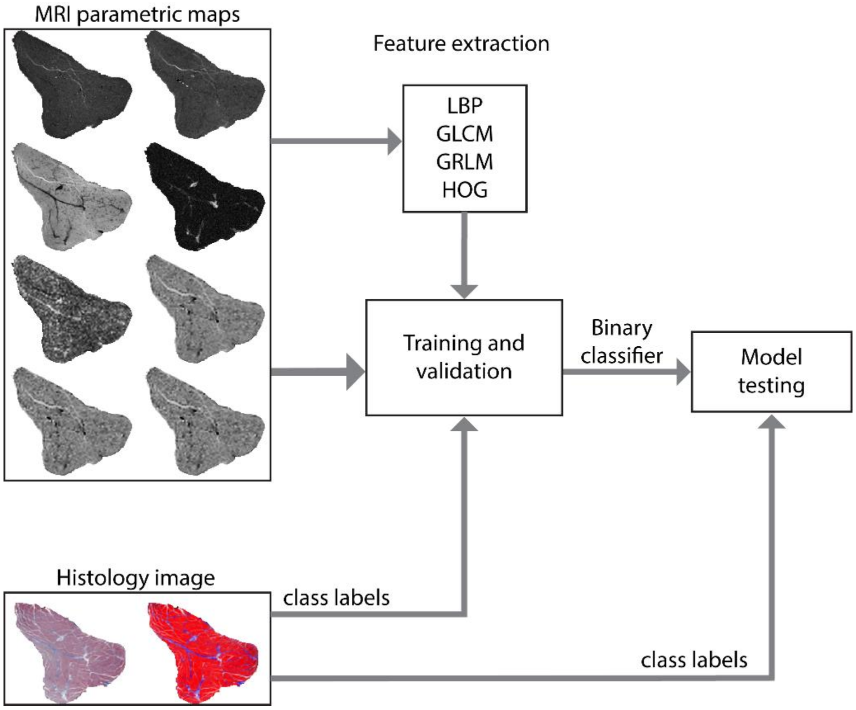

Figure 4.1. A block diagram illustrating experimental setup: starting with data acquisition, processing, masking, segmentation, registration, classification.

MRI Acquisition

Prior to imaging, the samples were placed into 50 ml centrifuge tubes and filled with 7% concentrated agarose gel composition to minimize the motion artifacts due to vibrations caused by the strong magnetic field during multiple MRI acquisitions [43-46]. The MRI images were acquired using an experimental 4.7T Varian Bruker scanner (40 cm horizontal bore and in-house developed birdcage coil system) with a FOV of 30 mm × 30 mm. The imaging protocol, total scanning time 195 min for each sample (listed in Table 4.1) consisted of:

- Morphological T_1w sequence
- Morphological T_2w sequence
- T_1m sequence: 2D multi-slice, gradient echo with four averages.

- T_2m sequence: 2D spin echo.
- 3-point Dixon sequence: T_2w, 2D spin echo with a base image and 2-frequency shifted images [47]
- Diffusion Weighted Imaging sequence: T_2w, 2D spin echo with 6 directions, pulse magnitude of 8.5 G/cm, a pulse duration of (δ) 25 ms, and spacing (Δ) of 25 ms and B=574 s/mm^2.

Table 4.1. MR image acquisition protocol

Sequence	TR (ms)	TE (ms)	FA (◦)	Averages	Matrix	Resolution	Scan time (min)
T_1w	268	6.1	21 & 72	4	256×256	0.1172	38
T_2w	3000	20-80 (Δ20)	-	1	256×256	0.1172	62
3-point Dixon	1000	40	-	1	256×256	0.1172	26
DTI	3000	68	-	1	128×128	0.2344	69

Image Processing and Registration

Digitized histology images were used in conjunction with a color-based segmentation algorithm to generate muscle and non-muscle masks (containing muscle, and combined fibrosis, fat and interstitial space) automatically [48]. T_1m, also referred to as T_1w longitudinal relaxation map, was generated using two T_1w spoiled gradient echo MR images (with two different flip angles) in a linear least squares regression approach known as Despot1 method [49]. T_2m, also referred to as T_2w transverse relaxation map, was generated using four SE images (with four different T_E) in a linear least squares regression algorithm after logarithmic transformation of raw data. Two Dixon maps -water, and fat [47]- were converted into two fractions: i.e., water volume fraction (DWf) and fat volume fraction (DFf) [50]. The DTI images were processed using Camino diffusion MRI toolkit [50] to produce apparent diffusion coefficient (ADC), fractional anisotropy (FA), mean diffusivity (MD), and trace diffusivity (TrD). Finally, all DTI map images were resampled to match T_1w image resolution. Figure 4.2 shows eight quantitative MRI maps used in classification experiments: i.e., T_1m, T_2m, DWf, DFf, ADC, FA, MD, TrD. To facilitate registrations and classifications, both MRI and histology images were masked [51]. These masks are also used to facilitate the classification experiments (training, validation, and testing the results). The masked histology images (raw and segmented) are presented in Figure 4.3.

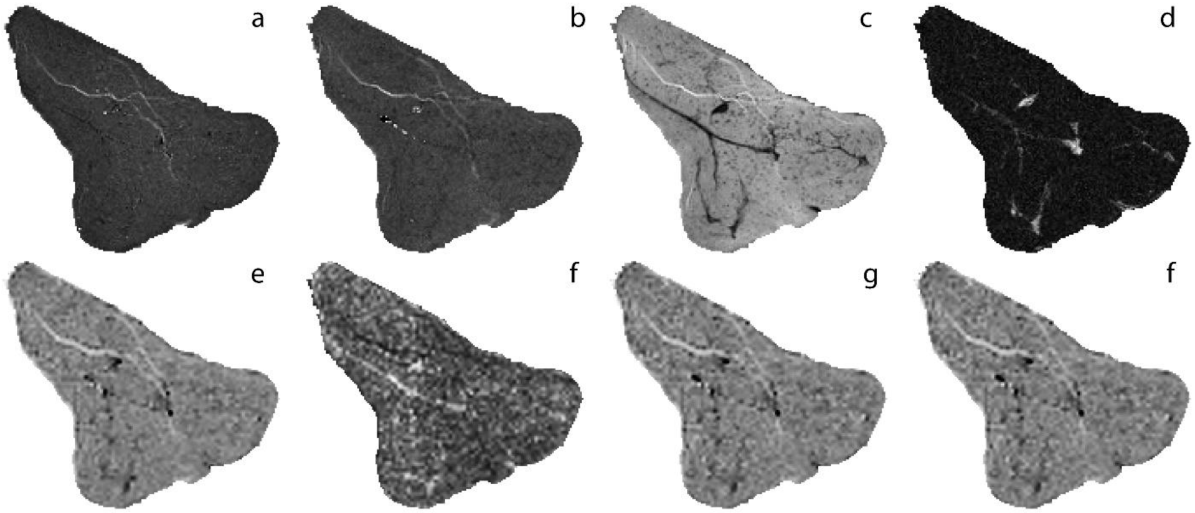

Figure 4.2. MRI map images corresponding to histology slice. (a) T_1-map, (b) T_2-map, (c) Dixon water volume fraction image, (d) Dixon fat volume fraction image, (e) ADC, (f) FA, (g) MD and (h) TrD.

Aligning a 2D histology slice with a 3D MRI volume data is a challenging process due to multiple limitations such as uncertain image orientation, determining the efficient similarity metric for multi-modality images, and tissue deformations. To address these issues, a 3-step registration framework was proposed in Chapter 2 consisting of:

1) Interactive alignment

2) Slice-to-Volume Affine Registration

3) Slice-to-Slice Non-Rigid Registration

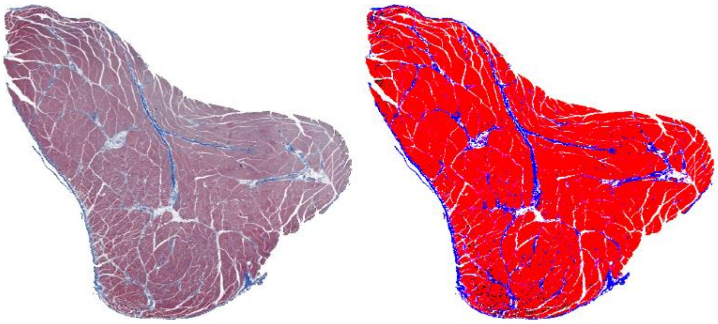

Figure 4.3. Trichrome stained raw histology image (left) and segmented histology image (right) where red represents muscle tissue, blue remarks the fibrosis tissue, and white shows the interstitial tissue.

This comprehensive registration approach provides an accurate pixel-wise registration between 2D histology and multi-parametric 3D MRI data. The registration method uses the intensity based and structural similarities obtained from 3D T_1w and T_2w MRI data for aligning 2D histology image to generate corresponding a 2D MRI image. The registration accuracy was validated by 5 observers calculating the Euclidean distance of five distinctive structural landmark points on MRI corresponding to the initially defined landmarks on histology images for four different initializations. For each sample, we used the registration result with a maximum accuracy of 1.096 ± 0.216 pixels (128.48 µm).

Extraction of Features

Local Binary Patterns

Originally proposed by Ojala et al. [52] and later modified to a rotation and scale invariant approach [53]. LBP represents local texture. In its simplest form, it integrates the information from eight neighborhood pixels by utilizing one-pixel radial filter approach. A pixel-wise LBP was calculated for each MRI map.

Gray-level Co-occurrence Matrix

GLCM also referred to as grey-tone spatial-dependence matrix or second-order histogram, was originally proposed by Haralick et al [54]. When divided by the total number of neighboring pixels in the image, co-occurrence matrix estimates the joint probability of two pixels at a certain distance along a given direction having a particular gray value. We built the co-occurrence matrix in a 5×5 sliding-window neighborhood by averaging four angular directions at distance one. This information was then summarized by nine statistical parameters including contrast, correlation, energy, entropy, homogeneity, sum averages, sum variance, difference variance, and normalized inverse difference moment. This produced a set of 9 GLCM-based pixel-wise features for each parametric MRI map.

Gray-level Run-length Matrix

Originally proposed by Galloway [55], GRLM is subsidiary to the observation that a coarse texture would have relatively longer gray level runs compared to a fine texture. This matrix provides information about runs of pixels with the same gray level values in the specific direction. We constructed GRLM in a 5×5 neighborhood sliding-window averaging four angular directions. This information was summarized by 11 statistical parameters including short run emphasis, long run emphasis gray-level nonuniformity, run length nonuniformity, run percentage, low gray-level run emphasis (LGRE), high gray-level run emphasis, short-run low gray-level run emphasis, short-run high gray-level run emphasis, long run low gray-level run emphasis, and long run high gray-level run emphasis.

Histogram of Oriented Gradient

Originally proposed in a patent application by McConnell [56, 57], HOG assesses local object appearance and shape within an image by summarizing intensity gradients binned into their approximate direction. We computed the HOG features in 2×2-cell blocks and bin resulting gradient magnitude into 9 gradient orientations [58]. This resulted in a feature vector (length 36) for each pixel in all pixel maps separately.

Classification Experiment

All eight quantitative MRI maps (T_1m, T_2m, DWf, DFf, ADC, FA MD, TrD) were within the same framework: i.e., they were co-registered and resampled to the same spatial resolution. Histology validated [48] class labels (muscle and non-muscle), co-registered with MRI through an accurate registration procedure were used as class labels during the classification experiments. Class labels separate the data into two classes: i.e., muscle (positive class) and non-muscle (negative class). The size of class labels was unbalanced with the ratio of positive to negative instances ranging from 3:1 (adult GRMD) to 27:1 (young GRMD). To evaluate the classification performance across different stages in the natural history of GRMD, we have performed a separate classification of each sample in a leave-one-out cross-validation setup.

Our experiment uses a leave-one-sample-out classification approach to train and validate the models for segmentation of pixels representing muscle. This segmentation was validated using the accurately registered histology images with the objective to assess the classification accuracy independently. To deal with overfitting towards majority class (muscle) during the training phase, we first under-sample the data from the over-represented class (muscle). A random under-sampling of 4000 muscle data points from each sample reduces the class distribution skewness in leave-one-out training data by 54%. For all classifications, we used a total of 58 features for all eight qMRI images (Table 4.2): i.e. raw qMRI images, three types of texture descriptors (local binary pattern, gray-level co-occurrence matrix, gray-level run-length matrix), and a gradient image (histogram of oriented gradients). We use a random forest (RF) classifier [59] approach with labeled training data, and the underlying features (incorporating spatial context) to train and validate binary classifier. A total of nine RF classifiers were separately trained and optimized through repeated 10-fold cross-validation. There were two optimization parameters related to RF, namely, the number of predictors tried at each split and the number of total decision trees required to build the random forest. The parameters of RF algorithm are optimized evaluating the performance of the generated models with each candidate parameter set using hold-out validation approach [60]. The final RF models were then built using the optimized parameters and used to classify the corresponding left-out samples. The accuracy, specificity, and sensitivity were calculated for each binary segmentation.

Table 4.2. Different types of features and the corresponding number of features.

Feature combinations	Number of features
Gray value content	8
Gradient information (HOG) features	288
Texture features (LBP + GLCM + GRLM)	168

The resulting segmentation was pruned by a morphological erosion using a line structuring element averaged over four orthogonal directions. The length of the line operator is optimized for each sample separately according to the thickness of the non-muscle structures. The pruned classification (segmented muscle region) is used to calculate muscle percentage index, using equation (4.1).

$$\frac{\sum muscle\ tissues}{\sum muscle + \sum non - muscle} \times 100 \tag{4.1}$$

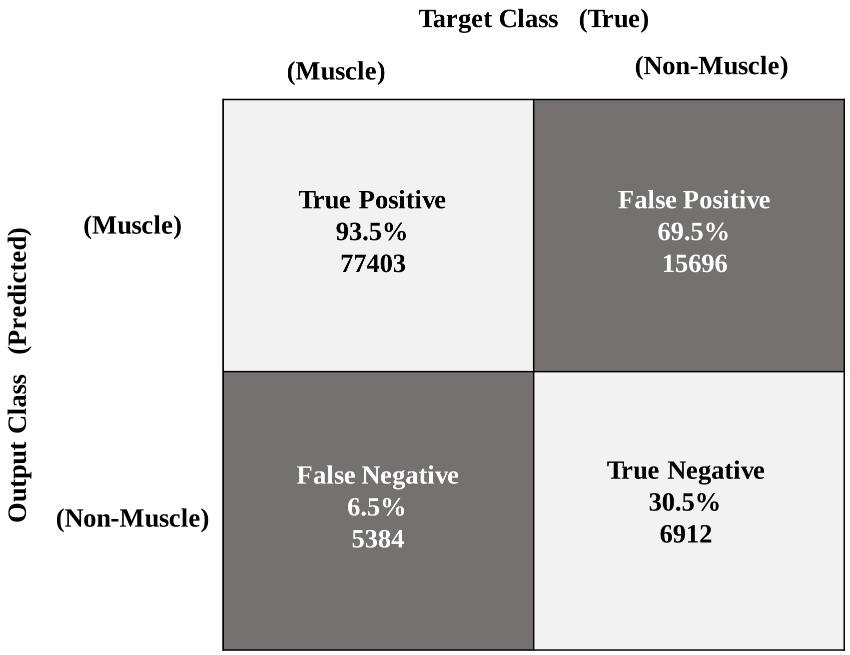

		Target Class (True)	
		(Muscle)	(Non-Muscle)
Output Class (Predicted)	(Muscle)	**True Positive** **93.5%** **77403**	**False Positive** **69.5%** **15696**
	(Non-Muscle)	**False Negative** **6.5%** **5384**	**True Negative** **30.5%** **6912**

Figure 4.4. Averaged confusion matrix over all nine GRMD samples

Results

In our experiment, we used all 58 available features for each qMRI (illustrated in Table 4.2), amounting to a total of 464 features, to classify all pixels as muscle or non-muscle. The raw classification results were pruned to refine isolated pixels afterward. The segmentation quality after pruning was improved as it eliminated a considerable number of isolated non-muscle points which improves overall sensitivity of the proposed method. The confusion matrix, averaged over all nine samples (Figure 4.4) shows 93.5% of muscle points classified correctly, making 6.5% of total muscles incorrectly classified as non-muscles. However, 69.5% of non-muscle pixels were incorrectly classified as muscle, resulting in a 30.5% correct classification for non-muscles.

Table 4.3 reports the final results including the individual and average sensitivity, specificity and accuracy, MPIgt, and MPI derived from qMRI data. We observed a negative correlation (correlation coefficient of -0.79) between the age and MPIgt, with MPIgt for young animals significantly higher (average 84%) than MPIgt for old animals (average 70%) as measured by two-tailed student T-test assuming unequal variances (p=0.05). Correspondingly, we observed a weaker negative correlation (correlation coefficient of -0.33) between the age and MPI, with MPI for young samples higher (average 92%) than MPIgt for old samples (average 90%).

Table 4.3. Muscle percentage index derived from histology and MRI data for nine GRMD samples

Age months	Age category	MPIgt	MPI	Sensitivity	Specificity	Accuracy
3	Young	0.81	0.90	0.93	0.22	0.80
12	Young	0.85	0.95	0.97	0.14	0.84
12	Young	0.84	0.97	0.98	0.11	0.85
15	Young	0.81	0.86	0.90	0.34	0.80
3	Young	0.82	0.98	0.99	0.08	0.83
42	Adult	0.76	0.83	0.92	0.44	0.80
3	Young	0.92	0.87	0.90	0.50	0.87
18	Adult	0.71	0.94	0.98	0.17	0.76
48	Adult	0.62	0.92	0.95	0.13	0.64
Average				0.95	0.24	0.80

A negative correlation between age and accuracy is observed (correlation coefficient of -0.75), ranging from -0.36 for young samples to -0.99 for old samples, implying lower accuracy for old samples. Correspondingly, this is also reflected in a boxplot (Figure 4.5) illustrating the difference between MPIgt and MPI for both age categories. There is no significant difference between MPI for young (average 0.86%) and adult (average 0.82%) samples as measured by two-tailed student T-test assuming unequal variances (p=0.7). On average, MPI showed an overestimation of 9.8% for young samples.

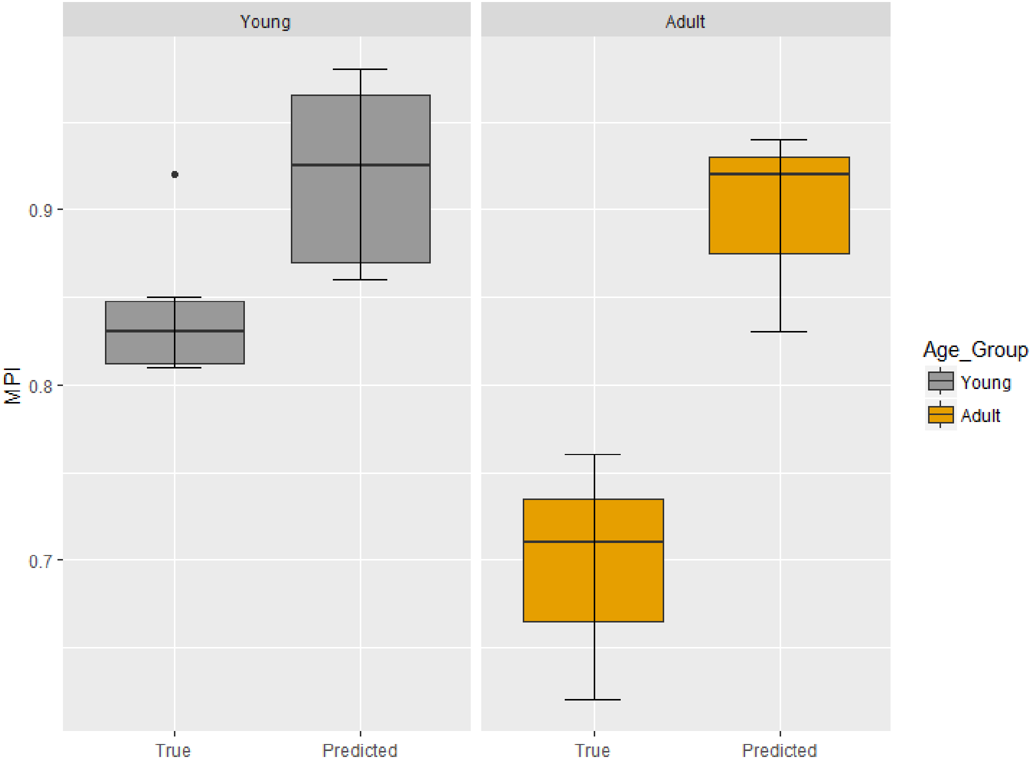

Figure 4.5. Boxplot illustrating true and predicted Muscle Percentage Index for two GRMD categories, i.e. young (3-15 months) and adult (18- 48 months)

We observed a positive correlation (correlation coefficient of 0.73), between MPIgt and MPI for young samples, and a negative correlation (correlation coefficient of -0.91), between MPIgt and MPI for adult samples. Figure 4.6 shows the histology and MRI provided muscle segmentation for a young (15 months old) GRMD sample, constituting of 81% muscle tissue. The rest of the tissues (19%) was classified as non-muscle (representing fat, fiber or interstitial tissues).

Overall, the MPI derived from qMRI using this classification approach was overestimated by 16.5%, with 9.8% for young samples and 29.9% for adult samples. The variance of this overestimation was for adult samples was twice the variance observed for young samples.

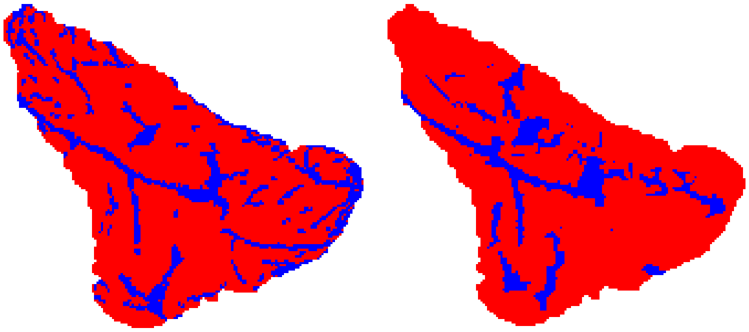

Figure 4.6. Histology derived (left) and multi-sequence MRI derived (right) muscle segmentation for a sample of 15 months old GRMD dog. The red color indicates the healthy muscle tissues, whereas the blue color specifies non-muscle locations.

Discussion

Past attempts to quantify MPI using MRI were based on manual segmentation [22-29], while a handful of them focused on semi-automated computerized method [17]. Vohra et al. [25] labeled the muscle regions as contractile and non-contractile as segmenting T_1w MRI images with a threshold selected by maximizing the entropy within the classes after manual segmentation of muscle groups. The validation of class segmentation was measured using interclass correlation coefficient varying values for muscle groups 0.81-1 for contractile and 0.87-1 for non-contractile class. They reported a significant difference of non-contractile CSA between control and DMD patients. Wokke et. al. [31] used contractile CSA (assessed by an arbitrary threshold) to differentiate healthy and DMD patients. They observed a significant increase of contractile CSA with aging for healthy patients but not for DMD patients. Godi et.al. [35] segmented muscles on T_1w images manually and then calculated the MVI measure using thresholding the segmented muscle region to assess disease progression. They presented a significant decrease on MVI measure between control and DMD patients, also they observed a decrease of MVI with aging among the DMD patient group.

In our method, we utilized different texture and gradient analysis components in a random forest classification framework to calculate MPI as an imaging biomarker to assess the DMD disease progression. Due to the automated muscle segmentation scheme, the current method presents a reproducible framework not limited by manual segmentation. The important difference to previous literature is that the current method is validated by histopathologic images, absent in any of the previous methods. Histology inspired validation provides a strong evidence of the accuracy for the automatically generated MPI as an imaging biomarker for disease progression. Another contribution of the present study is that it combines different levels of information in qMRI images (gray values, texture, and gradients), and utilize the predictive power of RF algorithm to classify tissue as muscles and non-muscles. The features constituted the final feature set without any attempt for feature selection. The rationale behind was to utilize the texture and gradient analysis information as maximum as possible in distinguishing between muscle and non-muscle regions. The localized texture analysis discovers the patterns of neighboring pixels in qMRI maps. As the skeletal muscle structure slowly degenerates into fat and fibrosis tissues in DMD, neighborhood texture difference serves an important marker to indicate the presence of other non-muscle components at the surrounding of muscle tissues.

In terms of performance, our method overestimated the MPI by 16.5%, with 9.8% for young samples and 29.9% for adult samples. The variance of this overestimation was for adult samples was twice the variance observed for young samples. Majority of samples experience low specificity due to overprediction of muscle classes. Particularly, low SP was observed for four young samples (3 and 12 months), and moderate SP for two young samples (3 and 15 months). The significant amount difference between the muscle and remaining tissues limited the number of instances for each class which directly affected the accuracy of the classification. Additionally, the non-muscle tissue in the classification experiment mostly provided by adult sample which was deformed during the pathological processes due to loss of structural completeness. On the other hand, the missing tissue regions occurred in the region of samples was assigned in the non-muscle tissue class which may cause ambiguity for the classifier model due to the ambiguity of tissue type in those regions. Among the age groups of GRMD subjects, a slight decrease in classification accuracy was observed as increasing age of groups with a linear fashion (83.3 % to 72 %). The youngest littermates show slightly varying accuracies between 83% and 87%. Older subjects show closer accuracies within the age groups except for adult subject group due to the oldest GRMD sample which has undergone a significant level of tissue distortions during pathological processes.

Histology derived segmentation clearly depicts the lack of well-defined non-muscle regions in most of the 3 months old samples as the disease is only in onset state. The disease may have progressed in a bit older samples (e.g. 12 months) and manifested in a larger proportion of non-muscle tissues, but the non-muscle composition may not be as same as an adult sample (e.g. 42 months or 48 months). Note that in our study, more than half of the non-muscle examples emerged from the adult samples. We also observed a considerable number of isolated non-muscle points in young samples, a possible indication of the disease onset state may have been removed by the pruning step, resulting in a lower SP and an over-estimation of MPI. Having a relatively small dataset, consisting of six young and three adult samples, muscle and non-muscle classes having an odd distribution (3.66:1). To balance the class ratio during the training, we adopted a simple approach of random under-sampling of an equal number of muscle points, rather than creating using oversampling. We apprehend that the non-muscle classification accuracy may improve by including additional samples.

Conclusions and Future Perspectives

The current method uses a classification based automated muscle segmentation to calculate the MPI as a potential MRI marker to assess the disease severity in DMD. Our assessment of MPI demonstrated that histology derived mean muscle percentage index is significantly different in two age categories. Our classification based automatic muscle segmentation framework achieved an average accuracy of 80% utilizing 58 features derived from all MRI parametric sequences and five different texture descriptors. The significant level of sensitivity for the classification model was obtained for each sample while the lower level of specificity was observed potentially affected due to the lower number of training examples. Histology-inspired validation on young and adult samples demonstrated a close similarity between ground truth and predicted muscle tissues.

Finally, this study leads to important research avenues. For instance, unlike a crude binary classification, a more suitable approach for muscle segmentation could be to identify the functional relationships between the tissue composition and MRI parametric pixel maps of dystrophic muscles. It would also be interesting to assess the efficacy of T_1w and T_2w images, in combination with parametric maps or at the individual level, for automated muscle segmentation.

References

[1] J. L. Thibaud, N. Azzabou, I. Barthelemy, S. Fleury, L. Cabrol, S. Blot, *et al.*, "Comprehensive longitudinal characterization of canine muscular dystrophy by serial NMR imaging of GRMD dogs," *Neuromuscular Disorders*, vol. 22, pp. S85-S99, 2012.

[2] A. Lerario, S. Bonfiglio, M. Sormani, A. Tettamanti, S. Marktel, S. Napolitano, *et al.*, "Quantitative muscle strength assessment in duchenne muscular dystrophy: longitudinal study and correlation with functional measures," *BMC Neurology,* vol. 12, pp. 1-8, 2012.

[3] T. Y. Kostrominova, D. S. Reiner, R. H. Haas, R. Ingermanson, and P. M. McDonough, "Chapter Seven - Automated Methods for the Analysis of Skeletal Muscle Fiber Size and Metabolic Type," in *International Review of Cell and Molecular Biology*. vol. 306, K. W. Jeon, Ed., ed: Academic Press, 2013, pp. 275-332.

[4] K. G. Hollingsworth, P. Garrood, M. Eagle, K. Bushby, and V. Straub, "Magnetic resonance imaging in duchenne muscular dystrophy: Longitudinal assessment of natural history over 18 months," *Muscle & Nerve,* vol. 48, pp. 586-588, 2013.

[5] A. B. Martins-Bach, J. Malheiros, B. Matot, P. C. M. Martins, C. F. Almeida, W. Caldeira, *et al.*, "Quantitative T2 Combined with Texture Analysis of Nuclear Magnetic Resonance Images Identify Different Degrees of Muscle Involvement in Three Mouse Models of Muscle Dystrophy: mdx, Largemyd and mdx/Largemyd," *PLOS ONE,* vol. 10, pp. 1-16, 2015.

[6] S. Mathur, R. S. Vohra, S. A. Germain, S. Forbes, N. D. Bryant, K. Vandenborne, *et al.*, "Changes in muscle T2 and tissue damage after downhill running in mdx Mice," *Muscle & Nerve,* vol. 43, pp. 878-886, 2011.

[7] W. Aherne, "A method of determining the cross sectional area of muscle fibres," *Journal of the Neurological Sciences,* vol. 7, pp. 519-528, 1968.

[8] L. C. Maxwell, J. A. McNamara, D. S. Carlson, and J. A. Faulkner, "Histochemistry of fibres of masseter and temporalis muscles of edentulous monkeys Macaca mulatta," *Archives of Oral Biology,* vol. 25, pp. 87-93, 1980.

[9] C. D. Shorey and K. W. Cleland, "Problems associated with the morphometric measurement of transverse skeletal muscle fibers: I. Analysis of frozen sections," *The Anatomical Record,* vol. 207, pp. 523-531, 1983.

[10] C. A. Schneider, W. S. Rasband, and K. W. Eliceiri, "NIH Image to ImageJ: 25 years of image analysis," *Nature Methods,* vol. 9, pp. 671-675, 2012.

[11] F. Liu, A. L. Mackey, R. Srikuea, K. A. Esser, and L. Yang, "Automated image segmentation of haematoxylin and eosin stained skeletal muscle cross-sections," *Journal of Microscopy*, vol. 252, pp. 275-285, 2013.

[12] J. N. Kornegay, J. R. Bogan, D. J. Bogan, M. K. Childers, J. Li, P. Nghiem, *et al.*, "Canine Models of Duchenne Muscular Dystrophy and Their Use in Therapeutic Strategies," *Mammalian Genome,* vol. 23, pp. 85-108, 2012.

[13] R. S. Vohra, S. Mathur, N. D. Bryant, S. C. Forbes, K. Vandenborne, and G. A. Walter, "Age-related T2 changes in hindlimb muscles of mdx mice," *Muscle & Nerve,* vol. 53, pp. 84-90, 2016.

[14] E. C. Qin, L. Jugé, S. A. Lambert, V. Paradis, R. Sinkus, and L. E. Bilston, "In Vivo Anisotropic Mechanical Properties of Dystrophic Skeletal Muscles Measured by Anisotropic MR Elastographic Imaging: The mdx Mouse Model of Muscular Dystrophy," *Radiology*, vol. 273, pp. 726-735, 2014.

[15] J. Park, J. Wicki, S. E. Knoblaugh, J. S. Chamberlain, and D. Lee, "Multi-Parametric MRI at 14T for Muscular Dystrophy Mice Treated with AAV Vector-Mediated Gene Therapy," *PLOS ONE,* vol. 10, pp. 1-24, 2015.

[16] T. Yokota, Q.-l. Lu, T. Partridge, M. Kobayashi, A. Nakamura, S. Takeda, *et al.*, "Efficacy of systemic morpholino exon-skipping in duchenne dystrophy dogs," *Annals of Neurology,* vol. 65, pp. 667-676, 2009.

[17] Z. Fan, J. Wang, M. Ahn, Y. Shiloh-Malawsky, N. Chahin, S. Elmore, *et al.*, "Characteristics of magnetic resonance imaging biomarkers in a natural history study of golden retriever muscular dystrophy," *Neuromuscular Disorders,* vol. 24, pp. 178-191, 2014.

[18] B. H. Wokke, J. C. Van Den Bergen, M. T. Hooijmans, J. J. Verschuuren, E. H. Niks, and H. E. Kan, "T2 relaxation times are increased in Skeletal muscle of DMD but not BMD patients," *Muscle & Nerve,* vol. 53, pp. 38-43, 2016.

[19] M. T. Hooijmans, N. Doorenweerd, C. Baligand, J. J. G. M. Verschuuren, I. Ronen, E. H. Niks, *et al.*, "Spatially localized phosphorous metabolism of skeletal muscle in Duchenne muscular dystrophy patients: 24–month follow-up," *PLOS ONE,* vol. 12, pp. 1-15, 2017.

[20] R. J. Willcocks, I. A. Arpan, S. C. Forbes, D. J. Lott, C. R. Senesac, E. Senesac, *et al.*, "Longitudinal measurements of MRI-T2 in boys with Duchenne muscular dystrophy: Effects of age and disease progression," *Neuromuscular Disorders,* vol. 24, pp. 393-401, 2014.

[21] I. Arpan, R. J. Willcocks, S. C. Forbes, R. S. Finkel, D. J. Lott, W. D. Rooney, *et al.*, "Examination of effects of corticosteroids on skeletal muscles of boys with DMD using MRI and MRS," *Neurology,* vol. 83, pp. 974-980, 2014.

[22] S. Ponrartana, L. Ramos-Platt, T. A. L. Wren, H. H. Hu, T. G. Perkins, J. M. Chia, *et al.*, "Effectiveness of Diffusion Tensor Imaging in Assessing Disease Severity in Duchenne Muscular Dystrophy: Preliminary Study," *Pediatric Radiology,* vol. 45, pp. 582-589, 2015.

[23] A. Mankodi, C. A. Bishop, S. Auh, R. D. Newbould, K. H. Fischbeck, and R. L. Janiczek, "Quantifying disease activity in fatty-infiltrated skeletal muscle by IDEAL-CPMG in Duchenne muscular dystrophy," *Neuromuscular Disorders,* vol. 26, pp. 650-658, 2016.

[24] M. T. Hooijmans, B. M. Damon, M. Froeling, M. J. Versluis, J. Burakiewicz, J. J. G. M. Verschuuren, *et al.*, "Evaluation of skeletal muscle DTI in patients with duchenne muscular dystrophy," *NMR in Biomedicine,* vol. 28, pp. 1589-1597, 2015.

[25] R. Vohra, A. Accorsi, A. Kumar, G. Walter, and M. Girgenrath, "Magnetic Resonance Imaging Is Sensitive to Pathological Amelioration in a Model for Laminin-Deficient Congenital Muscular Dystrophy (MDC1A)," *PLOS ONE,* vol. 10, pp. 1-12, 2015.

[26] U. Bonati, P. Hafner, S. Schädelin, M. Schmid, A. Naduvilekoot Devasia, J. Schroeder, *et al.*, "Quantitative muscle MRI: A powerful surrogate outcome measure in Duchenne muscular dystrophy," *Neuromuscular Disorders,* vol. 25, pp. 679-685, 2015.

[27] M. Gaeta, S. Messina, A. Mileto, G. L. Vita, G. Ascenti, S. Vinci, *et al.*, "Muscle fat-fraction and mapping in Duchenne muscular dystrophy: evaluation of disease distribution and correlation with clinical assessments," *Skeletal Radiology,* vol. 41, pp. 955-961, 2012.

[28] L. T. Bish, M. M. Sleeper, S. C. Forbes, K. J. Morine, C. Reynolds, G. E. Singletary, *et al.*, "Long-Term Systemic Myostatin Inhibition via Liver-Targeted Gene Transfer in Golden Retriever Muscular Dystrophy," *Human Gene Therapy,* vol. 22, pp. 1499-1509, 2011.

[29] C. R. Heier, A. D. Guerron, A. Korotcov, S. Lin, H. Gordish-Dressman, S. Fricke, *et al.*, "Non-Invasive MRI and Spectroscopy of mdx Mice Reveal Temporal Changes in Dystrophic Muscle Imaging and in Energy Deficits," *PLOS ONE*, vol. 9, pp. 1-12, 2014.

[30] J. Wang, Z. Fan, K. Vandenborne, G. Walter, Y. Shiloh-Malawsky, H. An, *et al.*, "A computerized MRI biomarker quantification scheme for a canine model of Duchenne muscular dystrophy," *International Journal of Computer Assisted Radiology and Surgery,* vol. 8, pp. 763-774, 2013.

[31] B. H. Wokke, J. C. van den Bergen, M. J. Versluis, E. H. Niks, J. Milles, A. G. Webb, *et al.*, "Quantitative MRI and strength measurements in the assessment of muscle quality in Duchenne muscular dystrophy," *Neuromuscular Disorders,* vol. 24, pp. 409-416, 2014.

[32] S. Mathur, D. J. Lott, C. Senesac, S. A. Germain, R. S. Vohra, H. L. Sweeney, *et al.*, "Age-Related Differences in Lower-Limb Muscle Cross-Sectional Area and Torque Production in Boys With Duchenne Muscular Dystrophy," *Archives of Physical Medicine and Rehabilitation,* vol. 91, pp. 1051-1058, 2010.

[33] P. Richards, W. R. Saywell, and P. Heywood, "Pseudohypertrophy of the temporalis muscle in Xp21 muscular dystrophy," *Developmental Medicine & Child Neurology,* vol. 42, pp. 786-787, 2000.

[34] H. Akima, D. Lott, C. Senesac, J. Deol, S. Germain, I. Arpan, *et al.*, "Relationships of thigh muscle contractile and non-contractile tissue with function, strength, and age in boys with Duchenne muscular dystrophy," *Neuromuscular Disorders,* vol. 22, pp. 16-25, 2012.

[35] G. Claudia, A. Alessandro, N. Francesca, P. S. C., S. Corrado, N. Sara, *et al.*, "Longitudinal MRI quantification of muscle degeneration in Duchenne muscular dystrophy," *Annals of Clinical and Translational Neurology,* vol. 3, pp. 607-622, 2016.

[36] T. C. Roberts, K. E. M. Blomberg, G. McClorey, S. E. L. Andaloussi, C. Godfrey, C. Betts, *et al.*, "Expression Analysis in Multiple Muscle Groups and Serum Reveals Complexity in the MicroRNA Transcriptome of the mdx Mouse with Implications for Therapy," *Molecular Therapy. Nucleic Acids,* vol. 1, pp. 1-11, 2012.

[37] R. J. Willcocks, W. D. Rooney, W. T. Triplett, S. C. Forbes, D. J. Lott, C. R. Senesac, *et al.*, "Multicenter prospective longitudinal study of magnetic resonance biomarkers in a

large duchenne muscular dystrophy cohort," *Annals of Neurology,* vol. 79, pp. 535-547, 2016.

[38] J. N. Kornegay, "The golden retriever model of Duchenne muscular dystrophy," *Skeletal Muscle,* vol. 7, pp. 1-21, 2017.

[39] Committee for the Update of the Guide for the Care and Use of Laboratory Animals, "Guide for the care and use of laboratory animals," ed. Washington, D.C.: National Academy Press, 2011.

[40] National Institutes of Health. (2015, 1 Sept). *Office of Laboratory Animal Welfare - Public Health Service Policy on Humane Care and Use of Laboratory Animals*.

[41] J. A. Kiernan, *Histological and Histochemical Methods*: Cold Spring Harbor Laboratory Press, 2008.

[42] D. M. Wikeley, *Manual of histological and histochemical methods used for larval evaluation*. Hobart , Tasmania: Marine Resources Division, Marine Research Laboratories-Taroona, Dept. of Primary Industry and Fisheries, 1994.

[43] P. W. Hales, R. A. B. Burton, C. Bollesdorff, F. Mason, M. Bishop, D. Gavaghan, *et al.*, "Progressive changes in T_1, T_2 and left-ventricular histo-architecture in the fixed and embedded rat heart," *NMR In Biomedicine,* vol. 24, pp. 836-843, 2010.

[44] A. Hellerbach, V. Schuster, A. Jansen, and J. Sommer, "MRI Phantoms - Are There Alternatives to Agar?," *PLOS One,* vol. 8, pp. 1-8, 2013.

[45] P. E. Thelwall, T. M. Shepherd, G. J. Stanisz, and S. J. Blackband, "Effects of Temperature and Aldehyde Fixation on Tissue Water Diffusion Properties, Studied in an Erythrocyte Ghost Tissue Model," *Magnetic Resonance in Medicine,* vol. 56, pp. 282-289, 2006.

[46] R. Pomfret, K. Sillay, and G. Miranpuri, "Investigation of the electrical properties of agarose gel: characterization of concentration using nyquist plot phase angle and the implications of a more comprehensive in vitro model of the brain," *Annals of Neurosciences,* vol. 20, pp. 99-107, 2013.

[47] G. H. Glover and E. Schneider, "Three-point Dixon technique for true water/fat decomposition with B0 inhomogeneity correction," *Magn Reson Med,* vol. 18, pp. 371-383, 1991.

[48] S. McConnell, "Automatic Canine Muscle Histology Image Segmentation Based on RGB Histogram," Master Unpublished master's thesis, Electrical and Computer Engineering, Texas A&M University, College Station, TX, 2016.

[49] S. C. Deoni, B. K. Rutt, and T. M. Peters, "Rapid combined T1 and T2 mapping using gradient recalled acquisition in the steady state," *Magnetic Resonance in Medicine,* vol. 49, pp. 515-526, 2003.

[50] S. Reeder, C. Hines, H. Yu, C. McKenzie, and J. Brittain, "On the definition of fat-fraction for in vivo fat quantification with magnetic resonance imaging," presented at the Proceedings of the Seventeenth Meeting of the International Society for Magnetic Resonance in Medicine, Hawaii, USA, 2009.

[51] A. Eresen, S. McConnell, S. M. Birch, J. F. Griffin, J. N. Kornegay, and J. X. Ji, "Localized MRI and histological image correlation in a canine model of duchenne muscular dystrophy," *Conf Proc IEEE Eng Med Biol Soc,* vol. 2016, pp. 4083-4086, Aug 2016.

[52] T. Ojala, M. Pietikäinen, and D. Harwood, "A comparative study of texture measures with classification based on featured distributions," *Pattern Recognition,* vol. 29, pp. 51-59, 1996.

[53] T. Ojala, M. Pietikainen, and T. Maenpaa, "Multiresolution gray-scale and rotation invariant texture classification with local binary patterns," *IEEE Transactions on Pattern Analysis and Machine Intelligence,* vol. 24, pp. 971-987, 2002.

[54] R. M. Haralick, K. Shanmugam, and I. H. Dinstein, "Textural features for image classification," *IEEE Transactions on Systems, Man, and Cybernetics,* vol. SMC-3, pp. 610-621, 1973.

[55] M. M. Galloway, "Texture analysis using gray level run lengths," *Computer Graphics and Image Processing,* vol. 4, pp. 172-179, 1975.

[56] R. K. McConnell, "Method of and apparatus for pattern recognition," ed: Google Patents, 1986.

[57] W. T. Freeman and M. Roth, "Orientation Histograms for Hand Gesture Recognition," USA Patent, 1994.

[58] N. Dalal and B. Triggs, "Histograms of Oriented Gradients for Human Detection," presented at the Proceedings of the 2005 IEEE Computer Society Conference on Computer Vision and Pattern Recognition (CVPR'05) - Volume 1 - Volume 01, 2005.

[59] L. Breiman, "Random Forests," *Machine Learning*, vol. 45, pp. 5-32, October 01 2001.

[60] R Core Team, "R: A Language and Environment for Statistical Computing," ed. Vienna, Austria: R Foundation for Statistical Computing, 2017.

CHAPTER V

SUMMARY AND GENERAL DISCUSSION

DMD disease affects the muscular tissue severely and causes structural changes in the muscles fibers. The clinical observation of the disease progression is assessed with invasive methods including, blood test, genetic evaluations, and muscle biopsies. The repetition of these techniques is limited due to the complexity and invasiveness of these procedures, MRI imaging has potential to provide valuable information about the muscular tissues due to a high soft tissue contrast capability. MRI imaging has a multitude of different sequences, all reflecting different properties of the scanned tissues. To increase the reproducibility of the evaluation in the DMD disease, identification of the quantitative MRI biomarkers become an important and required goal. The quantitative MRI parameters showed the suitability of MRI images for diagnosis of the disease. However, they do not correlate directly with biological changes in muscular tissues. On the other hand, the texture analysis presents an excellent computational method to assess heterogeneity in biomedical images. Therefore, texture analysis of MRI images has a potential to produce robust and sensitive identifiers for assessment of muscle changes during the progression and potential treatment of DMD diseases.

The aim of this thesis is to develop and evaluate quantitative, texture-based imaging biomarkers extracted form qMRI, reflecting the changes in aging GRMD muscle. The procedure defined in this thesis was addressed following questions:

- What kind of methods are needed to align a histology slice with an MRI volume?
- Which MRI imaging sequences provides a better understanding of the disease progression?

- Which textural analysis methods of MRI sequences result in better performance for assessment of clinical outcomes for GRMD disease?
- Which locally extracted features from quantitative MRI images utilizes the MPI as a biomarker of GRMD disease among age groups?

Chapter 1 presents the introduction of this thesis and outlines the principle concepts included in this thesis. That includes a detailed introduction to muscular dystrophies, the biological background of the Duchenne muscular dystrophy, animal models of DMD, noninvasive imaging modalities used in DMD, and qualitative and quantitative methods available to diagnose GRMD.

Chapter 2 introduces a framework to generate an oblique MRI slice from 3D T_1w and T_2w MRI image and to co-register these slices to a 2D histology image. The primary elements of the methodology are 1) interactive histology and MRI volume alignment for initialization, 2) utilizing T_1w and T_2w images for a better image, 3) a similarity metric combining mutual information and gradient information, and 4) elastic registration of histology images and multi-sequence MRI images. The framework includes three consecutive registration steps. The initial alignment of the histology slice in 3D volume determined by users using a 3D mouse and the orientation parameters were tuned using non-gradient based optimization technique. In the final step of the framework, employed elastic registration reduces the deformation effects on the histology images. For evaluation of the registration framework, four different registration experiments were completed with four users initializing the registration procedure. The registration results were validated by five different observers defining five distinct landmark points on the resulting MRI image obtained after registration. The Euclidean distance was used to calculate RMS error as misalignment measure. The resulting average accuracy was 148.83 ± 34.96 µm and the best accuracy was 128.48

± 25.39 μm for 10 samples. The detailed registration results for the experiments are provided in Table A1 (Appendix A).

- For evaluation of the proposed similarity metric, a total of 48 experiments was completed; i.e. individual and both MRI images as input for proposed similarity metric and mutual information using four initializations by the users.
- The accuracy of each registration experiment was evaluated by five observers.
- This work was used as the initial step for MRI quantification based on the biological tissue contents. The spatial alignment of histology and MRI images enables the quantitative studies aiming to research localized correspondence between invasive biological findings and noninvasive imaging modality results.

Chapter 3 investigates disease severity in GRMD disease using textural analysis methods with multi-metric quantitative MRI images using data acquired with 3T Siemens Verio clinical scanner. Total of forty-one textural features was generated using five different feature extraction methods: i.e. first order statistics, gray level co-occurrence matrix based features, run-length matrix based features, local binary patterns and statistics of wavelet transformed images. Utilizing a soft-margin support vector machines approach, the textural features of two qualitative (T_1w and T_2w) and 4 quantitative MRI parameter images (T_1m, T_2m, Dixon water fraction, and Dixon fat fraction) are analyzed to select imaging modality and feature method for GRMD disease evaluation. The cross-validated classification model performances for qualitative (T_1w and T_2w), quantitative MRI relaxation (T_1m and T_2m) and Dixon (Water and muscle fraction) images are compared. Among these imaging groups and feature methods, T_2 relaxation maps showed the 100% classification accuracy for disease severity assessment. The detailed list of the feature methods resulting in the highest accuracy w provided in Table B2, Table B3 and Table B4 (Appendix B).

Chapter 4 uses muscle percentage index as an imaging biomarker to quantify muscle degeneration in GRMD disease employing a machine learning approach. The MRI form nine GRMD muscle samples scanned using an experimental 4.7T Varian Bruker MRI scanner. Trichrome stained histology images of each muscle were segmented into two classes: muscle and non-muscle. In our earlier study, we measured the correlation of MRI and histology image using both 3T and 4.7T MRI data. The 3T MRI data did not show a coherent correlation between MRI and tissue compositions (muscle, fibrosis) obtained from histology images. Therefore, 4.7T MRI data was used in this study. The histology images were registered to 3D MRI volume data and corresponding quantitative MRI images for all sequences, T_1 (T_1m), T_2 (T_2m), Dixon (Water and fat mass fraction) and DTI (FA, ADC, MD, and TrD). Total of 464 features (58 features from each qMRI data) was generated from MRI images for the whole sample using four feature extraction methods (local binary patterns, gray-level co-occurrence matrix, gray-level run-length matrix, HOG features). The classifier models were optimized in a leave-one-out cross-validation approach, to evaluate the classification performance across different stages of GRMD. MPI was generated from a final classification result, for each sample separately, by a morphological filter as pruning method. The muscle class was compensated in muscle percentage index as a biomarker for disease progression. The classification experiments were completed with an average classification accuracy of 80% for nine GRMD muscle samples across all age categories (3 - 48) providing a validated MRI-based imaging biomarker for assessment of disease severity. The results showed that muscle percentage index reflects the biological observations of histology images.

Quantification of tissue changes in MRI images has the potential to improve disease diagnosis, monitoring the disease progression, evaluation of severity and predicting the clinical outcomes. The main challenge is to identify the suitable MRI imaging modality and the quantitative measure method for clinical applications.

This thesis contributes several methods to address this challenge. First, we developed a method to link a high-resolution histology image and low-resolution MRI volume data accurately. This method will provide the direct analysis of MRI image characteristics and biological changes on histology images. This study demonstrated that signatures of multi-metric MRI images provided a better correspondence between MRI and histology images. Therefore, we hypothesize that combination of information obtained from multiple MRI modalities may support better understanding effects of the altering tissues.

Second, we demonstrated that textural analysis of quantitative MRI images showed potential as a valuable non-invasive method for disease detection and evaluation of disease progression of GRMD disease. The preclinical studies included in this study presented that clinical outcomes and treatment effects may be monitored and assessed by the textural features obtained with five different feature extraction methods. In addition, we showed that the quantitative MRI images can be used to classify the tissue content of the muscle samples and automatically generated MPI measure reflected the changes of muscle content change throughout the disease.

The processes of development and implementation of disease biomarkers for GRMD disease diagnosis, severity grading, monitoring treatment response and clinical outcome prediction requires carefully designed strategy. The general approach of the studies focused on textural analysis was to extract features using T_1w or T_2w images for diagnosis without including additional information from other qualitative and quantitative MRI data. The effects of the GRMD disease may not be detected using only one imaging data due to multiple changes in tissues and these images are not robust to environmental changes. Other studies analyzed the variation of quantitative MRI metric changes of whole muscle data for diagnosis and monitoring the disease progression. The alteration of the muscle tissue throughout the stages of the GRMD disease affect the quantitative parameters differently; therefore, averages of the quantitative metrics may not reflect the disease progression. Many studies used the muscle tissue volume change for diagnosis and disease severity. However, muscle content was segmented either manually or using simple thresholding on MRI images. These methods are lack of histology image validation and don't evaluate the relationship between histology and MRI data.

To develop non-invasive MRI biomarkers utilizing heterogeneity on muscle textures for disease severity assessment and response monitoring, a carefully selected validation method is required. Additionally, a balanced number of subjects and features, combination of multi-sequence MRI data and independent test datasets will be improving the validity of determined biomarkers. Future studies need to give carefully design experiments selecting these requirements for reliably accurate performances.

In conclusion, monitoring outcomes of treatments and prediction of outcomes using non-invasive MRI biomarkers using tissue heterogeneity could be widely used in clinical applications. These imaging biomarkers could be used to detect most suitable treatment options for the patients, individually. For clinical approval, further studies using large-scale datasets are required.

APPENDIX A

DETAILED REGISTRATION RESULTS

Table A1. Detailed registration accuracy assessments for each experiment (T_1w, T_2w) with MI and MIC metrics by five observers

Sample	MRI	Observer 1		Observer 2		Observer 3		Observer 4		Observer 5	
		MI	MIC	MI	MIC	MI	MIC	MI	MIC	MI	MIC
1	T_1w	5.68	5.58	5.54	4.47	6.28	6.28	7.46	5.28	5.79	6.85
	T_2w	6.84	4.95	5.74	4.46	6.60	6.30	8.31	8.33	7.53	7.17
	Multi	6.43	2.80	7.15	2.70	7.76	2.74	7.56	2.50	7.53	3.83
2	T_1w	5.69	3.16	3.38	3.66	3.83	4.39	3.67	3.00	4.89	4.68
	T_2w	3.83	3.38	3.70	3.59	4.51	3.67	2.82	3.97	5.94	6.53
	Multi	4.27	2.26	4.12	2.31	5.39	1.95	5.32	2.16	7.75	3.27
3	T_1w	4.58	4.47	2.92	4.02	4.04	4.55	3.55	4.74	5.05	4.71
	T_2w	4.90	2.86	4.12	3.96	4.16	2.96	4.01	3.07	6.02	3.81
	Multi	4.43	2.90	4.18	2.94	4.70	2.80	4.12	2.72	4.38	3.35
4	T_1w	4.15	4.23	2.21	3.12	3.73	4.35	3.27	3.26	3.88	4.16
	T_2w	3.66	3.66	2.90	2.72	4.47	4.02	3.56	3.24	3.90	3.95
	Multi	4.03	2.50	2.89	2.52	3.91	2.57	2.67	2.48	3.41	3.43
5	T_1w	5.29	4.07	3.37	4.10	2.79	4.26	3.48	4.02	3.61	4.68
	T_2w	4.28	4.54	3.16	3.64	3.93	3.94	4.58	4.49	4.16	5.08
	Multi	3.26	3.08	2.73	3.19	3.40	3.33	3.72	3.30	3.88	3.72
6	T_1w	4.54	4.67	4.05	5.99	4.00	5.03	4.63	5.80	3.96	6.12
	T_2w	3.92	2.92	5.30	4.05	3.69	2.92	4.30	4.87	4.59	3.82
	Multi	4.29	2.40	5.00	2.70	3.13	2.53	4.62	2.65	5.01	2.69
7	T_1w	4.07	4.65	2.02	3.58	3.35	3.51	3.34	4.25	4.01	4.03
	T_2w	4.32	3.28	3.19	2.91	2.93	3.24	2.69	3.30	3.80	3.95
	Multi	3.87	3.17	3.31	3.32	2.71	3.17	3.28	2.81	4.52	4.25
8	T_1w	3.49	2.54	1.97	1.75	1.94	2.60	3.02	2.53	1.68	2.47
	T_2w	2.61	1.85	2.27	2.37	2.04	2.47	2.52	1.96	3.51	3.57
	Multi	2.09	1.78	2.34	1.90	2.12	1.56	2.00	1.76	3.01	2.98
9	T_1w	5.79	2.54	2.70	1.75	2.64	2.60	2.54	2.53	6.14	2.47
	T_2w	6.27	1.85	3.10	2.37	4.14	2.47	2.07	1.96	4.80	3.57
	Multi	3.32	1.78	3.00	1.90	3.99	1.56	3.58	1.76	5.06	2.98
10	T_1w	8.41	3.18	7.78	3.21	8.86	3.26	8.43	2.96	8.44	5.97
	T_2w	9.23	2.53	8.03	4.43	8.42	3.79	8.56	3.42	8.50	6.40
	Multi	7.23	2.18	7.58	2.18	8.05	2.28	7.63	2.35	7.62	2.97

APPENDIX B

DETAILED LIST OF TEXTURAL ANALYSIS STUDY

Table B1. List of textural features

	Nomenclature	**Description**
First order statistics (FOS)	MN	Mean
	STD	Standard deviation
	3rdM	Third Moment
	ENT1	Entropy
	KRT	Kurtosis
	SKW	Skewness
Gray level co-occurrence matrix (GLCM)	HMO	Homogeneity
	CNT	Contrast
	CRR	Correlation
	DIA	Diagonal
	ENT2	Entropy
	EGR	Energy
Gray level run-length matrix (GRLM)	SRE	Short run emphasis
	LRE	Long run emphasis
	RLN	Run length non-uniformity
	RP	Run percentage
	GLN	Gray level non-uniformity
	LGRE	low gray level run emphasis
	HGRE	high gray level run emphasis
Local binary patterns (LBP)	LBP1	Local binary pattern 1
	LBP2	Local binary pattern 2
	LBP3	Local binary pattern 3
	LBP4	Local binary pattern 4
	LBP5	Local binary pattern 5
	LBP6	Local binary pattern 6
	LBP7	Local binary pattern 7
	LBP8	Local binary pattern 8
	LBP9	Local binary pattern 9
	LBP10	Local binary pattern 10
Wavelet transform (WL)	CAM	Mean of approximation detail image
	CHM	Mean of horizontal detail image
	CVM	Mean of vertical detail image
	CDM	Mean of Diagonal detail image
	CAV	Variance of approximation detail image
	CHV	Variance of horizontal detail image

CVV	Variance of vertical detail image
CDV	Variance of Diagonal detail image
CAE	Energy of approximation detail image
CHE	Energy of horizontal detail image
CVE	Energy of vertical detail image
CDE	Energy of Diagonal detail image

Table B2. List of features for maximized accuracy for T_1w and T_2w images

1 textual features			2 textual features						3 textual features								
T1w	T2w	Both	T1w		T2w		Both		T1w			T2w			Both		
3rdM	3rdM	LGRE	ENT1	CDV	STD	CDV	ENT1	LGRE	MN	ENT1	CDV	3rdM	LGRE	CDV	MN	ENT1	CDV
CAM		CAM	HMO	CDV	3rdM	CNT	ENT1	CDV	MN	HMO	CDV	DIA	CHV	CVE	MN	HMO	CDV
CDV			CNT	CHM	3rdM	CDV	HMO	CDV	MN	CNT	CDV	RP	LGRE	CDE	MN	CNT	CDV
			CNT	CDV	LGRE	LBP1	CNT	CDV	MN	CRR	CDV	RP	CAM	CDE	MN	CRR	CDV
			CRR	CDV	LBP3	CVM	CRR	CDV	MN	ENT2	CDV	GLN	CHV	CVE	MN	DIA	CDV
			DIA	CDV	LBP5	CVM	DIA	CDV	MN	EGR	CDV	HGRE	CHV	CVE	MN	ENT2	CDV
			ENT2	CDV			ENT2	CDV	MN	LBP2	CDV	LBP1	CAM	CHE	MN	EGR	CDV
			EGR	CDV			EGR	CDV	MN	LBP3	CDV				MN	SRE	CDV
			GLN	CDV			RP	CVV	MN	LBP6	CDV				MN	RP	CVV
			HGRE	CDV			GLN	CDV	MN	CVM	CDV				MN	RP	CDV
			LBP2	CDV			LGRE	CHE	MN	CDV	CAE				MN	LGRE	CDV
			LBP3	CDV			HGRE	CDV	MN	CDV	CDE				MN	LBP3	CDV
			LBP4	CDV			LBP1	CDV	ENT1	KRT	CDV				MN	LBP7	CDV
			LBP6	CDV			LBP2	CDV	ENT1	SKW	CDV				MN	CDM	CDV
			LBP7	CAV			LBP3	CDV	ENT1	HMO	CDV				MN	CAV	CDV
			LBP8	CDV			LBP5	CDV	ENT1	CNT	CDV				MN	CHV	CDV
			LBP10	CDV			LBP7	CDV	ENT1	CRR	CDV				MN	CVV	CDV
			CVM	CDV			CVM	CDV	ENT1	DIA	CDV				ENT1	SKW	CDV
			CHV	CDV			CDM	CDV	ENT1	ENT2	CDV				ENT1	HMO	LGRE
			CDV	CAE			CDM	CDE	ENT1	EGR	CDV				ENT1	HMO	CDV
			CDV	CDE			CAV	CDV	ENT1	SRE	CDV				ENT1	CNT	CDV
							CHV	CDV	ENT1	LRE	CDV				ENT1	CRR	LGRE
							CVV	CDV	ENT1	RLN	CDV				ENT1	CRR	CDV
							CDV	CDE	ENT1	GLN	CDV				ENT1	DIA	CDV
									ENT1	LGRE	CDV				ENT1	ENT2	LGRE
									ENT1	LGRE	CAE				ENT1	ENT2	CDV
									ENT1	HGRE	CDV				ENT1	EGR	LGRE
									ENT1	LBP1	CDV				ENT1	EGR	CDV
									ENT1	LBP2	CDV				ENT1	RLN	CDV
									ENT1	LBP3	CDV				ENT1	RP	CDV
									ENT1	LBP4	CDV				ENT1	GLN	CDV
									ENT1	LBP5	CDV				ENT1	LGRE	CAM
									ENT1	LBP6	CDV				ENT1	LGRE	CDV
									ENT1	LBP7	CDV				ENT1	HGRE	CDV
									ENT1	LBP8	CDV				ENT1	LBP1	CDV
									ENT1	LBP9	CDV				ENT1	LBP2	CDV
									ENT1	LBP10	CDV				ENT1	LBP3	CDV
									ENT1	CAM	CDV				ENT1	LBP5	CDV
									ENT1	CHM	CDV				ENT1	LBP7	CDV
									ENT1	CVM	CDV				ENT1	LBP8	CDV
									ENT1	CDM	CDV				ENT1	CAM	CDV
									ENT1	CAV	CDV				ENT1	CHM	CAV
									ENT1	CHV	CDV				ENT1	CHM	CDV
									ENT1	CVV	CDV				ENT1	CVM	CDV
									ENT1	CDV	CAE				ENT1	CDM	CDV
									ENT1	CDV	CVE				ENT1	CAV	CDV
									ENT1	CDV	CDE				ENT1	CHV	CDV
									KRT	HMO	CDV				ENT1	CVV	CDV

Table B2. Continued

1 textural features			2 textural features			3 textural features						
T1w	T2w	Both	T1w	T2w	Both	T1w			T2w	Both		
						KRT	CNT	CDV		KRT	DIA	CDV
						KRT	CRR	CDV		KRT	LGRE	CDV
						KRT	DIA	CDV		KRT	CAM	CDV
						KRT	ENT2	CDV		KRT	CDM	CDV
						KRT	EGR	CDV		KRT	CHV	CDV
						KRT	GLN	CDV		SKW	HMO	CDV
						KRT	HGRE	CDV		SKW	CNT	CDV
						KRT	LBP3	CDV		SKW	CRR	CDV
						KRT	LBP6	CDV		SKW	DIA	CDV
						KRT	LBP8	CDV		SKW	ENT2	CDV
						KRT	CVM	CDV		SKW	EGR	CDV
						KRT	CHV	CDV		SKW	GLN	CDV
						KRT	CDV	CAE		SKW	LGRE	CDV
						KRT	CDV	CDE		SKW	HGRE	CDV
						SKW	HMO	CDV		SKW	LBP2	CDV
						SKW	CNT	CDV		SKW	CAM	CDV
						SKW	CRR	CDV		SKW	CDM	CDV
						SKW	DIA	CDV		SKW	CHV	CDV
						SKW	ENT2	CDV		SKW	CVV	CDV
						SKW	EGR	CDV		HMO	CNT	CDV
						SKW	GLN	CDV		HMO	CRR	CDV
						SKW	HGRE	CDV		HMO	DIA	CDV
						SKW	LBP2	CDV		HMO	ENT2	CDV
						SKW	LBP3	CDV		HMO	EGR	CDV
						SKW	LBP4	CDV		HMO	RLN	CDV
						SKW	LBP6	CDV		HMO	RP	CDV
						SKW	LBP8	CDV		HMO	GLN	CDV
						SKW	CVM	CDV		HMO	LGRE	CDV
						SKW	CHV	CDV		HMO	HGRE	CDV
						SKW	CDV	CAE		HMO	LBP1	CDV
						SKW	CDV	CDE		HMO	LBP2	CDV
						HMO	CNT	CDV		HMO	LBP3	CDV
						HMO	CRR	CDV		HMO	LBP4	CDV
						HMO	DIA	CDV		HMO	LBP5	CDV
						HMO	ENT2	CDV		HMO	LBP7	CDV
						HMO	EGR	CDV		HMO	LBP8	CDV
						HMO	LRE	CDV		HMO	CAM	CDV
						HMO	RLN	CDV		HMO	CHM	CDV
						HMO	GLN	CDV		HMO	CVM	CDV
						HMO	LGRE	CDV		HMO	CDM	CDV
						HMO	LGRE	CAE		HMO	CAV	CDV
						HMO	HGRE	CDV		HMO	CHV	CDV
						HMO	LBP1	CDV		HMO	CVV	CDV
						HMO	LBP2	CDV		HMO	CDV	CDE
						HMO	LBP3	CDV		CNT	CRR	CDV
						HMO	LBP4	CDV		CNT	DIA	CDV
						HMO	LBP5	CDV		CNT	ENT2	CDV
						HMO	LBP6	CDV		CNT	EGR	CDV

Table B2. Continued

1 textural features			2 textural features			3 textural features		
T1w	T2w	Both	T1w	T2w	Both	T1w	T2w	Both
						HMO LBP7 CDV		CNT RLN CDV
						HMO LBP8 CDV		CNT RP CDV
						HMO LBP9 CDV		CNT GLN CDV
						HMO LBP10 CDV		CNT LGRE CDV
						HMO CAM CDV		CNT HGRE CDV
						HMO CHM CDV		CNT LBP1 CDV
						HMO CVM CDV		CNT LBP2 CDV
						HMO CDM CDV		CNT LBP3 CDV
						HMO CAV CDV		CNT LBP4 CDV
						HMO CHV CDV		CNT LBP7 CDV
						HMO CVV CDV		CNT LBP10 CDV
						HMO CDV CAE		CNT CAM CDV
						HMO CDV CVE		CNT CHM CDV
						HMO CDV CDE		CNT CVM CDV
						CNT CRR CDV		CNT CDM CDV
						CNT DIA CDV		CNT CAV CDV
						CNT ENT2 CDV		CNT CHV CDV
						CNT EGR CDV		CNT CVV CDV
						CNT LRE CDV		CNT CDV CAE
						CNT RLN CDV		CNT CDV CHE
						CNT GLN CDV		CNT CDV CDE
						CNT LGRE CDV		CRR DIA CDV
						CNT LGRE CAE		CRR ENT2 CDV
						CNT HGRE CDV		CRR EGR CDV
						CNT LBP1 CDV		CRR RLN CDV
						CNT LBP2 CDV		CRR RP CDV
						CNT LBP3 CDV		CRR GLN CDV
						CNT LBP4 CDV		CRR LGRE CDV
						CNT LBP5 CDV		CRR HGRE CDV
						CNT LBP6 CDV		CRR LBP1 CDV
						CNT LBP7 CDV		CRR LBP2 CDV
						CNT LBP8 CDV		CRR LBP3 CDV
						CNT LBP9 CDV		CRR LBP4 CDV
						CNT LBP10 CDV		CRR LBP5 CDV
						CNT CAM CDV		CRR LBP7 CDV
						CNT CHM CDV		CRR LBP8 CDV
						CNT CVM CDV		CRR CAM CDV
						CNT CDM CDV		CRR CHM CAV
						CNT CHV CDV		CRR CHM CDV
						CNT CVV CDV		CRR CVM CDV
						CNT CDV CAE		CRR CDM CDV
						CNT CDV CHE		CRR CAV CDV
						CNT CDV CVE		CRR CHV CDV
						CNT CDV CDE		CRR CVV CDV
						CRR DIA CDV		CRR CDV CDE
						CRR ENT2 CDV		DIA ENT2 CDV
						CRR EGR CDV		DIA EGR CDV
						CRR LRE CDV		DIA RP CDV

Table B2. Continued

1 textural features			2 textural features			3 textural features						
T1w	T2w	Both	T1w	T2w	Both	T1w			T2w	Both		
						CRR	RLN	CDV		DIA	GLN	CDV
						CRR	GLN	CDV		DIA	LGRE	CDV
						CRR	LGRE	CDV		DIA	HGRE	CDV
						CRR	LGRE	CAE		DIA	LBP1	CDV
						CRR	HGRE	CDV		DIA	LBP2	CDV
						CRR	LBP1	CDV		DIA	LBP3	CDV
						CRR	LBP2	CDV		DIA	LBP5	CDV
						CRR	LBP3	CDV		DIA	LBP7	CDV
						CRR	LBP4	CDV		DIA	CAM	CDV
						CRR	LBP5	CDV		DIA	CHM	CDV
						CRR	LBP6	CDV		DIA	CVM	CDV
						CRR	LBP7	CDV		DIA	CDM	CDV
						CRR	LBP8	CDV		DIA	CAV	CDV
						CRR	LBP9	CDV		DIA	CHV	CDV
						CRR	LBP10	CDV		DIA	CVV	CDV
						CRR	CAM	CDV		DIA	CDV	CAE
						CRR	CHM	CDV		DIA	CDV	CDE
						CRR	CVM	CDV		ENT2	EGR	CDV
						CRR	CDM	CDV		ENT2	RLN	CDV
						CRR	CAV	CDV		ENT2	RP	CDV
						CRR	CHV	CDV		ENT2	GLN	CDV
						CRR	CVV	CDV		ENT2	LGRE	CDV
						CRR	CDV	CAE		ENT2	HGRE	CDV
						CRR	CDV	CVE		ENT2	LBP1	CDV
						CRR	CDV	CDE		ENT2	LBP2	CDV
						DIA	ENT2	CDV		ENT2	LBP3	CDV
						DIA	EGR	CDV		ENT2	LBP4	CDV
						DIA	LRE	CDV		ENT2	LBP5	CDV
						DIA	RLN	CDV		ENT2	LBP7	CDV
						DIA	GLN	CDV		ENT2	LBP8	CDV
						DIA	LGRE	CDV		ENT2	CAM	CDV
						DIA	LGRE	CAE		ENT2	CHM	CAV
						DIA	HGRE	CDV		ENT2	CHM	CDV
						DIA	LBP1	CDV		ENT2	CVM	CDV
						DIA	LBP2	CDV		ENT2	CDM	CDV
						DIA	LBP3	CDV		ENT2	CAV	CDV
						DIA	LBP4	CDV		ENT2	CHV	CDV
						DIA	LBP5	CDV		ENT2	CVV	CDV
						DIA	LBP6	CDV		ENT2	CDV	CDE
						DIA	LBP7	CDV		EGR	RLN	CDV
						DIA	LBP8	CDV		EGR	RP	CDV
						DIA	LBP9	CDV		EGR	GLN	CDV
						DIA	LBP10	CDV		EGR	LGRE	CDV
						DIA	CAM	CDV		EGR	HGRE	CDV
						DIA	CHM	CDV		EGR	LBP1	CDV
						DIA	CVM	CDV		EGR	LBP2	CDV
						DIA	CDM	CDV		EGR	LBP3	CDV
						DIA	CAV	CDV		EGR	LBP4	CDV

Table B2. Continued

1 textural features			2 textural features			3 textural features		
T1w	T2w	Both	T1w	T2w	Both	T1w	T2w	Both
						DIA CHV CDV		EGR LBP5 CDV
						DIA CVV CDV		EGR LBP7 CDV
						DIA CDV CAE		EGR LBP8 CDV
						DIA CDV CVE		EGR CAM CDV
						DIA CDV CDE		EGR CHM CDV
						ENT2 EGR CDV		EGR CVM CDV
						ENT2 LRE CDV		EGR CDM CDV
						ENT2 RLN CDV		EGR CAV CDV
						ENT2 GLN CDV		EGR CHV CDV
						ENT2 LGRE CDV		EGR CVV CDV
						ENT2 LGRE CAE		EGR CDV CDE
						ENT2 HGRE CDV		LRE CAM CDV
						ENT2 LBP1 CDV		LRE CAV CDV
						ENT2 LBP2 CDV		LRE CHV CDV
						ENT2 LBP3 CDV		RLN RP CVV
						ENT2 LBP4 CDV		RLN GLN CDV
						ENT2 LBP5 CDV		RLN LGRE CDV
						ENT2 LBP6 CDV		RLN HGRE CDV
						ENT2 LBP7 CDV		RLN LBP2 CDV
						ENT2 LBP8 CDV		RLN CAV CDV
						ENT2 LBP9 CDV		RLN CHV CDV
						ENT2 LBP10 CDV		RP GLN CDV
						ENT2 CAM CDV		RP HGRE CDV
						ENT2 CHM CDV		RP LBP2 CDV
						ENT2 CVM CDV		RP LBP7 CVV
						ENT2 CDM CDV		RP CVV CDV
						ENT2 CAV CDV		GLN LGRE CDV
						ENT2 CHV CDV		GLN HGRE CDV
						ENT2 CVV CDV		GLN LBP1 CDV
						ENT2 CDV CAE		GLN LBP2 CDV
						ENT2 CDV CVE		GLN LBP3 CDV
						ENT2 CDV CDE		GLN LBP7 CDV
						EGR LRE CDV		GLN CAM CDV
						EGR RLN CDV		GLN CHM CDV
						EGR GLN CDV		GLN CVM CDV
						EGR LGRE CDV		GLN CDM CDV
						EGR LGRE CAE		GLN CAV CDV
						EGR HGRE CDV		GLN CHV CDV
						EGR LBP1 CDV		GLN CVV CDV
						EGR LBP2 CDV		GLN CDV CDE
						EGR LBP3 CDV		LGRE HGRE CDV
						EGR LBP4 CDV		LGRE LBP1 CDV
						EGR LBP5 CDV		LGRE LBP2 CDV
						EGR LBP6 CDV		LGRE LBP3 CDV
						EGR LBP7 CDV		LGRE LBP5 CDV
						EGR LBP8 CDV		LGRE LBP7 CDV
						EGR LBP9 CDV		LGRE CAM CVV
						EGR LBP10 CDV		LGRE CAM CAE

Table B2. Continued

1 textural features			2 textural features			3 textural features						
T1w	T2w	Both	T1w	T2w	Both	T1w			T2w	Both		
						EGR	CAM	CDV		LGRE	CAM	CHE
						EGR	CHM	CDV		LGRE	CAM	CDE
						EGR	CVM	CDV		LGRE	CHM	CVV
						EGR	CDM	CDV		LGRE	CHM	CDE
						EGR	CAV	CDV		LGRE	CVM	CDV
						EGR	CHV	CDV		LGRE	CDM	CDV
						EGR	CVV	CDV		LGRE	CDM	CDE
						EGR	CDV	CAE		LGRE	CAV	CDV
						EGR	CDV	CVE		LGRE	CAV	CHE
						EGR	CDV	CDE		LGRE	CHV	CDV
						SRE	LBP3	CDV		LGRE	CVV	CDV
						SRE	CDV	CAE		LGRE	CDV	CAE
						LRE	GLN	CDV		LGRE	CDV	CDE
						LRE	HGRE	CDV		HGRE	LBP1	CDV
						LRE	LBP2	CDV		HGRE	LBP2	CDV
						LRE	LBP3	CDV		HGRE	LBP3	CDV
						LRE	LBP4	CDV		HGRE	LBP7	CDV
						LRE	LBP6	CDV		HGRE	CAM	CDV
						LRE	LBP8	CDV		HGRE	CHM	CDV
						LRE	LBP10	CDV		HGRE	CVM	CDV
						LRE	CVM	CDV		HGRE	CDM	CDV
						LRE	CHV	CDV		HGRE	CAV	CDV
						LRE	CDV	CAE		HGRE	CHV	CDV
						LRE	CDV	CDE		HGRE	CVV	CDV
						RLN	GLN	CDV		HGRE	CDV	CDE
						RLN	HGRE	CDV		LBP1	LBP2	CDV
						RLN	LBP2	CDV		LBP1	LBP3	CDV
						RLN	LBP3	CDV		LBP1	CHM	CDV
						RLN	LBP4	CDV		LBP1	CDM	CVE
						RLN	LBP6	CDV		LBP1	CAV	CDV
						RLN	LBP7	CAV		LBP1	CVV	CDV
						RLN	LBP8	CDV		LBP1	CDV	CDE
						RLN	LBP10	CDV		LBP2	LBP3	CDV
						RLN	CVM	CDV		LBP2	CAM	CDV
						RLN	CHV	CDV		LBP2	CAV	CDV
						RLN	CDV	CAE		LBP2	CHV	CDV
						RLN	CDV	CDE		LBP2	CVV	CDV
						RP	LBP2	CDV		LBP2	CDV	CDE
						RP	LBP3	CDV		LBP3	CAM	CDV
						RP	CDV	CAE		LBP3	CHM	CDV
						GLN	LGRE	CDV		LBP3	CAV	CDV
						GLN	LGRE	CAE		LBP3	CHV	CDV
						GLN	HGRE	CDV		LBP3	CVV	CDV
						GLN	LBP1	CDV		LBP3	CDV	CAE
						GLN	LBP2	CDV		LBP3	CDV	CHE
						GLN	LBP3	CDV		LBP3	CDV	CVE
						GLN	LBP4	CDV		LBP3	CDV	CDE
						GLN	LBP5	CDV		LBP4	CAV	CDV

Table B2. Continued

1 textural features			2 textural features			3 textural features		
T1w	T2w	Both	T1w	T2w	Both	T1w	T2w	Both
						GLN LBP6 CDV		LBP4 CHV CDV
						GLN LBP7 CDV		LBP5 CAM CDV
						GLN LBP8 CDV		LBP5 CHM CDV
						GLN LBP9 CDV		LBP5 CAV CDV
						GLN LBP10 CDV		LBP5 CHV CDV
						GLN CAM CDV		LBP5 CVV CDV
						GLN CHM CDV		LBP5 CDV CVE
						GLN CVM CDV		LBP5 CDV CDE
						GLN CDM CDV		LBP6 CAV CDV
						GLN CAV CDV		LBP6 CHV CDV
						GLN CHV CDV		LBP7 CAM CDV
						GLN CVV CDV		LBP7 CHM CDV
						GLN CDV CAE		LBP7 CAV CDV
						GLN CDV CVE		LBP7 CHV CDV
						GLN CDV CDE		LBP7 CVV CDV
						LGRE HGRE CDV		LBP7 CDV CDE
						LGRE HGRE CAE		LBP8 CDM CDE
						LGRE LBP2 CDV		LBP8 CAV CDV
						LGRE LBP3 CDV		LBP8 CHV CDV
						LGRE LBP4 CDV		LBP9 CHV CDV
						LGRE LBP4 CAE		LBP10 CAV CDV
						LGRE LBP6 CDV		LBP10 CHV CDV
						LGRE LBP7 CAE		CAM CVM CDV
						LGRE LBP8 CDV		CAM CDM CDV
						LGRE LBP9 CAV		CAM CAV CDV
						LGRE LBP10 CDV		CAM CAV CHE
						LGRE LBP10 CAE		CAM CHV CDV
						LGRE CHM CAE		CAM CVV CDV
						LGRE CVM CDV		CAM CDV CAE
						LGRE CHV CDV		CHM CVM CDV
						LGRE CDV CAE		CHM CAV CDV
						LGRE CDV CDE		CHM CAV CVE
						HGRE LBP1 CDV		CHM CAV CDE
						HGRE LBP2 CDV		CHM CHV CDV
						HGRE LBP3 CDV		CHM CHV CDE
						HGRE LBP4 CDV		CHM CVV CDV
						HGRE LBP5 CDV		CHM CDV CDE
						HGRE LBP6 CDV		CVM CAV CDV
						HGRE LBP7 CDV		CVM CHV CDV
						HGRE LBP8 CDV		CVM CDV CDE
						HGRE LBP9 CDV		CDM CAV CDV
						HGRE LBP10 CDV		CDM CAV CDE
						HGRE CAM CDV		CDM CHV CDV
						HGRE CHM CDV		CDM CVV CDV
						HGRE CVM CDV		CDM CDV CAE
						HGRE CDM CDV		CDM CDV CHE
						HGRE CAV CDV		CDM CDV CVE
						HGRE CHV CDV		CDM CDV CDE

Table B2. Continued

1 textural features			2 textural features			3 textural features		
T1w	T2w	Both	T1w	T2w	Both	T1w	T2w	Both
						HGRE CVV CDV		CAV CHV CDV
						HGRE CDV CAE		CAV CVV CDV
						HGRE CDV CVE		CAV CVV CDE
						HGRE CDV CDE		CAV CDV CHE
						LBP1 LBP2 CDV		CAV CDV CVE
						LBP1 LBP3 CDV		CAV CDV CDE
						LBP1 LBP4 CDV		CHV CVV CDV
						LBP1 LBP6 CDV		CHV CDV CAE
						LBP1 LBP8 CDV		CHV CDV CHE
						LBP1 LBP10 CDV		CHV CDV CVE
						LBP1 CVM CDV		CHV CDV CDE
						LBP1 CHV CDV		CVV CDV CAE
						LBP1 CDV CAE		
						LBP1 CDV CDE		
						LBP2 LBP3 CDV		
						LBP2 LBP4 CDV		
						LBP2 LBP5 CDV		
						LBP2 LBP6 CDV		
						LBP2 LBP7 CDV		
						LBP2 LBP8 CDV		
						LBP2 LBP9 CDV		
						LBP2 LBP10 CDV		
						LBP2 CAM CDV		
						LBP2 CVM CDV		
						LBP2 CAV CDV		
						LBP2 CHV CDV		
						LBP2 CVV CDV		
						LBP2 CDV CAE		
						LBP2 CDV CVE		
						LBP2 CDV CDE		
						LBP3 LBP4 CDV		
						LBP3 LBP5 CDV		
						LBP3 LBP6 CDV		
						LBP3 LBP7 CDV		
						LBP3 LBP9 CDV		
						LBP3 LBP10 CDV		
						LBP3 CVM CDV		
						LBP3 CDM CHE		
						LBP3 CAV CDV		
						LBP3 CHV CDV		
						LBP3 CVV CDV		
						LBP3 CDV CAE		
						LBP3 CDV CVE		
						LBP3 CDV CDE		
						LBP4 LBP5 CDV		
						LBP4 LBP6 CDV		

Table B2. Continued

1 textural features			2 textural features			3 textural features		
T1w	T2w	Both	T1w	T2w	Both	T1w	T2w	Both
						LBP4 LBP7 CDV		
						LBP4 LBP8 CDV		
						LBP4 LBP9 CDV		
						LBP4 LBP10 CDV		
						LBP4 CAM CDV		
						LBP4 CVM CDV		
						LBP4 CAV CDV		
						LBP4 CHV CDV		
						LBP4 CVV CDV		
						LBP4 CDV CAE		
						LBP4 CDV CDE		
						LBP5 LBP6 CDV		
						LBP5 LBP8 CDV		
						LBP5 LBP10 CDV		
						LBP5 CVM CDV		
						LBP5 CHV CDV		
						LBP5 CDV CAE		
						LBP5 CDV CDE		
						LBP6 LBP7 CDV		
						LBP6 LBP8 CDV		
						LBP6 LBP10 CDV		
						LBP6 CVM CDV		
						LBP6 CHV CDV		
						LBP6 CVV CDV		
						LBP6 CDV CAE		
						LBP6 CDV CVE		
						LBP6 CDV CDE		
						LBP7 LBP8 CDV		
						LBP7 LBP10 CDV		
						LBP7 CVM CDV		
						LBP7 CHV CDV		
						LBP7 CDV CAE		
						LBP7 CDV CDE		
						LBP8 LBP9 CDV		
						LBP8 LBP10 CDV		
						LBP8 CAM CDV		
						LBP8 CVM CDV		
						LBP8 CAV CDV		
						LBP8 CHV CDV		
						LBP8 CVV CDV		
						LBP8 CDV CAE		
						LBP8 CDV CDE		
						LBP9 LBP10 CDV		
						LBP9 CAM CDV		
						LBP9 CVM CDV		
						LBP9 CAV CDV		
						LBP9 CHV CDV		
						LBP9 CDV CAE		

Table B2. Continued

1 textural features			2 textural features			3 textural features		
T1w	T2w	Both	T1w	T2w	Both	T1w	T2w	Both
						LBP10 CAM CDV		
						LBP10 CVM CDV		
						LBP10 CAV CDV		
						LBP10 CHV CDV		
						LBP10 CVV CDV		
						LBP10 CDV CAE		
						LBP10 CDV CDE		
						CAM CHM CAE		
						CAM CVM CDV		
						CAM CHV CDV		
						CAM CDV CAE		
						CAM CDV CDE		
						CHM CVM CDV		
						CHM CHV CDV		
						CHM CDV CAE		
						CHM CDV CDE		
						CVM CDM CDV		
						CVM CAV CDV		
						CVM CHV CDV		
						CVM CVV CDV		
						CVM CDV CAE		
						CVM CDV CHE		
						CVM CDV CVE		
						CVM CDV CDE		
						CDM CHV CDV		
						CDM CDV CAE		
						CDM CDV CDE		
						CAV CHV CDV		
						CAV CDV CAE		
						CAV CDV CDE		
						CHV CVV CDV		
						CHV CDV CAE		
						CHV CDV CHE		
						CHV CDV CVE		
						CHV CDV CDE		
						CVV CDV CAE		
						CVV CDV CDE		
						CDV CAE CVE		
						CDV CAE CDE		
						CDV CVE CDE		

Table B3. List of features for maximized accuracy for T_1m and T_2m images

1 textural features			2 textural features						3 textural features								
T1m	T2m	Both	T1m		T2m		Both		T1m			T2m			Both		
STD	MN	CDE	STD	LGRE	LBP2	LBP10	SRE	CDE	STD	LGRE	CAM	HMO	RLN	LBP10	STD	LBP1	CDE
3rdM	SKW		LGRE	CHM	LBP4	LBP6	RLN	CDE	3rdM	LGRE	CAM	CNT	RLN	LBP2	3rdM	LBP1	CDE
ENT1	LGRE		LBP9	CDE			LBP7	CDE	RLN	LBP5	CVM	CNT	RLN	LBP10	3rdM	LBP2	CDE
HMO	CHM						CVM	CDE	LGRE	CVM	CDE	CRR	RLN	LBP10	3rdM	LBP6	CDE
ENT2	CVE						CHV	CDE				DIA	RLN	LBP10	3rdM	LBP9	CDE
EGR												DIA	LBP2	LBP10	3rdM	LBP10	CDE
RLN												ENT2	RLN	LBP10	KRT	LBP1	LBP6
LBP1												EGR	RLN	LBP10	KRT	LBP1	LBP8
LBP4												RLN	LBP5	LBP10	KRT	LBP1	CDE
LBP6												RLN	LBP10	CAE	SKW	LBP1	CDE
LBP8												GLN	LBP8	CDE	HMO	SRE	CDE
LBP9												HGRE	LBP8	CDE	ENT2	SRE	CDE
LBP10												LBP1	LBP6	CVM	EGR	SRE	CDE
CAM												LBP1	LBP6	CDE	SRE	LBP2	CDE
CHM												LBP1	LBP9	CVM	SRE	LBP3	CDE
CDM												LBP1	LBP9	CAE	SRE	LBP4	CDE
CHV												LBP2	LBP5	LBP10	SRE	LBP6	CDE
CDV												LBP4	LBP7	CDE	SRE	LBP10	CDE
CAE												LBP6	LBP9	CDE	SRE	CDM	CDE
CHE												LBP6	CAE	CDE	SRE	CAV	CDE
												LBP8	LBP9	CVM	SRE	CHV	CDE
															SRE	CDV	CDE
															SRE	CAE	CDE
															RLN	LBP7	CDE
															RLN	LBP9	CDE
															LBP1	CVM	CHV
															LBP2	LBP7	CDE
															LBP2	CHV	CDE
															LBP4	CVM	CDE
															LBP4	CHV	CDE
															LBP5	LBP6	CDE
															LBP5	LBP8	CDE
															LBP5	LBP9	CDE
															LBP5	LBP10	CDE
															LBP6	LBP7	CDE
															LBP6	CHV	CDE
															LBP7	LBP8	CDE
															LBP9	CHV	CDE
															LBP10	CHV	CDE
															CVM	CAV	CDE
															CVM	CHV	CDE
															CAV	CHV	CDE
															CHV	CAE	CDE

Table B4. List of features for maximized accuracy for DWf and DFf images

1 textual features			2 textual features						3 textual features								
DWf	DFf	Both	DWf		DFf		Both		DWf			DFf			Both		
CHM	3rdM	SRE	MN	CHM	3rdM	SRE	3rdM	LBP5	MN	ENT1	CAM	MN	SRE	CHE	3rdM	ENT1	CDE
	ENT1		HMO	CHM	HMO	CVE	3rdM	LBP7	MN	ENT1	CHM	MN	CVV	CHE	3rdM	SRE	LBP5
	HMO		EGR	CHM	CNT	CDE	HMO	SRE	MN	ENT1	CVE	MN	CVV	CVE	3rdM	SRE	LBP7
	CNT		CAM	CHM	ENT2	CVE	CRR	SRE	MN	HMO	CVE	STD	SRE	CHE	3rdM	SRE	CVE
	CRR		CHM	CHE	EGR	CVE	ENT2	SRE	MN	CRR	CVE	STD	SRE	CVE	3rdM	RLN	LBP5
	DIA				SRE	LRE	EGR	SRE	MN	ENT2	CVE	3rdM	SRE	CHE	3rdM	RLN	CVE
	ENT2				SRE	CVE	SRE	RLN	MN	EGR	CVE	3rdM	SRE	CVE	3rdM	RLN	CDE
	EGR				RLN	LBP10	SRE	GLN	3rdM	LBP4	CVV	3rdM	CVV	CVE	3rdM	RP	CVE
	SRE				LBP4	LBP10	SRE	LGRE	ENT1	GLN	CHM	ENT1	HMO	CVE	3rdM	GLN	CDE
	LRE				CVV	CVE	SRE	HGRE	ENT1	GLN	CAE	ENT1	CNT	CDE	3rdM	HGRE	CDE
	RLN				CVE	CDE	SRE	LBP3	ENT1	LGRE	CHM	ENT1	ENT2	CVE	3rdM	LBP5	LBP7
	GLN						SRE	LBP4	ENT1	HGRE	CHM	ENT1	EGR	CVE	3rdM	LBP5	CHM
	HGRE						SRE	LBP9	ENT1	HGRE	CAE	ENT1	SRE	RP	3rdM	LBP5	CDM
	LBP1						SRE	CAM	ENT1	CAM	CHM	ENT1	SRE	CVE	3rdM	LBP5	CVV
	LBP5						SRE	CAV	ENT1	CHM	CHE	ENT1	LBP4	CVE	3rdM	LBP5	CDV
	LBP9						SRE	CHV	ENT1	CHM	CVE	ENT1	CVV	CVE	3rdM	LBP5	CHE
	CHM						SRE	CVV	HMO	GLN	CHM	ENT1	CVE	CDE	3rdM	LBP5	CVE
	CDM						SRE	CHE	HMO	LGRE	CHM	KRT	CHV	CVE	3rdM	LBP5	CDE
	CAV						SRE	CVE	HMO	HGRE	CHM	KRT	CVV	CVE	3rdM	LBP7	CAM
	CHV						LBP5	CHM	HMO	CAM	CHM	SKW	CHV	CVE	3rdM	LBP7	CHM
	CDV						LBP7	CHM	HMO	CHM	CHE	SKW	CVV	CVE	3rdM	LBP7	CDM
	CVE						LBP10	CHM	HMO	CHM	CVE	HMO	CRR	CVE	3rdM	LBP7	CAV
							CHM	CVE	HMO	CHM	CDE	HMO	ENT2	CVE	3rdM	LBP7	CDV
									CRR	CAM	CHM	HMO	EGR	CVE	3rdM	LBP7	CHE
									CRR	CHM	CVE	HMO	SRE	RP	3rdM	LBP7	CVE
									CRR	CHM	CDE	HMO	SRE	LBP10	3rdM	LBP7	CDE
									DIA	CAM	CHM	HMO	SRE	CVE	3rdM	LBP10	CDE
									DIA	CHM	CVE	HMO	RP	CVE	3rdM	CVV	CVE
									ENT2	CAM	CHM	HMO	GLN	CVE	3rdM	CVE	CDE
									ENT2	CHM	CVE	HMO	HGRE	CVE	ENT1	GLN	CAV
									ENT2	CHM	CDE	HMO	CVV	CVE	ENT1	HGRE	CAV
									EGR	GLN	CHM	HMO	CVE	CDE	ENT1	LBP7	CHM
									EGR	LGRE	CHM	CNT	LBP4	CDE	ENT1	CHM	CDE
									EGR	HGRE	CHM	CNT	CHM	CDE	HMO	CRR	SRE
									EGR	CAM	CHM	CNT	CDM	CDE	HMO	ENT2	SRE
									EGR	CHM	CHE	CRR	EGR	CVE	HMO	EGR	SRE
									EGR	CHM	CVE	CRR	SRE	RP	HMO	SRE	RLN
									EGR	CHM	CDE	CRR	SRE	CVE	HMO	SRE	CHV
									SRE	CHM	CHE	CRR	RP	CVE	HMO	GLN	CAV
									GLN	CAM	CHM	CRR	CVV	CVE	HMO	HGRE	CAV
									HGRE	CAM	CHM	CRR	CVE	CDE	HMO	LBP7	CHM
									LBP5	CHM	CVE	DIA	CHM	CDE	CNT	SRE	CHE
												DIA	CDM	CDE	CNT	LBP5	CHM
												ENT2	EGR	CVE	CNT	CHM	CDM
												ENT2	SRE	RP	CRR	ENT2	SRE
												ENT2	SRE	CVE	CRR	EGR	SRE
												ENT2	GLN	CVE	CRR	SRE	RLN

Table B4. Continued

1 textural features			2 textural features			3 textural features						
DWf	DFf	Both	DWf	DFf	Both	DWf	DFf			Both		
							ENT2	HGRE	CVE	CRR	SRE	CHV
							ENT2	CVV	CVE	CRR	SRE	CVV
							ENT2	CVE	CDE	CRR	SRE	CVE
							EGR	SRE	RP	CRR	GLN	CAV
							EGR	SRE	LBP10	CRR	HGRE	CAV
							EGR	SRE	CVE	DIA	RLN	CHE
							EGR	RP	CVE	DIA	LBP5	CHM
							EGR	GLN	CVE	DIA	LBP5	CHE
							EGR	HGRE	CVE	DIA	LBP7	CHM
							EGR	CVV	CVE	DIA	LBP7	CHE
							EGR	CVE	CDE	DIA	CHE	CVE
							SRE	LRE	LBP6	DIA	CVE	CDE
							SRE	LRE	CAM	ENT2	EGR	SRE
							SRE	LRE	CDM	ENT2	SRE	RLN
							SRE	LRE	CAV	ENT2	SRE	CHV
							SRE	LRE	CVV	ENT2	GLN	CAV
							SRE	LRE	CHE	ENT2	HGRE	CAV
							SRE	LRE	CVE	ENT2	LBP7	CHM
							SRE	RLN	RP	EGR	SRE	RLN
							SRE	RLN	CVE	EGR	SRE	CHV
							SRE	RP	GLN	EGR	GLN	CAV
							SRE	RP	HGRE	EGR	HGRE	CAV
							SRE	RP	LBP4	EGR	LBP7	CHM
							SRE	RP	LBP5	SRE	LRE	CVE
							SRE	RP	LBP6	SRE	RLN	CHV
							SRE	RP	LBP7	SRE	RLN	CVE
							SRE	RP	LBP8	SRE	RP	CVE
							SRE	RP	LBP9	SRE	GLN	HGRE
							SRE	RP	LBP10	SRE	GLN	LBP3
							SRE	RP	CVM	SRE	GLN	LBP7
							SRE	RP	CHV	SRE	GLN	LBP9
							SRE	RP	CVV	SRE	GLN	CHM
							SRE	RP	CVE	SRE	GLN	CVM
							SRE	GLN	CVV	SRE	GLN	CAV
							SRE	GLN	CVE	SRE	GLN	CVV
							SRE	HGRE	CVV	SRE	GLN	CAE
							SRE	HGRE	CVE	SRE	GLN	CVE
							SRE	LBP2	CVV	SRE	GLN	CDE
							SRE	LBP2	CVE	SRE	LGRE	CAV
							SRE	LBP4	CVE	SRE	HGRE	LBP3
							SRE	LBP6	CVV	SRE	HGRE	LBP7
							SRE	LBP6	CVE	SRE	HGRE	LBP9
							SRE	LBP8	CVE	SRE	HGRE	CHM
							SRE	LBP9	CVE	SRE	HGRE	CVM
							SRE	LBP10	CVM	SRE	HGRE	CAV
							SRE	LBP10	CVV	SRE	HGRE	CVV
							SRE	LBP10	CVE	SRE	HGRE	CAE

Table B4. Continued

1 textural features			2 textural features			3 textural features						
DWf	DFf	Both	DWf	DFf	Both	DWf	DFf			Both		
							SRE	CHM	CVE	SRE	HGRE	CVE
							SRE	CVM	CVV	SRE	HGRE	CDE
							SRE	CVM	CVE	SRE	LBP5	CHM
							SRE	CHV	CVV	SRE	LBP5	CHV
							SRE	CHV	CVE	SRE	LBP5	CHE
							SRE	CVV	CVE	SRE	LBP5	CDE
							SRE	CVV	CDE	SRE	LBP6	CVE
							SRE	CAE	CHE	SRE	LBP7	CHM
							SRE	CAE	CVE	SRE	LBP7	CHV
							SRE	CVE	CDE	SRE	LBP7	CDE
							LRE	CVV	CVE	SRE	LBP9	CVE
							RLN	LBP3	CDE	SRE	LBP10	CVV
							RLN	LBP4	LBP10	SRE	LBP10	CVE
							RLN	LBP6	LBP10	SRE	CAM	CAV
							RLN	LBP9	LBP10	SRE	CHM	CVE
							RLN	CVV	CVE	SRE	CDM	CAV
							RP	LBP10	CVM	SRE	CDM	CVE
							RP	LBP10	CVE	SRE	CHV	CVV
							RP	CVV	CVE	SRE	CHV	CVE
							GLN	CVV	CVE	SRE	CVV	CVE
							GLN	CVE	CDE	SRE	CVV	CDE
							HGRE	CVV	CVE	LRE	LBP5	CHM
							HGRE	CVE	CDE	RLN	GLN	CHM
							LBP2	CHM	CDE	RLN	HGRE	CHM
							LBP2	CVV	CVE	RLN	LBP7	CHM
							LBP3	LBP5	CDE	RP	LBP5	CHM
							LBP3	LBP6	CDE	RP	CHM	CDM
							LBP3	LBP7	CDE	RP	CHM	CVE
							LBP3	LBP9	CDE	GLN	HGRE	CAV
							LBP3	CVM	CDE	GLN	LBP4	CHM
							LBP4	LBP5	LBP10	GLN	LBP5	CHM
							LBP4	LBP10	CAV	GLN	LBP5	CVM
							LBP4	LBP10	CHV	GLN	LBP5	CAV
							LBP4	LBP10	CAE	GLN	LBP5	CHV
							LBP4	CVV	CVE	GLN	LBP6	CHM
							LBP5	LBP6	LBP10	GLN	LBP7	CHM
							LBP5	CHM	CVE	GLN	LBP7	CVM
							LBP5	CAV	CDE	GLN	LBP7	CAV
							LBP6	CVV	CVE	GLN	LBP9	CHV
							LBP7	LBP8	CDE	GLN	LBP10	CHM
							LBP7	LBP10	CDE	GLN	CHM	CDM
							LBP7	CHM	CVE	GLN	CHM	CHV
							LBP7	CAV	CDE	GLN	CHM	CVV
							LBP7	CHV	CDE	GLN	CHM	CVE
							LBP8	CVV	CVE	GLN	CHM	CDE
							LBP9	CVV	CVE	GLN	CVM	CAV
							LBP10	CVV	CVE	GLN	CVM	CVE

Table B4. Continued

1 textural features			2 textural features			3 textural features		
DWf	DFf	Both	DWf	DFf	Both	DWf	DFf	Both
							LBP10 CVE CDE	GLN CAV CHV
							CAM CVV CVE	GLN CAV CVE
							CHM CVV CVE	HGRE LBP4 CHM
							CVM CVV CVE	HGRE LBP5 CHM
							CDM CVV CVE	HGRE LBP5 CVM
							CHV CVV CVE	HGRE LBP5 CAV
							CVV CVE CDE	HGRE LBP5 CHV
								HGRE LBP6 CHM
								HGRE LBP7 CHM
								HGRE LBP7 CVM
								HGRE LBP7 CAV
								HGRE LBP9 CHV
								HGRE LBP10 CHM
								HGRE CHM CDM
								HGRE CHM CHV
								HGRE CHM CVV
								HGRE CHM CVE
								HGRE CHM CDE
								HGRE CVM CAV
								HGRE CVM CVE
								HGRE CAV CHV
								HGRE CAV CVE
								LBP1 LBP4 CHM
								LBP1 LBP5 CHM
								LBP1 LBP7 CHM
								LBP1 CHM CDM
								LBP1 CHM CAV
								LBP1 CHM CVE
								LBP1 CHM CDE
								LBP2 LBP5 CHM
								LBP2 LBP7 CHM
								LBP2 CHM CVE
								LBP2 CHM CDE
								LBP3 CHM CVE
								LBP4 LBP7 CHM
								LBP4 CHM CVE
								LBP4 CHM CDE
								LBP5 LBP7 CHM
								LBP5 LBP10 CHM
								LBP5 CHM CDM
								LBP5 CHM CVV
								LBP5 CHM CDV
								LBP5 CHM CHE
								LBP5 CHM CVE
								LBP5 CHM CDE
								LBP7 CAM CHM
								LBP7 CHM CDM

Table B4. Continued

1 textural features			2 textural features			3 textural features		
DWf	DFf	Both	DWf	DFf	Both	DWf	DFf	Both
								LBP7 CHM CAV
								LBP7 CHM CHV
								LBP7 CHM CVV
								LBP7 CHM CDV
								LBP7 CHM CHE
								LBP7 CHM CVE
								LBP7 CHM CDE
								LBP7 CHV CDE
								CHM CDM CVE
								CHM CAV CVE
								CHM CHV CVE
								CHM CVV CVE
								CHM CDV CVE
								CHM CVE CDE
								CDM CVV CVE